Observation of Single Atom Defects and Sub-molecular Resolution with Atomic Force Microscopy in Ambient Environments

Edward Juan Dunn, MPhys (Hons)

Physics Department, Faculty of Science and Technology,

Lancaster University

A thesis submitted for the degree of

Doctor of Philosophy

December, 2023

Observation of Single Atom Defects and Sub-molecular Resolution with Atomic Force Microscopy in Ambient Environments

Edward Juan Dunn, MPhys (Hons).

Physics Department, Faculty of Science and Technology, Lancaster University

A thesis submitted for the degree of *Doctor of Philosophy*. December, 2023.

Abstract

Improvements in microscopy enable the imaging of new phenomena, driving scientific advancement and the technological change it brings. Imaging in ambient conditions in particular can create challenges which limit the resolution. If phenomena can be imaged in an ambient environment the images can be collected more quickly, allowing for faster iteration, and enabling the user to work with samples which cannot enter ultra-high vacuum equipment.

In this thesis, I demonstrate the imaging of transition metal dichalcogenides with atomic resolution conductive atomic force microscopy in ambient conditions and a comparative study alongside optical spectroscopy. Such resolution enables the differentiation of defect categories and the imaging of new types of defects created in samples via exposure to nitrogen plasma. The introduction of defects also induces changes in optical spectroscopy which can be identified in cryogenic measurements. This work builds a strong foundation for future work to establish correlations between the population of defects and features of photoluminescence spectra.

Further work on simulations explores atomic force microscopy techniques for imaging non-planar molecules, demonstrating that constant force approaches could yield high-resolution images of molecules and allow the user to extract quantitative information such as the angle of molecular moieties. Comparisons between experimental and simulated off-resonance atomic force microscope images of a network of Zn tetra-phenyl porphyrin on a Au (111) substrate show promising progress. Such images are created using atomic coordinates from density functional theory simulations and could enable the determination of the adsorption geometry of the molecules in the network in ambient conditions.

Acknowledgements

A thesis contains the work of one person, but the outcome is heavily influenced by the environment the work was carried out in. However, I would not be in a position to start this course without my parents diligent and passionate support throughout my GCSEs and A Levels. They encouraged me to aim high and then supported my decision to continue in an academic environment rather than a more certain career.

My first taste of the research environment was as a master's student under the supervision of Viktor Tsepelin. He introduced me to the use of harmonic oscillators as sensors, a subject which drove my interest in atomic force microscopy, and Python which continues to be my preferred method of data analysis. In this group, I learnt to work in the lab with the assistance of Theo Noble and Ash Jennings who gave their time enthusiastically to support me.

This PhD was funded by the "CDT in Science and Applications of Graphene and Related Nanomaterials". I received a broad introduction into 2D materials and characterisation techniques which gave me a head start before my PhD had even begun. The network of students involved in that CDT has led to many steadfast friends and kept me up to date with the exciting work at the forefront of 2D materials.

I first learnt to use the atomic force microscope in Oleg Kolosov's group with Eli Castañon and Marta San Juan Mucientes. They were incredibly friendly and showed me how an AFM can be modified in order to measure different properties.

My supervisor, Sam Jarvis, and co-supervisor, Rob Young, have been critical to my success. I have been granted a large amount of their time to discuss my progress and ask for guidance. The time and passion that they have made available to me has been key to developing a deep understanding and ensuring that I am using my time efficiently. Their advice has not simply been limited to the realm of science and their support for my career beyond this PhD and introduction to the wider scientific community has been invaluable.

I have shared laboratories with many capable scientists who have trained me on

equipment, offered their advice and made me feel welcome. In particular, I would like to thank Sophie Au-yong for helping me set up our cAFM equipment, Leo Forcieri for being a great friend and making us be social, Fangling Wu for showing me how to fabricate 2D materials, James Fong for passing on the correct operation of the cryostat and Amy Crisp for her assistance with the plasma reactor. As our PhDs finished at the same time and started 6 months apart Alessio Quadrelli has helped me throughout my PhD and I don't know where I'd be without your assistance, opinions and camaraderie.

When I am outside the lab I have worked in A15 alongside its occupants, who have created a thriving community that makes Lancaster feel like home; one that I will dearly miss as I move on. In particular, I have known Max Taylor since I was an undergraduate and playing tabletop games with him weekly has kept me going as we worked towards our PhDs.

During my viva I had many insightful conversations with my examiners Jonathan Prance and Sebastian Wood. I am thankful that my viva consisted of such productive conversations that engaged with my work and sought to improve it. Their corrections, alongside those of my supervisors, have been critical in refining this thesis into its current form.

The prestigious final place of an acknowledgements section must go to Emily Gamblen, my partner of $\sim 7\ 1/2$ years. She has been advising me, talking through my many concerns about my work and taking on some of my responsibilities when I have had to focus in my work. She has done all of this whilst pursuing her own PhD. It is hard to imagine completing this degree without her.

Declaration

I declare that the work presented in this thesis is, to the best of my knowledge and belief, original and my own work. The material has not been submitted, either in whole or in part, for a degree at this, or any other university. This thesis does not exceed the maximum permitted word length of 80,000 words including appendices and footnotes, but excluding the bibliography.

Edward Juan Dunn

Publications

Edward Juan Dunn, Robert Young and Samuel Paul Jarvis. "Contrasting the point defects of TMDs with Atomic Resolution Conductive Atomic Force Microscopy". *Manuscript in preparation*

Edward Juan Dunn, Shabnam Naseri, Leonardo Forcieri, Andreas Larson and Samuel Paul Jarvis. "Interpretation of ambient atomic force microscopy images of ZnTPP with sub-molecular resolution". *Manuscript in preparation*

Edward Juan Dunn, Robert Young and Samuel Paul Jarvis. "Simulation of Constant Force Atomic Force Microscopy for High Resolution Imaging of Non-planar Molecular Structure". *Manuscript in preparation*

Conference Presentations

European Materials Research Society 2022 Spring Meeting (Online)

- Oral Presentation - "Probing TMD defects with atomic scale probe microscopy"

29th General Conference of the Condensed Matter Division of the European Physical Society (Manchester)

- Oral Presentation - "Correlating the electronic and chemical structure of defects in TMDs with atomic resolution conductive microscopy"
- Oral Presentation - "Simulated imaging of submolecular structure in molecules with high topographic variation"

European Conference on Surface Science 35 (Luxembourg)

- Oral Presentation - "Atomic defects in TMDs: revealing electronic and chemical structure with conductive microscopy"

Interdisciplinary Surface Science Conference 24 (Manchester)

- Oral Presentation - "Identifying point defects in transition metal dichalcogenides with true atomic resolution"

Condensed Matter and Quantum Materials 2023 (Birmingham)

- Oral Presentation - "Ambient characterisation of atomic defects in transition metal dichalcogenides with single atom resolution"

Microscience Microscopy Congress 2023 (Manchester)

- Oral Presentation - "Ambient, true atomic resolution of point defects in transition metal dichalcogenide monolayers"

Contents

List of Tables

List of Figures

Chapter 1

Introduction

1.1 Why do we use microscopes?

"In general, a science involves a pursuit of knowledge covering general truths or the operations of fundamental laws" [1]. As humanity pursued knowledge and established fundamental laws for understanding the world, science began to have great predictive power over matters in our everyday experience. As a result, many active areas of research in physics are concerned with pursuing knowledge of systems we cannot observe with our unaided senses. For example, Cosmology studies phenomena on vast scales and concerns events that are not only separated from us by great distances but also by an unimaginably large stretch of time. Telescopes of various kinds are constructed in order to gather data on such exotic conditions.

Although exotic phenomena may seem far removed from everyday life, in many ways our lives have been transformed by the discoveries in these areas of physics. The desire to share scientific information prompted Tim Berners-Lee to develop the World Wide Web whilst working at CERN in 1989 [2] and the computing that is so central to life in the 21st century relies on semiconductors which derive their properties from quantum mechanics.

Microscopes offer a window into the world of the very small, enabling work on the scale of micrometres and, more recently, nanometres and Ångstrom. The basic

principles of Nanoscience were outlined by Richard Feynman in his seminal 1959 talk "Plenty of Room at the Bottom" in which he argued that an incredible amount of information could be stored on even the head of a pin if we gained the ability to manipulate matter at a small enough scale [3]. To work at such length scales it is critical that we can resolve the outcome. Thus the advancement of science on the nanoscale requires accessible microscopes that can keep up.

Tools of magnification have been in use since ancient times in the form of balls of water and glass [4], but devices we would recognise as microscopes only began to take shape in the early modern era. The inventor of the first compound microscope, where two lenses are put together, is lost due to a lack of evidence and competing claims [5]. However, the impacts of the first microscopes are clear.

Robert Hooke was an early adopter of the microscope and his observations of cork revealed compartments which he named 'cells'. These cells are now widely understood to be an almost fundamental unit of life due to following experiments by subsequent researchers such as Antonie van Leeuwenhoek who observed animal cells and single-celled organisms. Observing micro-organisms was critical to understanding, and thus combating, disease and remains crucial to the development of medicines.

The resolution of an optical microscope is limited by the particles that it uses. Photons of visible light have wavelengths in the range 380 - 750 nm. The resolution of a microscope that uses lenses is proportional to the wavelength of the particle detected and has the same order of magnitude. As a result, improvements in resolution required the ability to reliably detect particles with shorter wavelengths. Electrons are massive and charged, offering an ideal alternative to the photon because their wavelength can be made smaller than that of a photon and the charge ensures that they interact with electric fields. The use of electrons became possible with the development of magnetic lenses in the early 1930s and electron microscopy began as a part of these experiments.

With the electron microscope, the interior of cells became visible and, at high

energies, lattices of atoms could be observed. Because electrons can interact with matter in numerous ways, additional detectors can be added to the system to gain insight into the chemical composition and the distances between atoms in a crystal. Electrons which travel all the way through the material can be used to create images in a similar way to the X-ray imaging which is commonplace in hospitals. The transmission of electrons through the material is blocked by atoms at different rates depending on their atomic number. However, some electron microscopy is carried out using the electrons that re-emerge from the surface the beam entered from. This enables the imaging of thicker materials as electrons lose energy as they travel deeper into the sample until they cannot escape. The surface closest to the beam can be studied without thinning the sample by imaging electrons which return. 'Secondary electrons' originate from near this surface and enable sensitive imaging of topographic details, whilst 'backscattered electrons' penetrate further into the material and are sensitive to the atomic number of the atoms the electrons interact with. X-rays emitted when electrons from the beam scatter in the material are able to emerge from much deeper into the material than electrons, yielding information about the bulk of the crystal rather than just the surface. Further insight comes from low energy electron diffraction (LEED), commonly used to verify the growth of thin films and to study surface reconstruction [6, 7].

These new microscopes allowed researchers to observe features inside biological cells and study materials on length scales where material properties originate, further expanding our understanding of these systems. However, there remained some drawbacks to electron microscopy.

The electron microscopy techniques that can resolve individual atoms (transmission electron microscopy and scanning transmission electron microscopy) require exceptionally thin samples to ensure that sufficient numbers of electrons pass through the material and the resulting image flattens the information into a two-dimensional image. The non-transmission technique, the scanning electron microscope (SEM), requires conductive samples in order to drain the electrons

from the sample and high energy electrons incident on a sample surface can initiate chemical reactions which change the subject dramatically.

The work in this thesis regards a form of microscopy that uses no lenses and can be used to manipulate materials on the nanoscale. Scanning probe microscopy offers high-resolution imaging down to the atomic scale through the use of a sharp tip interacting with the surface over very small length scales. There are two main techniques, each with a plethora of variations which make scanning probe microscopy exceptionally versatile. Scanning tunnelling microscopy offers users the ability to observe the surface of conductive materials and the ability to collect spectra which inform the user about the energies of electrons near the surface. The other scanning probe technique, atomic force microscopy and its many modes open the scope of SPM to insulating samples and enable the measurement of a host of properties, such as thermal and electrical conductance.

Using SPM, images of the atoms inside molecules have been created [8] and changes in the energies of electrons can be measured at specific locations, illuminating how defects change crystals locally [9].

As discussed, the sharp tip interacts with the surface, meaning that pieces of material can be moved around the surface to design systems as well as image them. This has led to exciting lithography on extremely small length scales and the creation of quantum simulations of simple crystals and molecules [10, 11]. Of course, scanning probe microscopes are primarily microscopes and in this work, I will consider two interesting systems using the application and simulation of atomic force microscopy.

Two-dimensional materials have been regarded with excitement because they frequently possess favourable properties compared to their three-dimensional counterparts, leading to a potential for improvements in many sectors, but more importantly, they also possess unique properties of their own. The confinement to two dimensions results in low electrostatic screening and changes to the band structure. One effect is an increase in the lifetime of bound states involving electrons called excitons [12, 13].

In addition, all of the atoms in two-dimensional materials are close to the surface, meaning that all defects are visible and their position is simple to determine. Because scanning probe techniques only interact with the surface of a material, they don't pick up signals from deep inside the substrate the sample is placed upon; this makes them ideal for studying two-dimensional materials. The depth to which a technique it sensitive varies between techniques, but the each achieves high resolution by utilising short range interactions. It is possible to place a two-dimensional sample over a grid, enabling the user to collect images using transmission electron microscopy techniques. Exceptionally high-resolution images of 2D materials have been created in this way, but scanning probe techniques offer invaluable additional information. The transmitted electrons are sensitive to the atomic number of the imaged atoms, but the marginal difference in contrast between light elements means that some elements are difficult to observe. The multi-modal approach of scanning probe techniques means that changes in the height of atoms, variations in the states of electrons and even variations in the magnetic field can all be used to provide additional information to identify a defect.

I will present two studies showing how defects on the scale of individual atoms can be observed with atomic resolution in ambient conditions using conductive atomic force microscopy. In the first study, I will show that the density of defects in monolayer transition metal dichalcogenides can be surveyed and that different types of defects can be differentiated. All electron microscopy techniques operate in a vacuum environment and the scanning probe microscopy techniques that are typically used to collect such data face significant challenges when operating in ambient conditions or on surfaces with contamination. In developing a more robust technique we allow the user to observe samples created with techniques that may leave residues behind and to observe them in environments which may better resemble those in which the device will be used.

In the second study, we show how these benefits can be exploited to conduct new exciting research. We fabricated samples using mechanical exfoliation, which

is prone to polymer residues, and then created new defects via exposure to a N_2 plasma. In conductive atomic force microscopy images before and afterwards we were able to see changes in defect density and type despite the sample being exposed to an ambient environment for long periods. Further to this, we show that the creation of these defects leads to changes in the light emitted from the samples when illuminated. By introducing defects with a plasma, an unpredictable distribution of new defects will form which, if they vary on a suitable length scale, could be used to identify it by illuminating the sample and measuring the response. Security tags based on the properties of physical devices are a key part of multi-factor authentication [14]. New ways to create such devices are being explored which can be fabricated in a cost-efficient manner. Ideally, the signal from the device cannot be predicted before measurement, but once measured the device can be relied upon to reproduce the same signal in the future. Devices which can be made to produce multiple reliable signals are ideal as each signal can be used exactly once to prevent eavesdroppers from replicating the signal. The ability to make such a device with defects in 2D materials can be explored with many possible parameters such as the frequency and intensity of the illuminating light which can be varied to acquire a range of responses.

Along with 2D materials, this thesis concerns porphyrin molecules on metallic substrates. Tetra-phenyl porphyrin molecules are interesting subjects for the study of how molecules conform to a surface because they strike a balance between complexity and clarity. One can observe the rotation and distortion of parts of these molecules, but there are few moving parts, enabling researchers to focus on these features.

Porphyrins with metallic atoms 'complexed' into the centre are key to many processes which are fundamental to life [15]. Haem, a molecule that is critical in the transport of oxygen around the body, contains a porphyrin core complexed with an Fe atom. The various forms of chlorophyll contain a porphyrin core with a Mg centre and vitamin B12 (cobalamin) is has a Co complexed corrole core which is

very similar. Zn tetra-phenyl porphyrin (ZnTPP), which is important to this work, has been considered for molecular electronics applications [16].

Here we will simulate the application of constant force atomic force microscopy techniques to simulate a range of molecules including ZnTPP and study how it conforms to a particular surface of Au crystals.

1.2 Outline

This thesis has a structure of 8 chapters. In this chapter the role that microscopes play in the development of technology has been explained, along with the necessity of improving the resolution of microscopes and increasing the variety of samples that can be studied.

The work carried out in this thesis has focussed heavily on the development of measurement techniques in order to push the limits of resolution in a particular environment. As a result I will explain the important characterisation techniques first in 'Scanning probe microscopy techniques and optical spectroscopy' (Chapter 2).

Having established these techniques I will then discuss the materials studied in this work. This 'Materials' chapter (Chapter 3) will focus on two systems: two-dimensional materials and molecules on surfaces. For each system I will introduce theoretical frameworks for understanding the system and then discuss the literature on how these systems have been fabricated and characterised, especially through the techniques discussed in Chapter 2.

In 'Methods' (Chapter 4) the details of the experiments and simulations used to obtain the results outlined in the following chapters will outlined. The findings of this degree are separated into three chapters; each focussing on a separate goal. In 'Results: formative defect density in transition metal dichalcogenides' (Chapter 5) the ability to survey the defects present in mechanically exfoliated samples with atomic resolution and to compare the results is demonstrated. Following this, in

'Results: creation of defects in transition metal dichalcogenide monolayers' (Chapter 6), details our progress in elucidating how the introduction of further defects in transition metal dichalcogenides changes the optical properties of the crystals. The final chapter on my findings, 'Results: simulation of constant force atomic force microscopy' (Chapter 7), demonstrates how images created via 'constant force atomic force microscopy' methods can be interpreted by simulating images from atomic coordinates. In addition, the viability of measuring the angle between a section of a molecule and the substrate with such techniques is shown for an idealised microscope along with my progress towards interpreting images of a network of zinc tetraphenyl porphyrin molecules taken with a constant force technique.

The advances presented in this thesis and future research avenues will be summarised in 'Conclusions' (Chapter 8).

Chapter 2

Scanning probe microscopy and optical spectroscopy

This thesis focusses on the development of characterisation techniques. In order to review the literature studying the materials of interest for this thesis it is first necessary to introduce the methods by which those materials will be characterised. In this chapter I will first explain a group of microscopy techniques called scanning probe microscopy which includes atomic force microscopy, a technique used commonly throughout this thesis. The other important method of characterisation in this thesis, optical spectroscopy, will be discussed. Together the techniques give the user the ability to observe a specific region in detail with microscopy and gather information over a broader region with spectroscopy.

2.1 Development of SPM

2.1.1 Scanning tunnelling microscopy

The field of scanning probe microscopy (SPM) began with the invention of the scanning tunnelling microscope (STM) in 1981 [17]. Key to the invention is the ability of electrons to tunnel through regions where they would be forbidden from

entering classically. One of the first systems a student of quantum mechanics will ever encounter is the idea of the particle in one dimension. The particle may move left or right, but regions with an infinitely high potential can stand in its way. The wavefunction, which describes the probability of measuring the particle at a point in space, must be zero inside the potential barrier because there is no probability of finding it there. Such constraints can define the states a particle may have if two barriers confine it in a space with a similar size to the particle's wavelength. If the barrier is not infinitely high, however, there is a possibility of transmission. In classical physics, the particle must have enough energy to overcome the potential barrier, but in quantum physics, there is always a chance, even if it is negligible, of the particle penetrating the barrier. In the case of STM, carriers pass between states in a sharp tip and the sample by tunnelling through the vacuum between.

Figure 2.1 shows a diagram of how tunnelling in one dimension is considered in quantum mechanics. The wavefunction for a particle of energy E through a potential barrier characterised by its potential $U > E$ and its width d. The current that tunnels through this barrier decays exponentially as either U or d increases. Because of this, $I \propto e^{-\kappa d}$, where κ characterises the exponential decay. This relationship between I and d was one of the first topics to be probed by Binnig *et al.* when STM was invented [18].

It is clear that small changes in the distance between the tip of an STM and the sample can be measured with great sensitivity using the current. STM can be carried out by scanning the STM tip in a raster pattern at a constant height, measuring variations in the height of the surface. However, this mode of operation requires exceptionally flat surfaces so 'constant current' STM, where the height is varied to maintain a constant current is often preferred. In both cases, either current or tip height is kept constant and the other is plotted as the signal. This fine motion is carried out by using piezoelectric actuators. The actuator crystals expand when a voltage is applied, enabling the user to move the sharp tip over very small distances with precision.

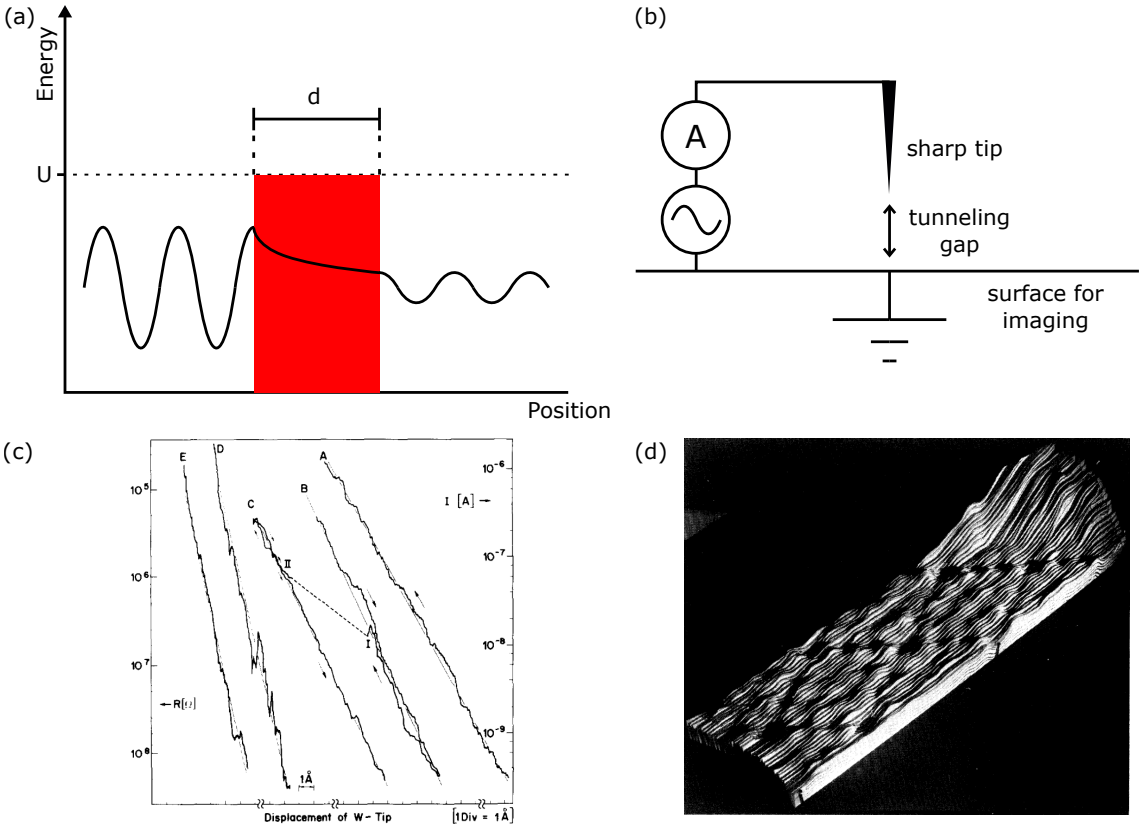

Figure 2.1: *(a)* For finite barriers requiring a potential energy U to overcome classically and a width d, the magnitude of the wavefunction (line overlaid on the diagram of potential energy) of an electron drops exponentially as it travels further into the barrier (red), but remains non-zero. *(b)* STM measures the tunnel current between a sharp tip and a sample or surface when a bias is applied. *(c)* Increasing the distance to the sample leads to an exponential decay in the tunnel current, depicted in this figure (Reprinted from *Binnig et al.* [18] with the permission of AIP Publishing) from the first paper on the topic by Binnig *et al.* . *(d)* Later the same year, the 7×7 reconstruction of Si was measured by the same authors (Reprinted figure with Permission from Binnig *et al.* [19] Copyright (1983) by the American Physical Society).

The first great success of STM imaging was the observation of the 7×7 reconstruction of Si(111) (Figure 2.1) [19]. The nature of this surface had eluded researchers using diffraction methods; they could postulate a set of possible surfaces, but couldn't determine which reconstruction it was. STM proved definitively which reconstruction occurs and thus its own utility. Because STM relies on a tunnelling current it is restricted to conductive surfaces, similar to SEM. However, it is important to be able to image insulating surfaces and samples upon those surfaces.

2.1.2 Atomic force microscopy

By placing an STM tip above a cantilever with its own sharp tip, AFM was realised. Forces from the surface deflected the cantilever and varied the tunnelling distance between the cantilever and the STM tip, enabling force to be used as a feedback variable. This was cumbersome though and AFM has been predominantly carried out via the 'beam deflection' or 'qPlus' methods.

In the beam deflection method, a laser reflects from the top surface of the cantilever and the deflection of the cantilever moves the laser spot on a photodiode, as depicted in Figure 2.4. By splitting the diode into four quadrants the motion can be separated into vertical and horizontal components; allowing the user to measure vertical and lateral force components acting on the tip. The qPlus technique is a specialist technique discussed in Section 2.4.2.

2.1.2.1 The Lennard-Jones potential

The remarkable resolution of SPM comes from the ability to observe features that have dimensions smaller than the tip. This shares many similarities with record players, where the sharp needle is guided by grooves with smaller dimensions than itself. This phenomenon is due to the short-range interactions that dominate the forces applied to objects close to a surface.

An AFM tip apex experiences the Lennard-Jones potential (Figure 2.2) as it approaches the surface. This potential applies a small attractive force that grows

dramatically close to the surface. However, as the tip pushes further in, the dominating factor of the Lennard-Jones potential switches to Pauli repulsion which results in a potential well and a high energy cost for pushing the tip further into the surface. The rapid onset of these forces at such short ranges means that the very closest part of the probe is experiencing a radically different force to the rest. It is this factor that allows needles to be guided along grooves that are smaller than their tip and for AFM tips to resolve features smaller than themselves. STM can be considered to behave similarly because the tunnelling current depends exponentially upon the tip-sample distance [20].

2.2 Contact mode atomic force microscopy

A host of AFM techniques emerged measuring variations in the magnetic field, electrical potential, conductivity and more, but all were based on a set of topographical techniques [21].

The simplest technique is contact mode. The tip approaches the surface until the cantilever deflection reaches a desired value. Then the tip is scanned across the surface, whilst the deflection is maintained by varying the height. The simplicity of such a technique makes it very robust, but the high contact forces can wear and blunt the tip apex, reducing the resolution.

2.3 Conductive atomic force microscopy

Conductive atomic force microscopy (cAFM) is a contact AFM mode used to observe nanoscale changes in conductance. The height of the tip is determined by using deflection feedback in contact mode, but a bias voltage is set up between the sample and the tip. By coating the probe in a conductive material, a current between the tip and sample can be induced and measured to infer the local conductance.

cAFM has been demonstrated as a technique for establishing variations in

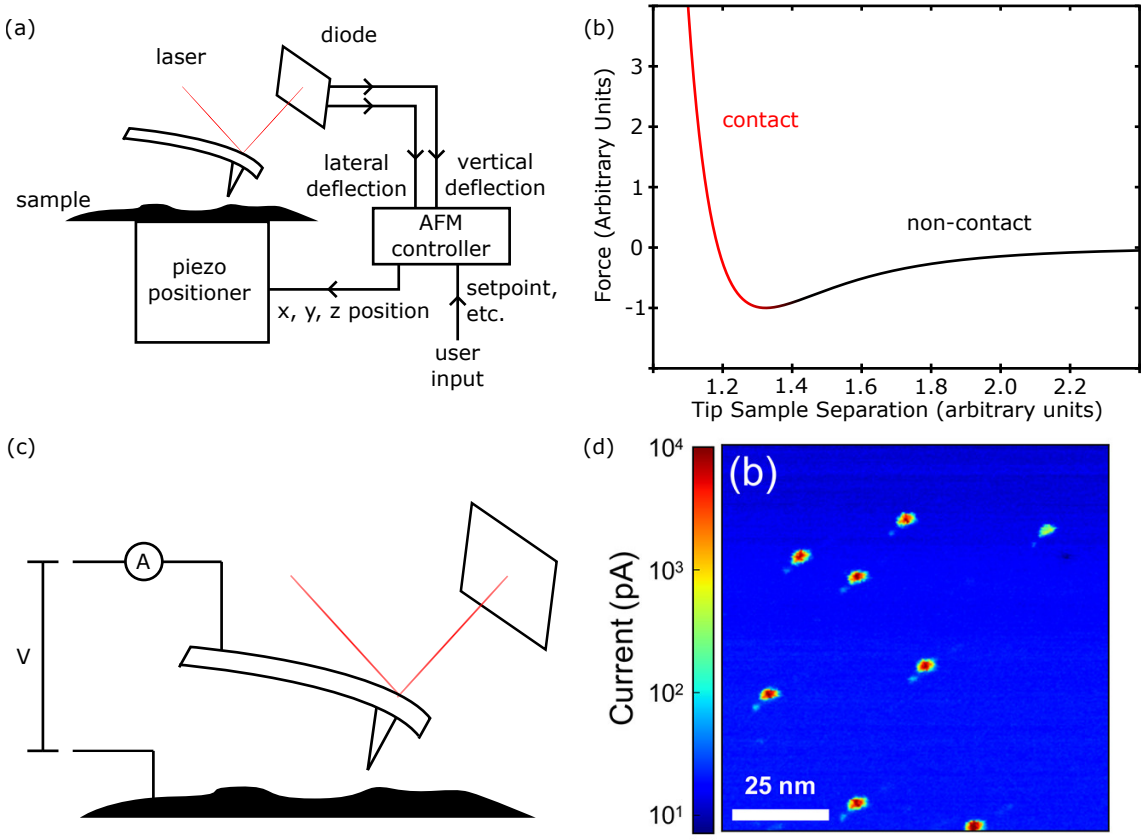

Figure 2.2: Contact mode atomic force microscopy is operated by measuring the deflection of a cantilever with a laser. *(a)* The laser is positioned so that it reflects off the top side of the cantilever and onto a diode. Changes in the position of the laser as it hits the diode are used to determine the deflection, which is then sent to a controller. The controller can change the height of the sample using the piezoelectric positioning system whilst moving the sample in x and y. *(b)* The force experienced by the cantilever can be described using the Lennard-Jones potential which becomes suddenly repulsive near the surface. This repulsive section is considered to be in contact. *(c)* In order to carry out cAFM a bias voltage is set up between a conductive probe and the sample. *(d)* In a conductive sample, a current will flow which can be measured to determine the local conductivity, for example, the conductivity increases when the tip scans over defects in WS_2. Reprinted (adapted) with permission from Rosenberger *et al.* [22]. Copyright 2018 American Chemical Society.

conductivity due to spatial position and as a static technique where the voltage is swept to probe conductivity as a function of voltage.

Spatial maps allow us to observe changes in the conductivity of different materials, phenomena such as Moiré patterns [23] and, importantly, the observation of defects [22]. The images collected by this technique will likely call STM to the mind of any material scientist and it is through comparison with STM that one can best highlight the strengths and weaknesses of cAFM. Like STM, cAFM measures the electronic properties of a material, requiring a conductive substrate as a result. There are three major differences: that STM is a non-contact technique, allowing for better preservation of tip apices; that STM measures a tunnel current rather than via direct conduction; and, crucially, that the feedback mechanism of STM uses current as the feedback variable rather than deflection.

The fact that cAFM tips experience the much greater forces of the 'contact' region means that tip apices are likely to become blunted, reducing the lateral resolution. STM can also operate across a range of tunnel currents, optimising the tip-sample distance for the task to be carried out. These factors make STM a preferable instrument for many samples, however, the use of current feedback can cause problems. In order to scan effectively, STM needs a clear current signal and if the measured signal is below the current set-point, STM approaches the sample. In this way, picking up contamination on an STM tip can cause the tip to crash into the sample and create difficulties for measurements in the band gap of semiconductors. For this reason STM users often measure in an ultra high vacuum environment, avoiding these problems. Because cAFM uses a deflection feedback system it operates in a manner closer to constant height STM, where the tunnelling current is measured with feedback off.

In this thesis we study the defects present in mechanically exfoliated transition metal dichalcogenides (TMDs). The details of our mechanical exfoliation process will be outlined in Section 4.3.1, but the aspect that is crucial for selecting SPM techniques is that mechanical exfoliation necessitates the exposure of the TMD flakes

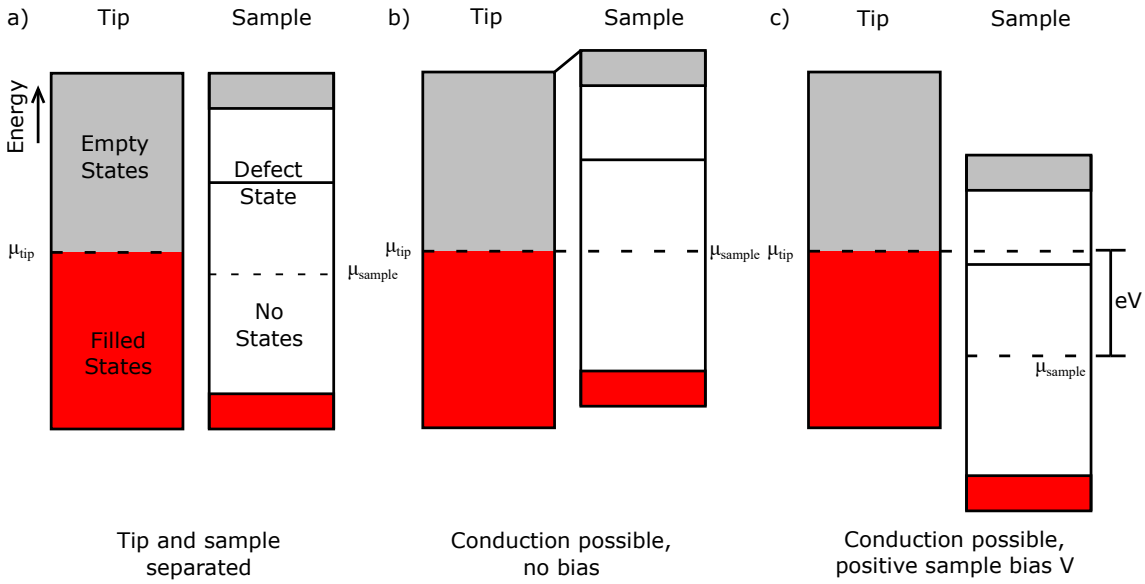

Figure 2.3: A diagram of the band structure of the tip and sample applicable to cAFM and STM. *(a)* When no current can flow between the tip and sample the chemical potential (μ) in the tip and sample will be different. The states below μ will be filled with electrons and those above will be empty. If a sample is semiconducting, as depicted here, the chemical potential will lie in a region with no states. *(b)* When a current can flow between the tip and sample the band structures will become offset in order to align the chemical potentials, reaching a state of equilibrium where no current flows. *(c)* In order to induce a current a bias voltage must be applied, moving empty states on one side to lower energies than the filled states on the opposite side. In the diagram a defect state moves below the μ of the tip.

to polymers which can cover the flakes. Due to the need to prevent the exposure of STM tips to surface contaminants there is a tendency for samples prepared via cleaner techniques to be studied via STM [24, 25]. The more robust nature of a deflection feedback system makes cAFM an ideal technique to study point defects in mechanically exfoliated TMDs. If contamination is picked up by a cAFM tip it affects the signal but does not result in a fatal crash.

As discussed, mapping conductance spatially is not the only way to carry out cAFM. The bias voltage can be varied at a particular location in order to provide spectroscopic information about the band structure. By applying a sample bias empty states on one side of the junction fall below the chemical potential (μ) of the

opposite side, such as in Figure 2.3, letting charges travel between the tip and sample. As the voltage changes the states that are filled or depleted changes, meaning that the local density of states can be probed by finding the derivative with respect to the voltage [22]. By sweeping the bias voltage, the conductance of the tip-sample system can be extracted, revealing information about transport through defective regions and molecules [22, 26].

2.4 The dynamic modes

In dynamic mode the cantilever is driven near resonance. Similar to STM, dynamic mode AFM can be carried out at a constant height or with feedback. The variables are height and either the amplitude or resonant frequency of the cantilever oscillation.

The resonance is described by a sum of forces [27, 28]. As the cantilever oscillates away from its equilibrium position by distance z it experiences a restorative force characterised by its Hooke's constant k, forces proportional to the velocity by the complex constant γ and the driving force $F_D(t)$. When brought close to a surface an AFM cantilever will also experience forces from the surface which will be considered once a discussion of harmonic oscillators has been completed. $\gamma = \gamma_1 + i\gamma_2$ describes both the dissipative forces that resist the motion as drag forces or intrinsic damping $\gamma_1\dot{z}$ and those which originate from the mass of any viscous fluid dragged along by the resonator $i\gamma_2\dot{z}$. When considered together, the acceleration of a cantilever of effective mass m may be found, yielding a second order differential equation.

$$m\ddot{z} = F_D(t) - kz - \gamma\dot{z} \tag{2.1}$$

Let us build up our picture by first considering the simple harmonic oscillator where damping is neglected and there is no driving force. Here $m\ddot{z} = -kz$ and using the ansatz $z(t) = z_0 e^{\lambda t}$ we find that $\lambda = i\sqrt{\frac{k}{m}}$. The imaginary nature indicates that this is an oscillation with no loss of energy because the magnitude of $e^{\lambda t}$ is unity

whilst the index remains imaginary. Let us name the angular frequency of oscillation the natural frequency $\omega_0 = \sqrt{\frac{k}{m}} \in \mathbb{R}$.

If the oscillator is damped it loses energy and, in the absence of a driving force, it decays. A damped harmonic oscillator is described by $m\ddot{z} = -kz - \gamma\dot{z}$ and using the ansatz $z(t) = z_0 e^{\lambda}$ again we find a different answer: $\lambda = -\frac{\gamma}{2m} \pm \sqrt{\frac{\gamma^2}{4m^2} - \omega_0^2}$. Because $\gamma \in \mathbb{C}$ we can split this into real and imaginary parts. In the underdamped case, which most closely resembles a driven oscillation, the cantilever oscillates near the natural frequency. For small frequency shifts, the imaginary part should be similar to ω_0, meaning that $\lambda \sim -1/\tau + i\tilde{\omega}$ where the oscillation decays with a lifetime $\tau \sim \frac{2m}{\gamma_1}$ and the new resonant frequency $\tilde{\omega} \sim \omega_0 - \frac{\gamma_2}{2m}$. The shift in the frequency $\Delta\omega = \tilde{\omega} - \omega_0 \sim -\frac{\gamma_2}{2m}$ as a result.

Applying a driving force oscillating in time t with amplitude F_0 and angular frequency ω yields $F_D = F_0 e^{i\omega t}$, enabling the cantilever to sustain a continuous oscillation. If it is driven far from resonance the cantilever will oscillate at this driving frequency, but near ω_0, the cantilever will adopt its resonant frequency $\tilde{\omega}_0$.

By using the solution $z(t) = z_0 e^{i\omega t}$, we can find the oscillation amplitude z_0 as a function ω:

$$z_0(\omega) = \frac{F_0}{m} \frac{\omega_0^2 - \omega^2 - \omega\gamma_2/m - i\omega\gamma_1/m}{(\omega_0^2 - \omega^2 - \omega\gamma_2/m)^2 + \omega^2\gamma_1^2/m^2} \sim \frac{F_0}{m} \frac{\omega_0^2 - \omega^2 - 2\omega\Delta\omega - 2i\omega/\tau}{(\omega_0^2 - \omega^2 - 2\omega\Delta\omega)^2 + 4\omega^2/\tau^2} \tag{2.2}$$

This is a Lorentzian curve, depicted in Figure 2.4, which resonates when the denominator comes as close to 0 as possible. From this, the value of $\tilde{\omega}_0$ can be extracted and it is found to be $\sim \omega_0 - \frac{\gamma_2}{2m}$ for small deviations from ω_0, just like in the damped oscillator. The tip surface interaction damps the oscillation, leading to the shift $\Delta\omega$ which can be used as a feedback variable.

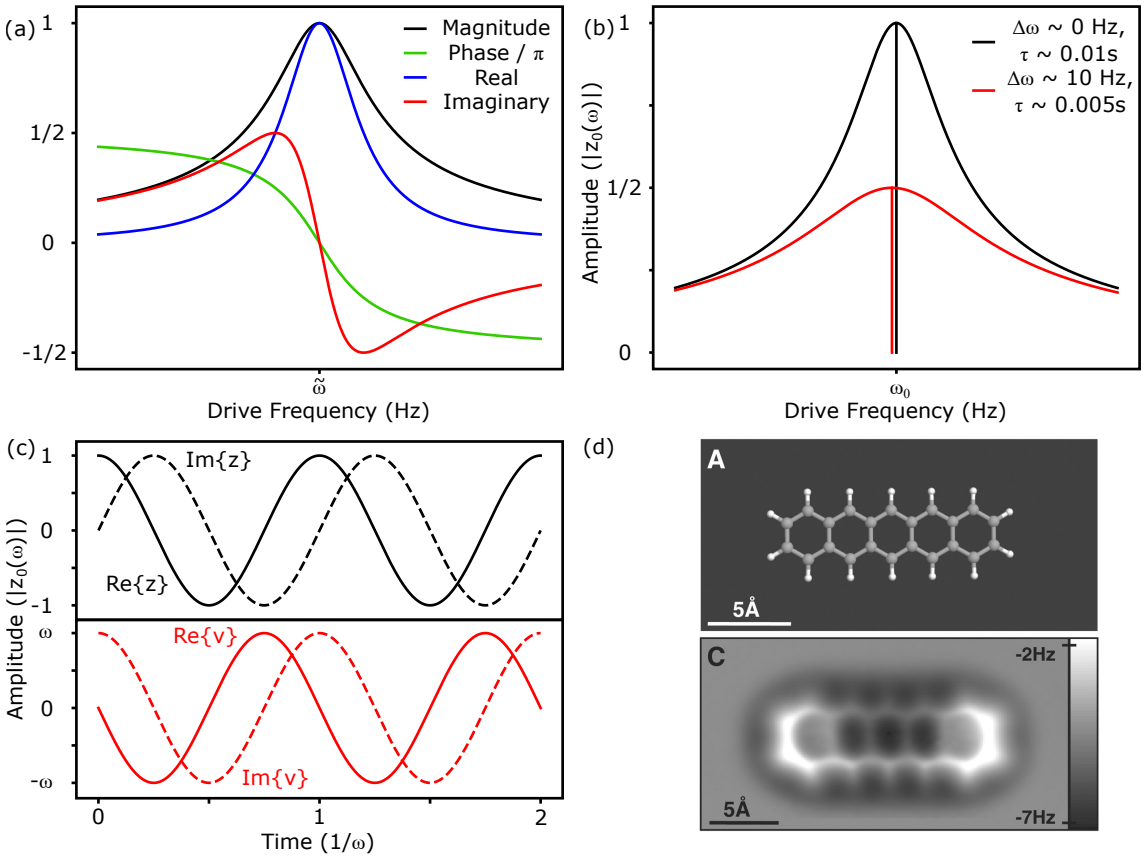

Figure 2.4: *(a)* The dependence of the oscillation amplitude of a resonator with $\Delta\omega = 0$ Hz, $\tau = 0.01$ s and $\omega_0 = 2{\times}10^5$ Hz on the frequency ω of a driving signal with amplitude i. Using these values we can calculate this dependence, showing that the magnitude peaks at the resonant frequency $\tilde{\omega}$. The real part reaches it's maximum at $\tilde{\omega}$ whilst the imaginary part passes through 0. Representing the amplitude as a complex number encodes the phase relative to the oscillator at resonance. *(b)* The damping force due to γ_1 results in a broadening of the peak, a decrease in the amplitude and shorter value of τ. Damping due to γ_2 can lead to a shift in $\tilde{\omega}$ to lower frequencies ($\Delta\omega$). *(c)* The position and the velocity are $\pi/2$ out of phase, which is encoded in the complex numbers representing them. *(d)* NC-AFM, a form of frequency modulation AFM, can be used to acquire images of planar molecules such as pentacene where the structure of the molecule is clearly resolved. From Gross et al. [8]. Reprinted with permission from AAAS.

2.4.1 Amplitude modulation atomic force microscopy

Amplitude modulation dynamic mode AFM is most commonly used in ambient environments. By interacting only during a brief contact at the bottom of the oscillation cycle, the lateral forces can be minimised and the maximum force experienced during a cycle can be kept relatively low, preserving the tip apex. The dissipative forces experienced due to interaction with the surface shift the resonant frequency as $\Delta\omega \propto \frac{-dF_{ts}}{dz}$ where F_{ts} is the tip-sample interaction. This force has an effect akin to damping, shifting the resonance peak similar to in Figure 2.4b) and, because of this, varying the amplitude. The driving frequency is set close to the resonant frequency and then, the peak shifts due to the tip-sample force, changing the amplitude at the drive frequency. Because the slope of the resonance curve is very steep close to resonance, small changes in frequency shift lead to big changes in the oscillation amplitude, allowing it to be used as a feedback variable.

When the tip sample interaction changes the cantilever takes some time to adjust to the new environment. The lifetime of the loss of energy should be similar to τ [17]. This lifetime is adequate in ambient conditions, where γ is large so τ is small, however, in a UHV system τ leads to very long measurement times.

2.4.2 Frequency modulation and non-contact atomic force microscopy

Long measurement times are not only tedious, they also increase the influence of thermal drift and other effects which can be suppressed by making measurements shorter. As a result, it is important to have faster measurement speeds in order to maintain the quality of the measurements.

The solution that is commonly implemented in the ultra high vacuum environment is to measure the change in the resonant frequency rather than the amplitude. The resonant frequency changes on a timescale of τ_f [17].

$$\tau_f = \frac{2\pi}{\tilde{\omega}_0} \tag{2.3}$$

Frequency modulation AFM in a constant height mode is referred to as Non-Contact Atomic Force Microscopy (NC-AFM). The technique is named after the typical operation of this imaging mode; the distance from the sample is selected such that only the closest objects are imaged via Pauli repulsion. This approach minimises the forces on the tip, preserving the apex, but moves close enough to the surface to begin to see the strong dependence of the force on the distance to the sample.

The images in NC-AFM are collected by measuring the frequency of the oscillating cantilever and simply plotting the shift in resonant frequency relative to the natural frequency.

Many NC-AFM images are collected using the qPlus technique rather than the beam deflection technique. To use this technique, a quartz tuning fork is stimulated into harmonic motion using a drive voltage because of its piezoelectric properties. The current in the circuit can then be measured to track changes in the resonance frequency and oscillation amplitude, from which the tip-surface forces can be inferred.

This technique is almost exclusively used in a UHV environment at low temperatures, where it can be used to acquire images with incredible stability and detail. In particular by picking up a carbon monoxide (CO) molecule at the tip apex the technique can be used to obtain images with exceptionally sharp sub-molecular resolution.

In 2009 the first images created using CO functionalisation were published, indicating the position of the atoms within a pentacene molecule [8]. This presents a significant challenge relative to the imaging of surfaces with atomic resolution because molecules can be moved by interaction with the tip as they are weakly bound to the surface. An image from this paper is shown in Figure 2.4d where it seems like lines have been drawn between the atoms along the bonds. The details

of how this should be interpreted are discussed in Section 2.6.

2.4.3 Off resonance atomic force microscopy

In this work, we consider the more recent 'off-resonance' techniques in detail as they are used to acquire high-resolution topographic images of our samples in an ambient environment and they are a common method of imaging force iso-surfaces, which are simulated in Chapter 7.

As discussed in Section 3.3, molecules on metallic surfaces are often imaged using NC-AFM and STM. Both of these techniques are non-contact techniques, which is important because the force experienced by the subject can be kept very small [29, 30, 31]. Even very small forces can move molecules around the surface, disrupting the network of ZnTPP we would like to observe on Au (111).

As STM convolutes the electronic structure with the geometry of the subject [32], NC-AFM is often used to complement STM in the study of conformation [33, 31]. NC-AFM allows the spatial distribution of orbitals to be ignored as AFM interacts mostly with the dense core electrons around the nucleus itself [34].

NC-AFM is a constant height technique, as detailed in Section 2.4.2, which offers unparalleled resolution within a thin x-y plane but struggles to resolve atoms at other heights. Imaging non-planar molecules with the greatest detail will require the adoption of a feedback variable so that the tip can be moved closer to the sample in order to measure lower sections. In an ambient environment, or even at room temperature in a UHV system, variations in temperature cause expansion that will effectively change the height of the tip. This means that the path of the tip must be reactive, further emphasizing the need for a feedback variable.

Force provides an ideal feedback variable because we would like to maintain a low value. Ideally then, we should use a technique which attempts to maintain a constant, low force and plots the height of the tip when the condition is met.

In the high-resolution techniques used in vacuum environments the tip is driven near its resonant frequency and the frequency shift is commonly used as a feedback

variable. However, it can be difficult to quantify the force that causes the frequency shift on a tip. In ambient environments force has been measured directly by driving the tip well below its resonant frequency.

In nano-mechanical measurements the properties of a material are calculated by pushing an AFM tip into a sample and measuring the cantilever deflection. Because the force on the tip causes a proportionate deflection and the constant of proportionality for the system (k) can be calibrated, the force on the tip can be calculated by multiplying the deflection by k. This measurement is repeated by pushing into the sample repetitively; effectively a low-frequency oscillation. When a tip is oscillated at resonance the interaction with the surface can influence the amplitude and resonant frequency of the tip, but it doesn't change the trajectory of the tip. This means that the force curve from nano-mechanical measurements cannot be obtained near resonance. Nonetheless it is clear that to measure force directly the cantilever should be driven at a frequency that is sufficiently far below the resonant frequency.

In off-resonance AFM methods a force is used as a set point for the feedback and the tip is driven well below the resonant frequency. The value of k is used to convert the deflection signal into a series of force curves with each oscillation creating its own curve. By measuring the oscillation far from the surface a sinusoidal signal can be measured demonstrating the forces experienced by the tip without tip-surface forces. Then the tip is moved down to the surface in order to interact with it. The force data recorded far from the surface can be subtracted from the data measured at the surface, leaving only the tip-surface interaction. The idealized curve and some data collected from a simulation of the tip surface interaction are shown in Figure 2.5.

By integrating the deflection signal across a small window when the tip is closest to the sample, an average force can be measured. By doing so over a sufficiently small period of time a good approximation of the 'peak force' is found. The peak force can then be compared to the set point and used to change the height of the

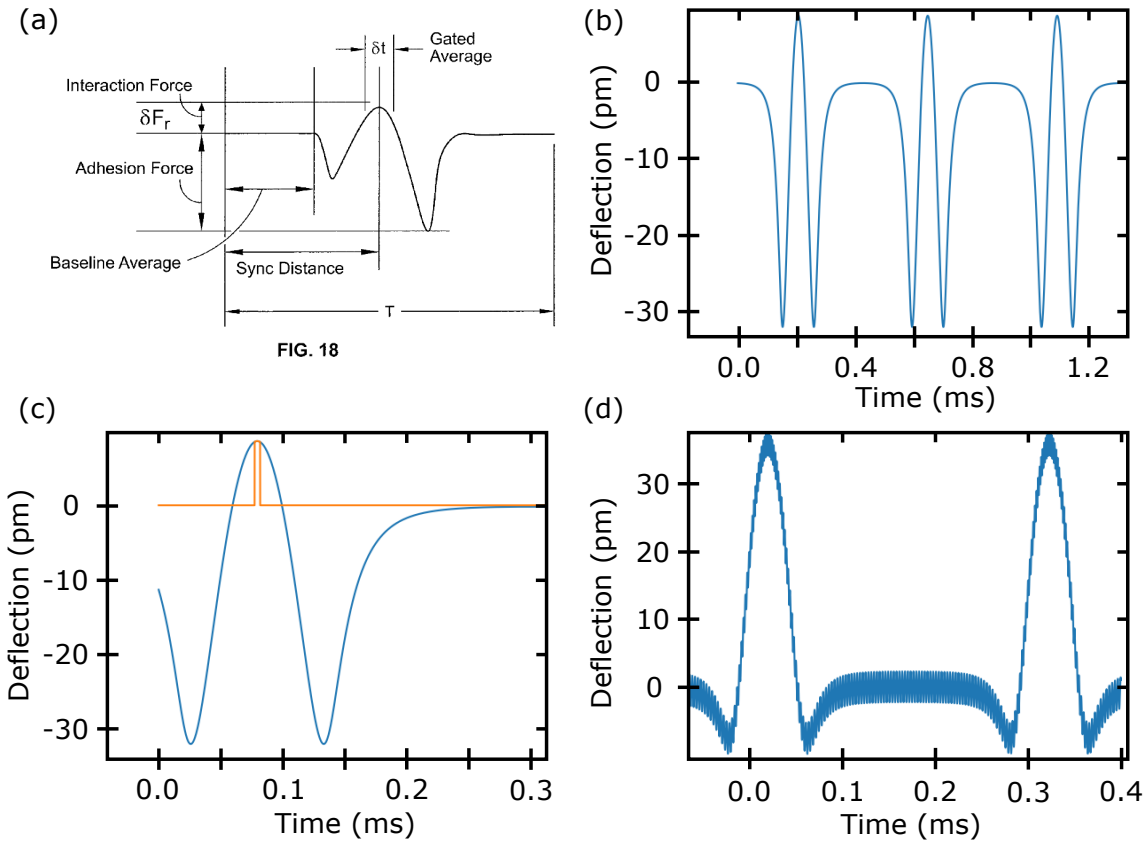

Figure 2.5: The operation of Bruker's Peak Force Tapping Algorithm measures the interaction force by integrating the deflection signal around the point when an AFM tip comes closest to the surface and scaling it by Hooke's constant. *(a)* A cartoon of the desired force (proportional to the measured deflection) from US Patent US8650660B2 [35] is shown alongside results from a simulation of tip oscillations in Python. The interaction force from 3 oscillations creates a pattern in the deflection every oscillation *(b)*. By sampling during a short window, positioned in time using the 'sync distance', each cycle the peak can be isolated *(orange)* and averaged *(c)*. If the damping is too low the cantilever will ring at the resonant frequency, obscuring measurement *(d)*.

tip so that, with a good set of feedback parameters, the force will never rise too high above the set point. In nano-mechanical measurements a significant portion of the contact regime is probed in order to get a large range of data for a linear fit. However, with this constant force technique, we can keep the peak force low so long as the signal can be measured above the noise floor. In fact, off-resonance

techniques can even measure negative (attractive) forces by simply moving the tip away from the surface and maintaining the sync distance.

2.5 Degrees of Resolution

When discussing scanning probe microscopy it is important to define exactly what is meant by resolution. In the simplest terms: an object is resolved when one can distinguish the feature from the rest of the objects in the image. In SPM this is frequently determined by the geometry of the tip apex.

In some cases, the tip is mostly interacting with the surface via a particular atom [17]. Molecular dynamics simulations of AFM tips show that it is reasonably common for a single atom to protrude far enough to dominate tip-sample interactions and the nature of the atom at the apex then has a significant effect on the contrast observed [36, 37, 38]. In order to retain such a tip, great care must be taken to not blunt the apex and, as a result, SPM images are often taken with much lower resolutions.

When an AFM tip scans over a surface, a raised section may interact with the side of the tip first and when descending down a step the sides of the tip may continue to interact with the higher section after the apex has already passed (Figure 2.6). As the tip-surface interaction is used to create the image, the image is as much an image of the tip as the surface. Ideally, an SPM tip is rotationally symmetrical and sharp and this consistency means that we do not observe it's effects. However, when the tip deviates significantly from the ideal, the tip begins to impact the image. When a feature on the surface is sharper than the tip, the feature in the SPM image will be a representation of the tip rather than the sample such as in Figure 2.6.

Resolution can also be affected by the signal-to-noise ratio and whether the feedback gains are correctly chosen. If the signal from features is not large enough for them to be distinguished from the background, the AFM will not be able to respond in a noticeable way to the signal it receives. If this problem is limiting your

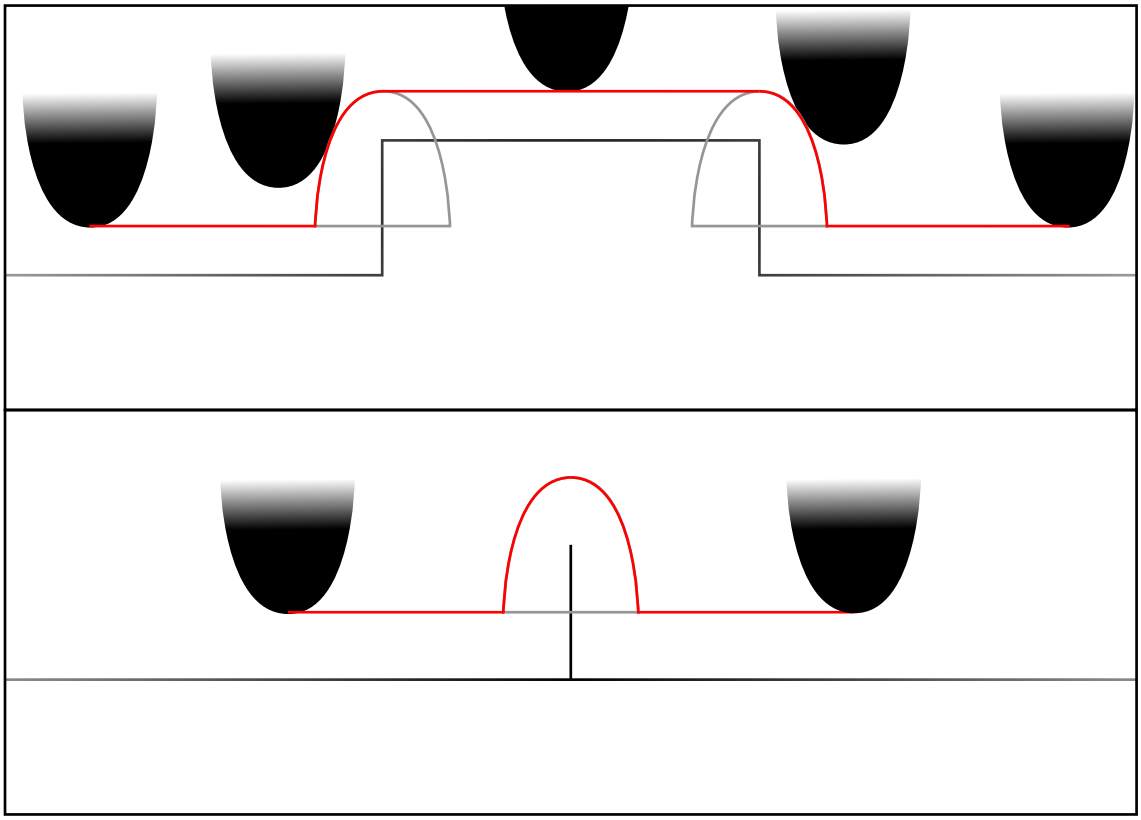

Figure 2.6: A cartoon showing the path (red) that a tip apex in contact mode (other techniques see similar effects) moving from left to right will follow when moving along the surface *(a)*. At a sudden step, a region higher up the tip will interact with the step and lead to the tip rising early and when descending down a step the tip will continue to interact with it after it has passed. Because the measured force is the tip-surface interaction and different parts of the tip are interacting with the same step the tip apex traces out the shape of the tip. If the step was infinitely thin *(b)* the line would simply image the tip apex.

resolution, the noise must be decreased by isolating your AFM from sources of noise or the signal must be increased by measuring a stronger interaction.

There are several specific terminologies relating to resolution that must be defined. When working with molecules sub-molecular resolution is a common benchmark. There is no formal definition and, in practice, it essentially refers to imaging features of the molecule rather than the molecule as a whole. For instance, the imaging of individual moieties such as phenyl rings or lobes in STM from molecular orbitals provides information about the molecule rather than its location and a single apparent height. One could be more strict though and limit sub-molecular resolution to mean the resolution of single 'bonds' like the NC-AFM images discussed in Section 2.4.2. Here we will take sub-molecular resolution to be the broader category.

When working with crystal lattices a key distinction must be made between lattice resolution and atomic resolution. Because the surface of a crystal is a repeating pattern it is possible that one can image this periodicity without imaging individual atoms [25]. An image is said to have lattice resolution if the periodicity of the lattice is seen and it is necessary to be able to show the imaging of an individual atom in order to claim to be measuring with atomic resolution. Typically this means imaging a defect in the crystal where a single atom is missing, such as the defects that will be discussed in Section 3.1.5.1.

2.6 Image interpretation

An image, or indeed any measurement, is only useful if it can be interpreted. As a result, an understanding of how images are produced by SPM techniques is critical to obtaining and using valuable data.

As discussed, STM measures the tunnel current between the sample and tip and this has an exponential dependence on the distance to the sample. There are other factors involved in this process which are key to interpreting STM images. In order

for there to be a net flow of electrons between the tip and sample there needs to be a potential difference V between them. As the V increases, an increasing number of carriers may lose energy after tunnelling, as depicted in Figure 2.3. The number of carriers added to the current as V increases depends on the local density of states (LDOS) within $\pm eV$ of the chemical potential μ. The density of states will be discussed in detail in Section 3.1.2.

Changes in the LDOS due to a change of material or defects lead to changes in the tunnelling current, which can lead to the feedback moving the tip relative to the sample, falsely indicating a change in height. This convolution of the LDOS and tip-sample distance means that one has to be cognisant that a perceived change of height in an STM image may be generated by changes in the LDOS or even by charges shifting the chemical potential locally.

AFM, by contrast, interacts with electrons more generally as it measures the forces between electrons over a much wider range of energies [39]. As the core electron orbitals are densely packed near the nucleus of an atom, each atom can be clearly resolved in NC-AFM.

Further complications for all SPM techniques originate from the tip used, as with the artefacts discussed above. In STM the LDOS of the tip is often assumed to be constant, and therefore having no effect on the data, but realistically this is a simplification. The number of states available for a carrier to tunnel to or from in the tip has just as much effect as those in the sample.

The forces between the tip and sample will, by their nature, deform both parties. In $I(z)$ measurements with an STM the system deviates from an exponential dependence when the tip-sample forces become large. In a study on highly ordered pyrolytic graphite (HOPG) this has been attributed to the forces deforming the sample and changing the density of states due to strain [40, 41].

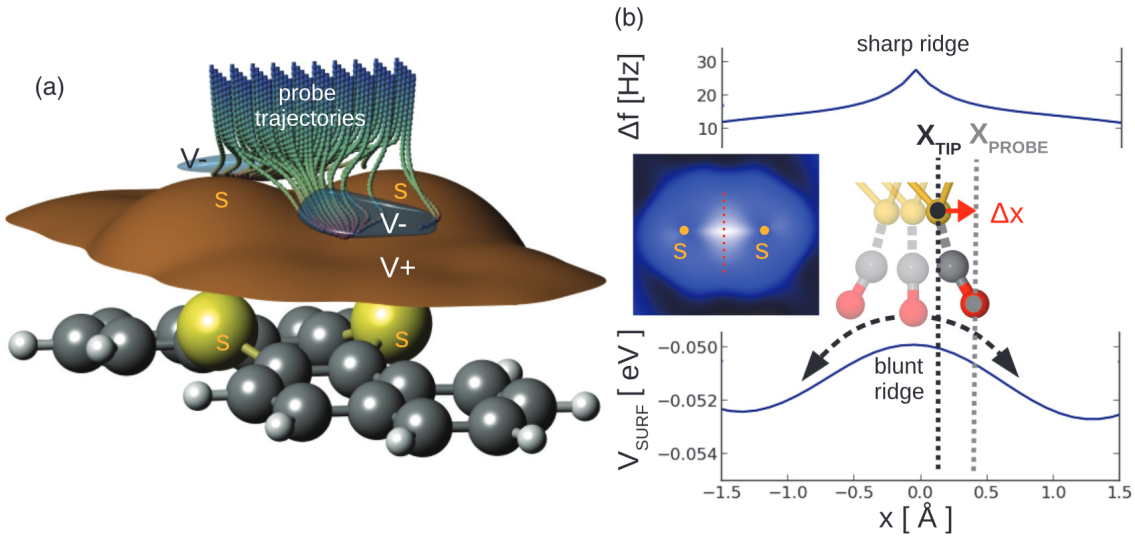

Figure 2.7: This is a figure from the work of *Hapala et al.* on the mechanisms at work in CO tip NC-AFM images. The ridge in the potential iso-surface (brown) above Dibenzo[a,h]thianthrene is due to two Sulfur atoms (yellow) which are not bonded to each other *(a)*. The probe trajectories are deflected as the tip relaxes down the potential landscape. In an NC-AFM image, the watershed between relaxation to one side and the other is the only place where the tip experiences a high force, resulting in a sharp ridge in the image despite the potential surface being much more 'blunt' by comparison *(b)*. Reprinted figure with permission from Hapala P. et al [42]. Copyright 2014 by the American Physical Society.

2.6.1 The Probe Particle Model

As the apex transduces all of the force into the tip the flexibility of the bonds at this position impacts the signal dramatically. The Probe Particle Model (PPM) is a simulation that was developed to interpret NC-AFM images, especially those taken with a CO molecule functionalising the apex [42, 43]. The apex can bend, moving into areas where less force is experienced. This effect is made more extreme by the CO molecule and this bending is the mechanism that yields such high resolution in NC-AFM images. The model considers this and it has shown that features resembling bonds can be imaged, using the Lennard-Jones potential and atomic coordinates without considering the electron orbitals.

Each atom can be viewed as the source of its own Van der Waals force field, because the electrons are concentrated there, which contributes to the overall field. One could consider the force field to be many force iso-surfaces summed together. Because the positions directly above the atoms are closest to them, there will be a peak in the iso-surface above each atom. In a molecule, the bonds between atoms often represent the shortest possible path between two atoms. In-between the atoms the tip will measure a contribution from both, leading to a ridge in the force iso-surfaces. This ridge acts as a watershed, discriminating between situations where a tip will relax down one side or the other and it is only at the very top of the ridge that the tip will not be deflected to experience lower forces. This effect is shown in Figure 2.7 along with its result: a sharp increase in contrast at the watershed in NC-AFM images which appears as if the bond has been measured. However, in this example, there is no bond between the two sulfur atoms causing the watershed!

This indicates that one cannot claim to have observed bonding without additional evidence. This is a good example of how it is necessary to understand the mechanism behind the creation of SPM images in order to ensure your interpretation is valid. The Probe Particle Model has become an invaluable tool that is used in many publications [44, 45].

2.7 The challenges of ambient measurement

The beautiful images of STM and NC-AFM derive, in part, from the isolation of the experiment. By choosing to operate in an ultra high vacuum (UHV) environment, the experiment can avoid the presence of contaminants, the formation of water between the tip and surface and extrinsic damping on mechanical oscillators [25, 46].

Contaminants can be picked up and dropped by an SPM tip: changing the resonant frequency, acting as a transducer for force and insulating the tip apex from electrical current. All of these effects will change the signal measured by any SPM mode leading to sudden jumps and drops in the perceived height or conductivity of the surface. In the case of STM, this can be particularly troublesome as, if the electrical signal is reduced too far, the tip will move too close to the surface and 'crash'. Removing contaminants creates a more stable system capable of generating very repeatable images.

If a sufficient quantity of water is present in the atmosphere, placing a tip close to the surface creates a small gap that is susceptible to capillary effects [46]. A small amount of water condenses between the tip and surface leading to a change in the medium of the oscillation. This sudden change obscures the tip-surface interaction you are trying to probe, reducing the resolution in z and distorting $F(z)$ spectra. This sudden change of medium is discontinuous and only affects the base of the oscillation, but entirely immersing the experiment in a consistent fluid medium may not suit your experiment.

The sensitivity of a resonating system depends upon its Q-factor [47]. This factor describes how energy provided to the system is distributed by the resonator. A high Q-factor means that more of the energy reinforces the oscillation at resonance and less energy is needed to maintain an oscillation. In a mechanical resonator in an atmosphere, air resistance increases proportionately with the velocity until the onset of turbulence, but in the opposite direction [48]. Because the air resistance is always acting (π radians) out of phase with the motion of the resonator, the force is always

acting to oppose that motion and dissipates energy into the atmosphere. It is clear then, that by carrying out your experiment in a UHV environment you increase your Q-factor.

A higher Q-factor means that the resonance peak is sharper, giving a higher resolution in frequency and, as a result, better discrimination between frequency shifts. NC-AFM gains better resolution in z from its operation in a UHV environment, but the Q-factor is further increased by operation at a low temperature.

Decreasing the temperature of an SPM system increases the sensitivity of 'qPlus' sensors and yields many other advantages [47]. As the temperature of a system decreases, the random motion of its constituents also decreases. If the atoms the tip interacts with, and the tip itself, have a smaller range of possible positions then the range of possible tip-sample distances is reduced so the force experienced by the tip is more consistent. Again, this improves the z-resolution of the SPM device.

Further to this, if one is studying molecules on a surface, a commonly observed system in SPM, the molecules have less energy. As a result of this the molecules are less likely to move around the surface [49]. Imaging a moving object one pixel at a time is just as impossible as you might think! Additionally, the surface itself can move due to thermal drift. If the surface or SPM piezo is not in thermal equilibrium, they will expand at different rates. Though the change in the size of features is often minimal, across a large object the collective expansion and contraction of bonds leads to the surface moving relative to the tip. By isolating the SPM system from external temperature changes and taking steps to define the temperature of the tip and sample the rate of thermal drift can be reduced significantly.

Such isolated systems grant researchers the ability to understand fundamental science without the intervention of the messy world outside the UHV chamber, but these ideal SPM conditions do not reflect the environment in which many applications and processes operate. Many materials will be used in an ambient environment or a host of liquid environments. It is vital that SPM can be carried out in these environments as well in order to understand how we can expect materials to

change when in use. In addition, broadening the ways in which data can be collected on phenomena opens the door for more researchers to contribute to a topic, widening the perspectives with which a system is viewed. For these reasons, it is important that the limits of resolution in an ambient environment are explored and probed to see if improvements can be made.

2.8 Optical spectroscopy

Microscopy provides users with an invaluable method of observing features on very small length scales. This is ideal for identifying individual features, but it also means that by its very nature, only a small portion of the sample is observed. The optical spectroscopy techniques discussed here inform the user about the properties of a material within a laser spot, which is much larger than many SPM images with atomic resolution. Such techniques are carried out by shining a laser on the sample, providing photons with a single energy. One can then study if any photons are measured at different energies due to losses in energy between an electron absorbing the photon and an electron emitting a new photon.

These energy losses originate from two processes. In Raman spectroscopy, the carriers interact with a vibration in the crystal which can be modelled well as a quasi-particle called a phonon. Diagrams of the process are shown in Figure 2.8.

During the scattering of a photon from an electron in the crystal, the energy of an electron is either increased (Stokes) or decreased (Antistokes) via an interaction with a phonon [52]. The energy of a photon E can be expressed in terms of plank's constant h, the speed of light c and wavenumber ν which is the inverse of the wavelength. Raman scattering leads to a change in the energy of the photon ΔE which is measured as a change in ν called the Raman shift $\Delta\nu$.

$$\Delta E = hc\Delta\nu \tag{2.4}$$

The units of $\Delta\nu$ are [cm^{-1}] because ν is the inverse of the wavelength. Because

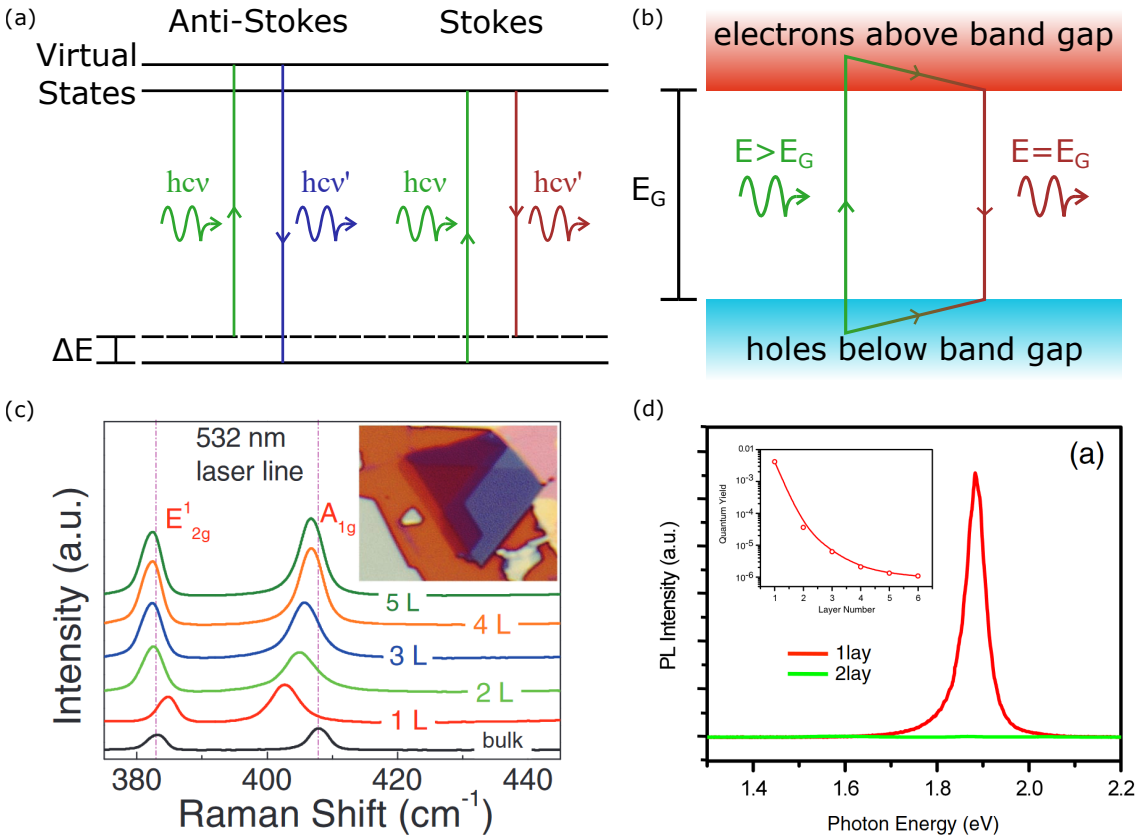

Figure 2.8: Two diagrams depicting the light-matter interactions behind *(a)* Raman and *(b)* photoluminescence spectroscopy. In Raman scattering the crystal gains or loses vibrational energy ΔE during the interaction, varying the energy of the scattered photon. In photoluminescense spectroscopy in semi-conductors the reduction in the energy of electrons leads to electrons above the band gap and empty states ('holes') just below the gap which biases the emission energy of photons to equal that of the gap. The *(c)* Raman and *(d)* PL signals of MoS_2 reported by Li et al. (Reprinted figure with permission from Li H. et al. [50] Copyright Wiley-VCH GmbH. Reproduced with permission.) and Mak et al. (Reprinted figure with permission from Mak K. F. [51] et al. Copyright 2010 by the American Physical Society.) respectively.

phonons in a material are oscillations in the bonds and there are a number of specific oscillations that can be excited in a given crystal, the Raman spectrum of a particular crystal shows distinctive peaks. Even in the case of similar crystals, the mass of the atoms differs, leading to variations in the spectrum.

The other optical spectroscopy technique used in this thesis is photoluminescence

spectroscopy (PL). The technique is carried out in the same way, but the peaks are formed due to a different light-matter interaction. When a material is excited by a photon, promoting an electron to a higher energy state, the electron is able to lose energy through a number of mechanisms. When the electrons encounter a region without states they can no longer lose energy via interactions that only lead to small losses of energy. This increases the likelihood of finding electrons above this gap and then that they will emit a photon in order to lose enough energy to traverse the gap in a single interaction. The exact amount of energy required to travel across this gap can then be studied by measuring the energy of the photons emitted from the material.

In this work we will study a class of materials called semiconductors which have such a situation with states either side of a band gap. In the following chapter the theory behind electrons in crystals will be explained and it will become clear how Raman and PL can reveal valuable information about a group of two dimensional crystals called transition metal dichalcogenides.

Chapter 3

Materials

A microscope is useless without a subject to study and a reason to do so. This chapter will discuss the systems that are the subject of this thesis: two-dimensional materials and the molecules adsorbed on surfaces. For each material, I will first outline what they are and which properties make this material worthy of study. In order to appreciate how the system comes to have those properties it is crucial to discuss the physics that describes their behaviour. Then, I will discuss how these systems are fabricated and characterised in current research in order to study these properties and prepare for their exploitation in emerging technologies.

3.1 Two dimensional materials

The idea of a material with less than 3 dimensions originates from a foundational concept in quantum mechanics. A particle with no external conditions applied to it is said to be in 'free space'. Imagine that two, infinitely large parallel boundaries that reflected the particle could be used to constrain its movement in a particular dimension. If these boundaries are brought close enough together ($\sim h/p$ where p is the momentum) the particle is no longer thought of as having a particular position in that dimension. Instead, the wavefunction of the particle becomes a standing wave between the boundaries and the particle may occupy the states created by the various

harmonics of that system. The motion in the two perpendicular directions remains unaffected. As a result, we have the idea of restricting a particle in a dimension until it ceases to have a meaningful position in that dimension and effectively 'loses' a dimension. When a material is said to have two, one or even zero dimensions this refers to the confinement of electrons in that material such that motion in some or all of the directions becomes meaningless.

Two-dimensional systems were originally fabricated as a part of a bulk material. On the interface between two bulk semiconductors, one can trap electrons near the interface. However, two-dimensional materials were a theoretical construction before any two-dimensional materials were fabricated. By developing a theoretical framework for the physics of a two-dimensional material, it can be used as a building block for considering the physics of layered materials. Some crystals, such as graphite, are composed of repeating 2D layers that are only bound to each other by Van der Waals forces. By considering a single layer (monolayer graphene) theorists were able to construct theoretical models of carbon nanotubes [53] and graphite [54] for instance.

In 2004 the first report of 2D crystals was made, showing the creation of graphene monolayers from the exfoliation of graphite and their subsequent characterisation [55]. Mechanical exfoliation is a process in which a form of tape is used to tear layered materials apart until a single monolayer remains.

The physics of 2D crystals could then be explored, including exotic quantum transport properties for which Andre Geim and Konstantin Novoselov won The Nobel Prize. The intriguing possibilities of measuring unique or improved properties due to a two-dimensional geometry resulted in a great deal of interest from researchers in fundamental and applied fields alike. This led to the isolation of many other 2D materials and the discovery of alternative synthesis routes such as Chemical Vapour Deposition (CVD) and Molecular Beam Epitaxy (MBE).

3.1.1 Bravais lattices

In physics, crystals are made up of a repeating pattern of atoms. Either an individual atom or a group of atoms called a 'basis' are repeated in space at points in a Bravais lattice $\mathbf{r}$. A lattice is a mathematical device defined as the points in space found by summing together an integer number ($u_1, u_2 \in \mathbb{Z}$)of the lattice vectors ($\mathbf{a}_1, \mathbf{a}_2$) [56]. In three dimensions we require three vectors, but for two dimensions we can define a lattice as points satisfying Equation 3.1.

$$\mathbf{r} = u_1\mathbf{a}_1 + u_2\mathbf{a}_2 \tag{3.1}$$

Lattices are classified on the basis of their symmetries, such as rotational symmetry. With the simple constraints of being a lattice in two dimensions, there are actually relatively few classifications of Bravais lattices in two dimensions, so much so that they are all shown in Figure 3.1. The remaining lattices with very low symmetry come under the catch-all term 'oblique lattice'. The periodic nature of crystals enables a complex system to be modelled as a small, understandable repeating cell.

3.1.2 The density of states

In Quantum Mechanics waves are often described in terms of the wavenumber $q = \frac{2\pi}{\lambda}$ where λ is the wavelength. In this thesis, I will use q to refer to the wavenumber rather than the standard k in order to avoid confusion with the Hooke's constant. A wave with a position x and amplitude A in a single dimension can be described by the wavefunction ψ in Equation 3.2. Critically, this wavefunction is periodic as $1 = e^0 = e^{2\pi j}$ where $j \in \mathbb{Z}$.

$$\psi = Ae^{iqx} \tag{3.2}$$

Another result of the periodicity is that the electrons act as if confined within a periodic potential of size L [57]. To satisfy these conditions a wave would need to have the same value if x were to change by L. By equating the values of ψ in

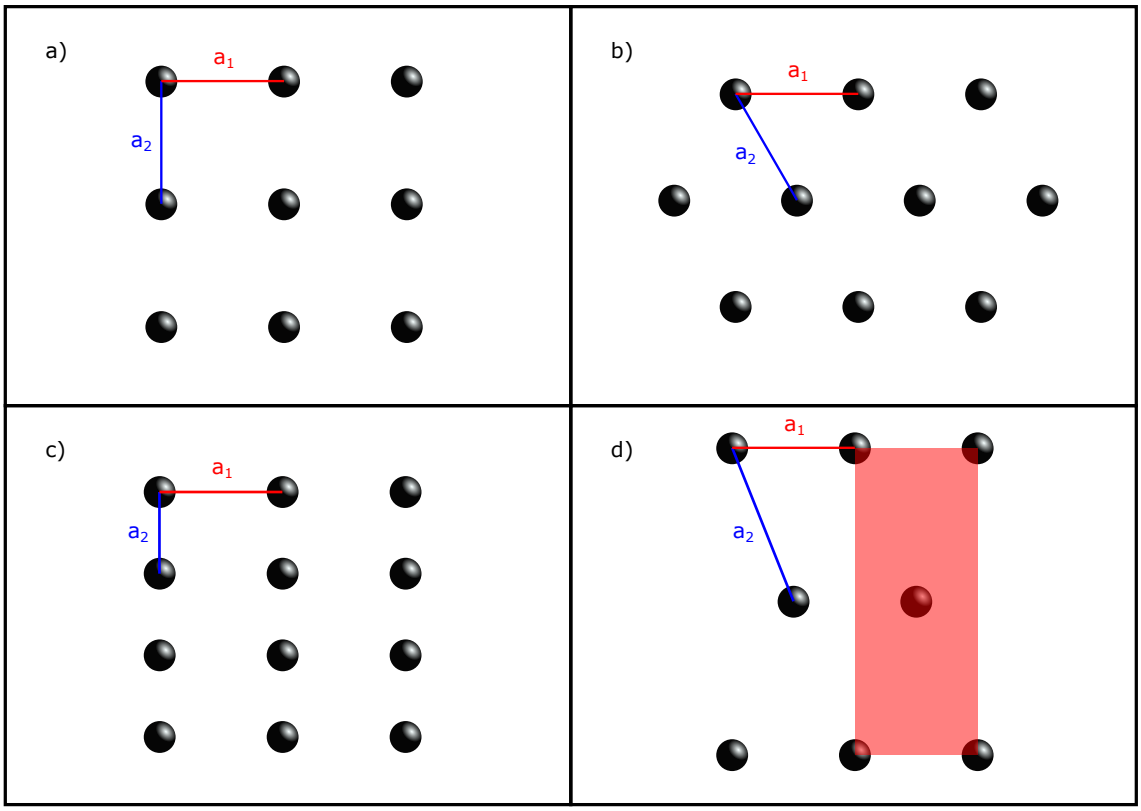

Figure 3.1: All 2D Bravais lattices are oblique lattices, but there are four specific cases. The 'square' lattice *(a)* is the simplest case: the lattice vectors are equal ($a_1 = a_2$) and separated by 90°. If the vectors remain equal in length, but they are instead 60° degrees apart, one has a 'triangular' or 'hexagonal' lattice *(b)*. If the vectors are different lengths, but the angle remains 90° on the other hand, we have a 'rectangular' lattice *(c)*. Finally, if the lengths of the vectors are different and the angle between them isn't 90° there is a case where interesting symmetries arise. If the component of one of the vectors in the direction of the other is half the length of that vector ($\hat{\mathbf{a}}_1 \cdot \mathbf{a}_2 = a_1/2$) then a repeating rectangle is formed with a site in the middle *(d)*, presenting similar symmetries to the rectangular lattice. This lattice is called the 'centred rectangular lattice'

Equation 3.2 at $x = \pm L/2$ we can see that $q = \frac{2\pi}{L}j$. This means that electrons can only have specific values of momentum and in order to occupy these states, the electron must have a large enough wavenumber.

There is a concept in physics called a free electron gas where electrons have energies defined solely by their kinetic energy E, which depends on q and the mass of the electron m_e. The kinetic energy of a particle can be described in terms of q by Equation 3.3.

$$E(q) = \frac{\hbar^2 q^2}{2m_e} \tag{3.3}$$

In a single dimension an electron may move left or right, described by negative and positive q respectively. As E increases, so does q and more states become accessible to the electron. The states are equidistant in q and there are 2 directions, so 2 states are added every time q increases by $\frac{2\pi}{L}$. As a result, the number of available states in a distance L in terms of the wavenumber can be found by integrating $N(q) = \int_0^q 2\frac{1}{2\pi}dq$. The expression inside the integral is the density of states $g(q) = dN/dq$. As the energy of the electrons is much more useful as an experimental variable, we can use Equation 3.3 to express the density of states in terms of energy for an electron gas. This is shown in Equation 3.4..

$$g(E) = \frac{1}{\pi\hbar}\sqrt{\frac{m_e}{2}}E^{-1/2} \tag{3.4}$$

A slight complication arises from sources of degeneracy such as spin. It is common for two electrons with opposite spins to occupy an otherwise identical state. In such a case the density of states can simply be scaled to account for the degeneracy.

In two dimensions the material can travel in two dimensions which results in two orthogonal wavenumbers q_x and q_y which can be described by the wavevector $\mathbf{q}$ with magnitude q. If the states were plotted on two axes representing q_x and q_y they would form a square lattice. An electron with a particular kinetic energy can fill within the boundary $q = \sqrt{q_x^2 + q_y^2}$; a circle. As a result, increasing q adds new

states in a more complex way. In two dimensions the density of states is constant.

In reality, because two-dimensional systems confine electrons in the third, out of plane, direction the electron can enter higher harmonic states in that direction, as discussed. If the electron can be in the fundamental wave or first harmonic there are twice as many ways to arrange the electrons. As a result, a fuller description of the system is a series of steps.

3.1.3 Band structure

In real crystals, kinetic energy is not the only consideration for electrons. Electrons near the chemical potential are in states relating to the chemical bonding between atoms. The impact of binding so many atoms together is that, instead of the bonding and anti-bonding states one would expect when two atoms bond, there are 'bands' of continuous states; each defined by a dispersion relationship $E(\mathbf{q})$.

The resulting 'band structure' consists of surfaces in $E(\mathbf{q})$ where the electrons can exist and some regions of E which no bands enter called 'band gaps'. When the chemical potential, the minimum energy required to add an electron to the system, lies within such a gap the bands below the gap are occupied and those above are not. Electrons may be excited from the band below this gap, known as the valence band, to the band above, known as the conduction band. After excitation, the electrons rapidly decrease their energy within this band by changing $\mathbf{q}$ until they are at a minimum position. A similar process occurs in the valence band where electrons in higher energies are able to move into the empty state, resulting in an absence of an electron called a 'hole' moving to the highest energy in the valence band.

If the electron and hole have the same value of q, the electron can decay back into the valence band by emitting a photon. If this is not the case, another particle other than the electron and the hole must take part, decreasing the probability of the interaction and making it more favourable for the recombination of the electron and the hole to occur through other paths such as defects where a photon is not emitted. The former case is called a 'direct' band gap and the latter is an 'indirect'

band gap and signifies that this material will not be a good candidate for devices involving the emission of light.

Electrons in the conduction band and holes in the valence band are termed 'carriers'. If a band is full there can be no movement of charge because the carriers are moving in all directions resulting in no net motion, but when carriers are created they are able to transport charge through the crystal. Thus it is only the carriers that need to be considered in order to discuss much of the properties of a crystal.

The periodicity of the lattice also results in the dispersion relationship $E(q)$ becoming periodic too. As a result, the momentum space can be folded into a manageable periodic region called the Brillouin zone [56]. The momentum of an electron is then replaced by a 'crystal momentum' $\mathbf{p} = \hbar\mathbf{q}$ that lies within the Brillouin zone as these are only momentum values required to describe the energy of all of the electrons in a crystal. In a two-dimensional crystal, the region is a two-dimensional shape such as a hexagon if the dispersion relationship is plotted on axes of q_x and q_y.

3.1.4 Effective mass

Frequently, the top of the valence band and the bottom of the conduction band have near-parabolic dispersion relationships, mirroring that of the free electron gas. When this is the case, we can act as if the electrons in the material are 'free' by scaling the kinetic energy up or down with a constant. As the kinetic energy already has the constant $\frac{1}{2m_e}$ at the front we can simply exchange the mass for an effective mass $\tilde{m}_e$ that approximates the dispersion relationship near the band gap. Because the vast majority of carriers reside in this region, this is frequently a good approximation.

One might be wondering where the effects of confinement become relevant. Essentially, these bands act like many two-dimensional free electron gasses. Quantum dots, systems that are confined in all three dimensions, are ideal examples of confinement in action. By changing the size of a small piece of semiconducting material, the band gap can be changed. By tuning the radius of the dot we can

change the light that the dot absorbs, changing its colour [58].

3.1.5 Transition metal dichalcogenides

Transition Metal Dichalcogenides (TMDs) stand out as 2D materials with many potential applications due to their favourable properties. There are multiple ways for a TMD to arrange itself, called 'phases', but many common TMDs find the semiconducting '2H' phase to be the most energetically favourable. This means that they often adopt this phase in naturally occurring layered materials (bulk). In the monolayer case alone these TMDs have a direct band gap [59], making them candidates for efficient optical devices with a bright photoluminescence response (explored in Section 2.8). There is great interest in TMDs because of their potential applications. They have been considered for applications as field effect transistors, as catalysts and for optical applications. The heavy impact of defects on the properties of TMDs also offers avenues for tuning TMDs to have the desired properties for an application, as will be explored in Section 3.2.

The basis of a TMD consists of three atoms; a transition metal and two chalcogen atoms [60, 61]. The transition metals are a variety of metallic elements lying in the centre of the periodic table from groups 3 to 12 and the chalcogens are sulfur, selenium and telerium. If z lies normal to the surface of the TMD, the chalcogen atoms lie at identical x-y positions whereas the transition metal is offset. When this basis is repeated in a triangular lattice, the atoms form a honeycomb-like pattern when observed normal to the plane (Figure 3.2). The chalcogen atoms in the basis are separated in z such that when the basis is repeated the crystal consists of three layers: a transition metal core with chalcogen atoms above and below. For this reason, the monolayer of a TMD has historically been called a tri-layer in some publications though a consensus has been reached over time that brings the terminology in discussions of TMDs in line with other layered materials.

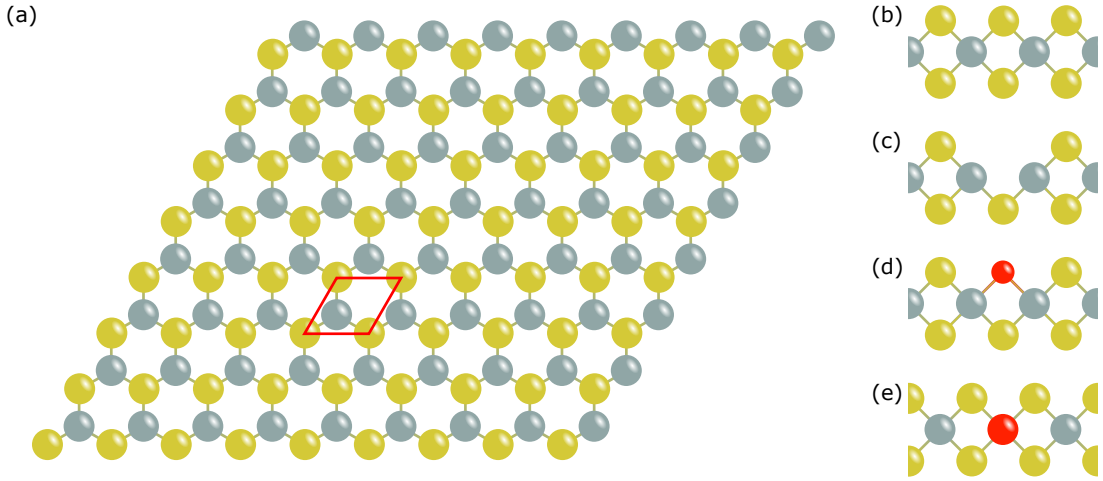

Figure 3.2: Cartoons of the TMD lattice from the out of plane *(a)* direction and a cross-section of a monolayer *(b)*. The chalcogen atoms are in yellow and the transition metal atoms in grey. The common defects in TMDs are also shown with atoms of non-native species displayed in red: a chalcogen vacancy *(c)*, chalcogen substitution *(d)* and a transition metal substitution *(e)*.

3.1.5.1 Defects

Defects are deviations from the theoretical lattice discussed in the previous section [62]. These changes can involve missing atoms (vacancies), the wrong element (substitutions) and atoms simply in the wrong place (dislocations). The common defects in TMDs are shown in Figure 3.2c-e.

When discussing defects it is important to consider two categories: formative defects, defined here as those which were created during the formation of the crystal, and experiential defects which have been created by the conditions a crystal has experienced since that time.

During growth, the crystal formed because it was the most energetically favourable scenario for the ensemble of atoms present (assuming a quasi-static process). This means that the formative defects are likely formed from the elements in the ideal lattice (native); though there will, of course, be some degree of impurity. When the formation of a crystal begins, it will start at several nucleation points and

then spread out. When two of these crystals merge a series of compromises will have to be made along their interface. This often materialises as a line of dislocations called a grain boundary. In addition to this, some errors will have been made resulting in vacancies and substitutions of one native element for another, referred to as an 'antisite'. If similar elemental species were present there may be some degree of formative substitution for non-native elements.

Experiential defects are created after the formation of the crystal from sources such as exposure to air. If it is energetically favourable to replace atoms in the lattice with available elements, the crystal will gradually incorporate substitutions even, in some cases, changing so substantially that remaining atoms of the replaced element should be treated as defects in a new crystal [63].

The properties of materials can be changed on a macroscopic scale through their collective effects on bulk properties such as conductivity and quantum efficiency. It is often the collective effects that lead to their purposeful incorporation into materials. The semiconductor industry uses defects to 'dope' materials, tuning the size of their band gap, carrier concentration and the position of the chemical potential.

In a small localized region around the defect, stronger changes in the properties can be seen. A defect may add, remove, or shift electronic states, leading to the idea of a local density of states (LDOS). In the case of a crystal with well-defined magnetic properties, a spin that breaks the pattern leads to a local distortion in the magnetic field. Some elements may even introduce a local magnetic susceptibility in a material with very little response to a magnetic field.

These strong local changes can be observed by SPM modes that are sensitive to them. Monolayer 2D materials are particularly good candidates for SPM characterization because their defects are at the surface and, neglecting the substrate, must originate within the single layer so there is less ambiguity about their depth. TMDs are known to possess many formative defects compared to other 2D materials and yet retain some degree of air stability such that they can be observed in an ambient environment [62]. Point defects such as vacancies and

substitutions occur on a particular lattice site and, as a result, act as a good measure of 'true' atomic resolution. As was discussed in Section 2.5, probes with what is termed 'lattice resolution' cannot resolve individual atoms, and thus defects. The periodicity of the lattice can be imaged when the tip is interacting with multiple atoms, but this means that the defects cannot be observed.

Clearly, TMDs are materials with great potential due to their properties. Because these properties are strongly influenced by an abundance of defects, characterising them is vital; especially in an ambient environment that many TMD devices may be exposed to during fabrication or use. In Chapters 5 and 6 we will discuss how we successfully characterised TMDs with atomic resolution using cAFM.

3.1.5.2 Excitons

In TMDs, the band structure is made more complicated by excitons. Excitons are bound particles formed by coulomb interaction between an electron and a hole. The system bears a striking resemblance to the lone hydrogen atom with an electron of charge $-e$ orbiting a proton of charge $+e$. One clear difference is mass. Here the mass of the two particles is determined by their effective masses due to the band structure of the material.

By finding the second derivative of $E(\mathbf{q})$, as defined in Equation 3.3, with respect to $\mathbf{q}$ we can find the effective mass of each band. Using these masses we can calculate the energy levels of the exciton.

In most TMD samples the smallest gap is between two different points in the Brillouin zone and the carriers collect at those positions. In the monolayer case however, an exciton, the A exciton, reduces the gap in energy between the electrons and holes at the 'K' point converting the material from an indirect band-gap material to a direct band-gap material [51, 59].

The bandgap at the K point actually increases in the monolayer case, but the binding energy of excitons is much larger in two dimensions. The energy levels of a hydrogen atom are spherically symmetrical in three dimensions and this yields the

energy levels $E = \frac{R_E}{n^2}$ where $n \in \mathbb{Z}$ and R_E is defined in Equation 3.5.

$$R_E = \frac{\mu e^4}{2(4\pi\epsilon\hbar)} \tag{3.5}$$

The masses of the two carriers are combined into one 'reduced' mass μ and ϵ is the permittivity of the medium, which at is the permittivity of free space $\epsilon = \epsilon_0$ for hydrogen. The first consideration for excitons in TMDs is that they are in a two-dimensional system. As a result, the Schrödinger equation is solved in two dimensions so the binding energy is 4 times larger [64, 65]. Further to this, a monolayer is extremely anisotropic, leading to an anisotropic permittivity. The electrons in a solid screen charge because the coulomb interaction leads them to attempt to cancel the charge out. Monolayer TMDs have exceptionally low permittivities, meaning that the charge is badly screened and the carriers in the exciton experience each other more, resulting in a factor of 9 increase in the binding energy due to the change in permittivity alone. Collectively the factor of 4 and 9 result in a binding energy approximately 40 times greater [64]. The fact that the bands with extrema at K originate from in-plane states that are relatively unaffected by the presence of layers above and below has also been cited as a factor in the switch to a direct band gap in the monolayer [59, 66].

Excitons can form from more than one carrier. The exciton itself is neutral, but it is made of charged constituents facilitating interactions with even more carriers. An exciton with a third carrier is called a trion and it becomes negatively charged if the extra carrier is an electron (eeh) or positively charged if the extra carrier is a hole (ehh). There are also reports where features have been attributed to bi-excitons (eehh) consisting of four carriers. Interactions are more likely to occur if there are more carriers available to participate, so when an electrical field caused by defects or external sources attracts more carriers of a particular type the population of excitons that form is affected. In fact, as the trions are energetically favourable cryogenic studies have found that the population of trions remains relatively stable, whereas the population of neutral excitons depends heavily on the carriers present[67, 68].

Different forms of carriers have different binding energies, resulting in different bandgaps for the material. Because defects change the properties of a material locally it is reasonable to expect changes in the local population of excitons and the light emitted when the carriers recombine. In addition, carriers in defect states can form excitons, leading to bound excitons with lower energies [69]. By studying these bound excitons we can learn about the defects present in a TMD and a good way to do this is through optical spectroscopy.

3.1.5.3 Optical spectroscopy

The optical spectroscopy techniques discussed in Section 2.8 can be used to study TMDs. The Raman spectrum is particularly important for identifying different materials due to the unique spectrum that different crystals have. In particular, one can differentiate between monolayer and few-layer 2D materials. In the case of WSe_2 and MoS_2 two peaks are significantly closer together in the monolayer case for instance [50, 70].

Photoluminescence (PL) spectroscopy on the other hand, yields information about the bandgap of semiconductors. Because the holes rise to the top of the valence band and electrons relax to the bottom of the conduction band, the energy of the emitted photon is equal to the energy of the band gap. This means that the band gap of a semiconductor can be probed by measuring the energy of the returning photons.

In the case of TMDs the population of excitons are measured instead, because excitons in monolayer TMDs create states that are closer together than the bandgap if they are neglected. As a result when the carriers recombine, the photons observed in the PL signal are mostly the result of the annihilation of the electrons and holes paired together in excitons.

As discussed, TMDs have strong direct band gap PL signals in the monolayer case. Decay via the emission of a photon has a negligible impact on the momentum of the electron. As a result, a photon alone cannot enable an electron to decay across

an indirect band gap. Because the radiative decay does not need the involvement of an additional particle to remove momentum from the carriers it is much more efficient and more photons are released. This means that monolayer TMDs have a large increase in the signal of their PL spectra relative to even bilayers [51, 59, 61]. This sudden change makes it easier to identify monolayers. Examples of PL spectroscopy can be seen in Figures 2.8 and monoIdLit.

3.2 Review of transition metal dichalcogenides

In this section, the existing work to characterise and fabricate samples involving transition metal dichalcogenides (TMDs) will be outlined. This includes advances in the fabrication of TMD samples in isolation, as a part of heterostructures and after processes which create defects. The methods of characterising the samples and, in particular, their defects are an important consideration here alongside simulations which offer possible explanations for what is observed.

Due to the widespread interest in TMDs, their defects have been observed thoroughly under Scanning Tunnelling Microscopy (STM) [9, 71, 72, 73, 74, 75, 76, 77, 78]. The formation of defects is not an ordered process and monolayer TMDs have a strong optical response. Every sample contains a unique arrangement of defects and this can be probed optically as defects modify the PL response, so it should be possible to use TMDs as identifying tags. [79, 80, 81].

If changes in the density of defects occur on length scales appreciable for optical techniques, 100s of nm, there is the possibility to map stark changes to create a readable, unique tag. Such tags have applications in product verification or as part of a multi-factor authentication system [14].

In order to progress the use of few-layer TMDs from laboratory samples to materials that begin to have an impact on people's lives it is key to understand them in an ambient environment. Once exposed to air TMDs can react chemically and this should change their properties [82]. Synthetic samples have been shown to

be particularly susceptible in studies with X-ray photoelectron spectroscopy (XPS), PL spectroscopy and Auger electron spectroscopy. In order to introduce TMDs into an ambient environment there are essentially two approaches: one can study and understand the decay, or attempt to encapsulate the sample. Encapsulation by hBN has been shown to reduce changes in the Raman and PL spectra and to maintain the electronic properties, implying that the sample is protected from oxidation and other forms of damage [83]. However, some applications for TMDs such as catalysis will require the surface to be exposed and encapsulation adds another layer of complexity to making the technique generally available.

In order to explore the possibilities of applying TMDs as secure identification tags and to lay the groundwork for studies on the effects of air exposure on TMDs it is important to be able to acquire meaningful images of defects in an ambient environment. As discussed above, STM has already shown that it offers invaluable insights, but the ambient environment can provide problems for STM. In 'constant current' mode, as discussed in Section 2.3, an STM changes the height of the tip using a feedback loop to maintain a constant current. As the ambient environment is less pristine and mechanically exfoliated samples are typically exposed to polymers which can be picked up on the STM tip, studies of TMDs with STM have tended to be restricted to an ultra high vacuum environment.

Recently there have been examples of atomic resolution using higher eigenmodes of cantilever oscillation by *Severin et al.* [84] and cAFM on TMD samples by *Sumaiya et al.* [24], *Nowakowski et al.* [85] and in this work which show atomic resolution in ambient conditions. In Chapter 5 I will present my research into the defects of TMDs with conductive atomic force microscopy, but here I will outline existing observations with scanning probe microscopy (SPM).

3.2.1 Fabrication of two dimensional materials

The balance between the ability to scale devices up to the dimensions necessary for large-scale industrial processes and the necessity of maintaining high-quality

samples has long acted as the core axis along which 2D fabrication techniques are positioned in literature. For instance, mechanical exfoliation is limited to the creation of flakes on the order of a few microns, but the high quality and largely monocrystalline nature of the flakes produced means that they are commonly used in fundamental research [86, 87, 88]. The strength of chemical vapour deposition (CVD) is its ability to create continuous macroscopic monolayer films, but these films are often polycrystalline [89]; resulting in grain boundaries that can significantly harm electronic transport properties [62]. Uses of 2D materials aiming at large-scale production tend to employ methods such as liquid phase exfoliation [90], intercalation [91] and 'Hummer's method' [92] to create dispersions from which 2D flakes can be cast onto substrates. However, isolating monolayers and preventing damage to flakes can be extremely difficult. In this section, I will explain the method used to create our 2D samples, mechanical exfoliation, in detail and briefly introduce chemical vapour deposition as it is necessary to understand the existing studies of defects in TMDs.

3.2.1.1 Mechanical exfoliation

The fundamental idea of mechanical exfoliation is to use adhesive tapes to pull apart the layers of a Van der Waals layer material [86, 87]. As the chemical bonds in these materials bind together atoms within a single 'monolayer', the forces between the layers that make up a bulk crystal are solely Van der Waals forces. This means that the layers can be trivially separated by sticking the top of the crystal to adhesive tape and then pulling the tape away. Repetitive exfoliation decreases the average layer number of the flakes but decreases the average size of flakes by tearing them apart.

Mechanical exfoliation can be carried out in particular atmospheres to reduce the exposure of samples to contaminants, but the polymer residues of the tapes are more difficult to exclude [87, 93].

3.2.1.2 Chemical vapour deposition

An alternative method, used to create exceptionally clean samples is chemical vapour deposition (CVD) [88]. In this method, precursor materials are vapourised into a carrier gas and then react in this state to form the desired substance on a growth substrate. Often it is necessary to choose a substrate upon which the material will grow well, necessitating a transfer onto a substrate which is better suited to the experiment. This is only one of many parameters which can affect CVD growth though and the correct tuning of the growth conditions can have a severe effect on the CVD film created.

The crystal often expands from initial nucleation points, creating what is known as a polycrystalline material, where multiple crystals become joined together. Nonetheless, the size of these polycrystalline films can become macroscopic, especially with the use of roll-to-roll growth methods [94, 95].

On a much smaller scale, the clean environment of CVD growth techniques enables the growth of two-dimensional samples that can be studied by STM with less concern for contamination as the sample needn't leave a vacuum environment [9, 24].

3.2.2 Deterministic transfer techniques

A number of techniques for the transfer of 2D materials onto a substrate have been devised. The basis of many of the techniques is to press the substrates together, allowing the flake to move to the more favourable substrate. In the PDMS dry transfer process, the sample is transferred from a PDMS stamp on a cantilever onto the desired substrate [87]. If transferring onto SiO_2 it is common to use a heater to aid the transfer by softening the PDMS stamp and to separate the layers quickly to pick materials up and slowly to place them [96]. PMMA is also commonly used as a stamp for the transfer and many techniques have been used to remove the polymer stamp after transfer. The simplest solution is to simply lift off the stamp rather than leave it behind, but there are examples of the stamp being purposefully left behind

and then removed through wet chemistry [87, 97]. The removal of PMMA with acetone has limited success though and more aggressive solutions which damage the material of interest are necessary in order to fully clean the substrate [98].

Alternative methods to dry transfer exist, for instance, flakes may be separated from their substrate using wet chemistry and then floated on the surface of water. By reducing the water level, the flakes may be brought down onto the new substrate [99]. However, this technique requires the substrate to be immersed in water and water in between the sample and substrate can cause folds as it complicates the placement of the flake. In addition to this, the water-based techniques involve exposing the sample to water which can be difficult to remove from the surface.

3.2.3 Spectra of transition metal dichalcogenides

A key part of the fabrication of monolayer samples is identification. By studying the changes in the photoluminescence (PL) and Raman spectra as layer number decreases, monolayers can be determined efficiently. The mechanisms of Raman and PL spectroscopy were described in Section 2.8.

Some spectra showing the layer-dependent changes in from the literature are shown in Figure 3.3. The E_{2g} and A^1_{2g} peaks of MoS_2 and WS_2 separate as layer number increases [50, 102, 100], which should enable the user to differentiate flakes of various thicknesses. The drop in the distance between these peaks from ~ 22 cm^{-1} to ~ 18 cm^{-1} between bilayer and monolayer MoS_2 is particularly large. However, the substrate can have a substantial effect on these values [102].

The PL spectrum of MoS_2 shows a less significant increase in intensity in the monolayer case, despite reports of extreme amplification on free-standing monolayers [51]. However, the disappearance of the indirect band gap peak 'I' at ~ 800 nm offers a clear difference between the monolayer and all other thicknesses [102].

The Raman spectrum of WSe_2 is peculiar amongst TMDs in that it has almost degenerate E^1_{2g} and A^1_{2g} peaks, leading to a single large peak. However, at 4 layers and below there is an additional peak that could be caused by uniaxial strain [70]. In

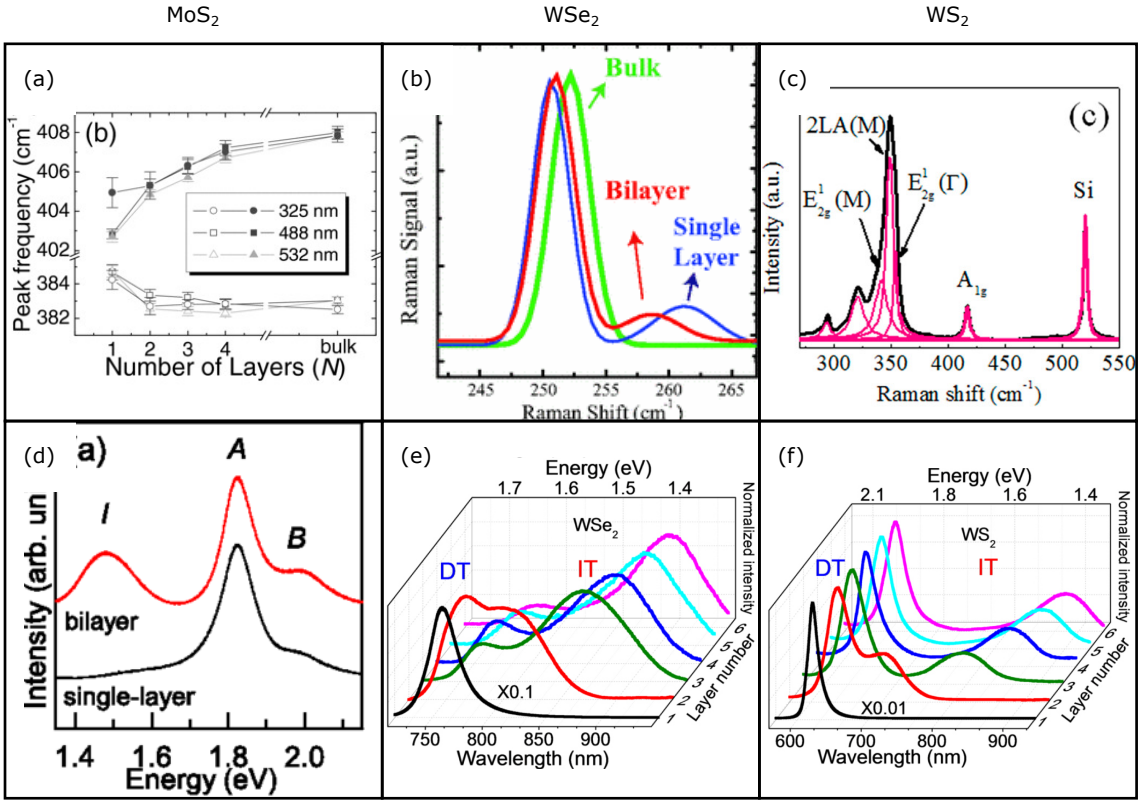

Figure 3.3: The E^1_{2g} and A_{1g} peaks in the spectra of MoS_2 separate as layer number increases *(a)* (Graph from Li H. et al. [50]. Copyright Wiley-VCH GmbH. Reproduced with permission.). This is also the case for the WS_2 [100], though as can be seen from the data reported by *Peimyoo et al. (c)*, the peaks are significantly more complex (Creative Commons License https://creativecommons.org/licenses/by/4.0/deed.en shown here is panel c of Figure 1 of [101]). In few-layer samples of WSe_2, an additional peak can be seen, such as in the spectra reported by (b) *Sahin et al.*, which moves beyond 260 cm^{-1} in the monolayer case alone (Reprinted with permission from Sahin H. et al. [70]. Copyright 2013 by the American Physical Society.). The PL spectra depicted here *(d-f)* all show the disappearance of the 'I' peak at longer wavelengths (lower energies) in the monolayer case alone and a large increase in intensity except MoS_2 which is reported to only increase by 40% by *Scheuschner et al.* on a SiO_2 substrate. Panel *d)*: Reprinted figure with permission from Scheuschner N. et al. [102]. Copyright 2014 by the American Physical Society. Panels *e-f)*: Li et al., [100]

the monolayer case alone, this peak lies above 260 cm^{-1}, presenting a clear indicator for identifying monolayers.

The PL spectrum of both W containing TMDs is over an order of magnitude brighter than the multilayer flakes meaning that it is often exceptionally clear from the magnitude of the PL signal which flakes are monolayers [100, 103, 101].

3.2.4 Observation of defects in transition metal dichalcogenides

MoS_2, WSe_2 and WS_2 have defects which have been very commonly studied with SPM [9, 22, 24, 72, 73, 74, 75, 76, 77, 78, 85, 104, 105, 106, 107, 108, 109, 110, 111, 112]. WSe_2 and WS_2 in particular are interesting subjects of study for optical applications because of the bright photoluminescence signal discussed above.

In order to discuss them it is important to define some terminology. Defects which mostly influence a specific lattice site will be referred to as 'localised' and the term 'diffuse' will be used for those which extend over a wider radius. In constant current scanning tunnelling microscopy (STM) it is common to discuss 'bright' and 'dark' defects corresponding to protrusions and depressions which are traced by the tip. Here I will refer to the 'bright' defects as 'augmenting' as they correspond to an increase in the current due to an increase in the local density of states between the tip and the chemical potential (See Section 3.1.2). The opposite situation, dark features, will be referred to as 'depleting'.

Observations by Barja *et al.* using NC-AFM and STM have made a strong argument that the most common defects in TMD samples, even if they are CVD samples that have never been exposed to air, are oxygen substitutions [9]. The assignment was made on the basis of STS measurements and spatial maps of $\frac{dI}{dV}$ on and around defects in $MoSe_2$ carried out at cryogenic temperatures and UHV conditions. Barja *et al.* also show that whether or not an oxygen substitution is imaged as an augmenting or depleting defect is determined by whether the defective atom lies on the top or bottom sub-layer of chalcogens in a TMD monolayer.

The defects observed extend slightly onto neighbouring cells, but are very nearly localised.

The spectra and images are in agreement with simulations of the local density of states around oxygen substitutions and I am not aware of any conflicting evidence. One can compare the most common defects across a variety of measurements and techniques. It is not uncommon for these defects to be attributed to chalcogen vacancies in STM, STEM and cAFM images on the basis that they are the most common defects and the low formation energy of vacancies, but no further evidence is cited [24, 72, 85, 104]. In STEM images, light elements are difficult to observe, especially if they lie above other larger elements, due to their minimal contrast, so there should be little difference between a vacancy and an oxygen substitution [9]. As a result, the defects in these papers assigned to vacancies are likely oxygen substitutions, which is how they are assigned elsewhere [9, 77, 110, 113]. In the STM and cAFM papers cited here the defects are either localised or approximately so.

In the work of Zhang *et al.* the most common defects are attributed to transition metal vacancies because they observe the defect lying between the chalcogen atoms, but this is not a common opinion nor a commonly reported observation of defects in TMDs [114].

This standpoint, that the most common defects are oxygen substitutions, is supported by theoretical work which indicates that not only is it energetically favourable for oxygen to form oxygen substitutions in a TMD, vacancies increase the probability of the adsorption and dissociation of oxygen nearby [108, 109]. As a result, it seems that if vacancies were to form, any exposure to an ambient environment would quickly convert them to oxygen substitutions.

In the work of Rosenberger *et al.* [22], the defects observed all appear as augmenting defects in cAFM images, but in the atomic resolution images taken by Sumaiya *et al.* the localised defects are all depleting. This could be due to augmentation around the site of a depleting defect that has been observed in

experiments and in simulations of the local density of states around defects in TMDs [9, 72, 75, 78, 115]. In cAFM which does not achieve atomic resolution, it is possible that the atoms surrounding the defective site as a whole are augmenting, even if the site itself is not.

Diffuse defects are frequently attributed to transition metal substitutions in studies using cAFM [24, 104]. Observations on TMDs by *Yankowitz et al.* measure a much lower density of diffuse defects than oxygen substitutions [74].

Defects have been observed with a similar appearance in STM images and attributed to charged defects [111]. A characteristic feature of these defects is their band bending. Band bending raises or lowers both the conduction band edge and the valence band edge at the same time rather than widening or thinning the band gap. This is because a coulomb force is experienced by the electrons in both bands and modifies them in the same way. If a diffuse defect were to be a charged defect one would expect to see asymmetrical behaviour with respect to the bias voltage in cAFM and STM.

3.2.5 Stability in air

Chalcogens with higher atomic numbers suffer a reduction in air stability [108, 116, 117]. Simulations of the formation energies of defects in TMDs offer insight into how probable defects are to form in each material. The formation energies of chalcogen vacancies in diselenide TMDs are less than in their disulfide counterparts, but this is not the entire picture. TMDs formed with tungsten have higher formation energies for chalcogen vacancies than those formed with molybdenum [108]. This results in a similar probability of chalcogen vacancies forming in MoS_2 than in WSe_2 and one would assume that there are similar densities of chalcogen defects in the two crystals as a result. However, there is an increased probability of molecular oxygen adsorption on WSe_2, which may mean that the presence of adsorbed oxygen leads to an increased number of defects by directly substituting chalcogens, rather than filling vacancies. In fact, if vacancies were the dominant form of defects and the

sample was exposed to oxygen, simulations show that molecular oxygen adsorption and dissociation on the surface are energetically favourable and that in the presence of a chalcogen vacancy the process is more likely [108, 109, 118]. Once the oxygen is adsorbed onto the surface, oxygen substitutions have a lower formation energy than chalcogen vacancies, so we could expect the oxygen to then fill the vacancy, forming an oxygen substitution [118, 119].

3.2.6 Cryogenic photoluminescence studies of WSe_2

Defects in WSe_2 have been studied with STM and cryogenic photoluminescence on HOPG by *Zhang et al.* and it was in this study that they found the dominant defect to be Tungsten vacancies [114]. Another group, using their method of CVD sample preparation found the same result in their STM images of WSe_2 on HOPG [76]. However, this view stands in contrast with other works so it is possible that this is a quirk of the particular fabrication method.

Nonetheless, *Zhang et al.* set out to identify the origin of defect-bound excitons in WSe_2. They discuss that because the bands at the conduction band edge are split into two based on the spin of the electrons, the lowest energy exciton is 'dark' because it cannot recombine radiatively. However, a small amount of thermal energy allows the slightly higher energy 'bright' exciton that has radiative emission to be occupied, leading to emission at room temperature. However, reducing the thermal energy of the system (cooling it down) can reduce the occupancy of the bright exciton, reducing the PL emission from the neutral exciton peak. This viewpoint has been found to agree with results in other groups [80, 120].

The measurement of polarised PL spectra on WSe_2 grown by the same method on a sapphire substrate was much brighter and showed that the spin polarisation is much weaker on the defect-bound excitons than the free excitons, meaning that they should be free of the dark exciton condition that makes the free exciton peak weaker at lower temperatures. In addition, they saw that the WSe_2 grown on an oxidised Si wafer had a signal five orders of magnitude stronger than on HOPG.

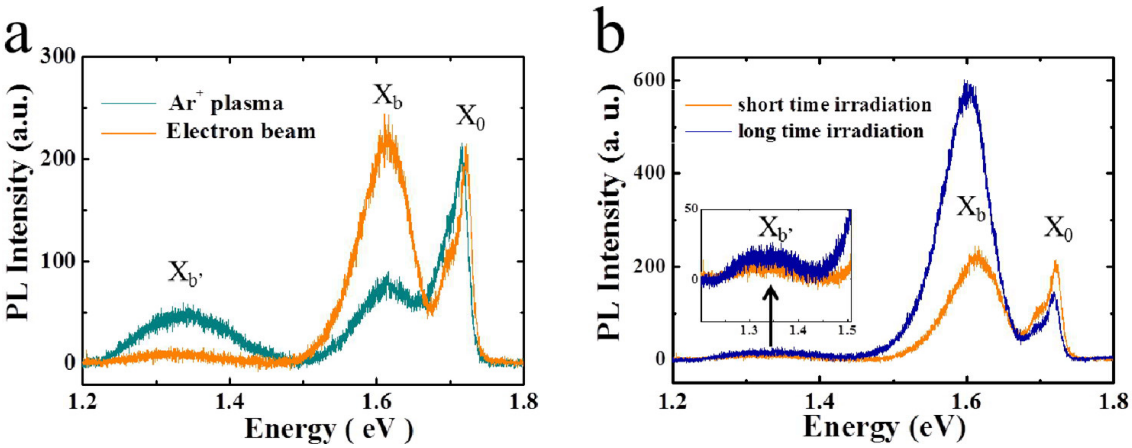

Figure 3.4: *a)*: The PL spectrum of WSe_2 consists of a free exciton X_0 peak and a trion peak at slightly lower energies. Electron beam exposure mostly added peak X_b to the spectrum of WSe_2, but exposure to argon plasma also added $X_{b'}$. *b)*: A longer exposure to electron beam irradiation is necessary in order to observe $X_{b'}$. Reprinted with permission from Wu et al. [120]. Copyright 2017 American Chemical Society.

A more detailed view is given by a group from Nanjing University which published two illuminating papers on the effects of defects on the PL signal of WSe_2 on SiO_2 measured at 83 K. In the first paper, an electron beam was used to generate defects, resulting in a relatively shallow defect peak at ~ 1.62 eV that was absent in their pristine samples [80]. Before irradiation, there were two peaks at ~ 1.71 and ~ 1.73 eV. The peak at higher energies was attributed to the free exciton peak X whereas the peak at a slightly lower energy was attributed to free trions. Irradiating their samples with Ar^+ plasma instead resulted in two defective peaks. One lies at ~ 1.60 eV, similar to their previous work with an electron beam, but another peak was also found at much lower energies around ~ 1.35 eV [120]. The deeper peak was then observed after irradiating samples with an electron beam for a long time. The shallow peak is labelled X_b and the deep peak is labelled $X_{b'}$. These peaks are shown in Figure 3.4

Both X_b and $X_{b'}$ saturate at low powers compared to the linear power dependence of the free exciton peak. The two localised peaks indicate that there are two ways that defects can be localised and that the deeper excitons require a different change

to occur. The higher binding energy of $X_{b'}$ may be due to a state which is much further into the bandgap, potentially caused by a different type of defect. X_b has been reported to be caused by mid-gap states $\sim$ 0.1 - 0.3 eV above the valence band maximum. This corresponds well with the position of peaks in the density of states resulting from defects on the chalcogen sites. Oxygen substitutions (O_{Se}) have been predicted to produce peaks in the density of states close to the valence band minimum and this has been observed in low-temperature scanning tunnelling spectroscopy measurements with energies in the correct range for $MoSe_2$ [9].

At helium, rather than nitrogen, temperatures similar features are observed. The free exciton lies between 1.7 and 1.75 eV [121, 114].

3.3 Molecules on surfaces

The other system studied in this thesis is molecules adsorbed on a metallic surface; specifically Zn tetraphenyl-porphyrin (ZnTPP) on Au (111). In this section I will introduce some key concepts that will assist the reader in understanding the discussion of ZnTPP that follows. Then I will introduce the ways in which molecules adsorb on metallic surfaces and, in particular, describe Au (111).

The wavefunctions of individual atoms, referred to as orbitals, are not grouped into bands like they are in crystals; they are at discrete energy levels [122]. A molecule lies somewhere in between as the process of bonding fundamentally changes the orbitals to new 'molecular orbitals' where the electrons should be thought of as involved in the bond rather than bound to a particular atom.

The variation in the bonding of carbon makes it exceptionally versatile; so although molecules can be simple, like carbon monoxide and molecular oxygen, they can also become incredibly complex. In order to discuss such large collections of atoms chemists have identified 'groups' of atoms that can act as building blocks in our understanding of more complex molecules.

3.3.1 Phenyl rings, pyrrole and porphryin

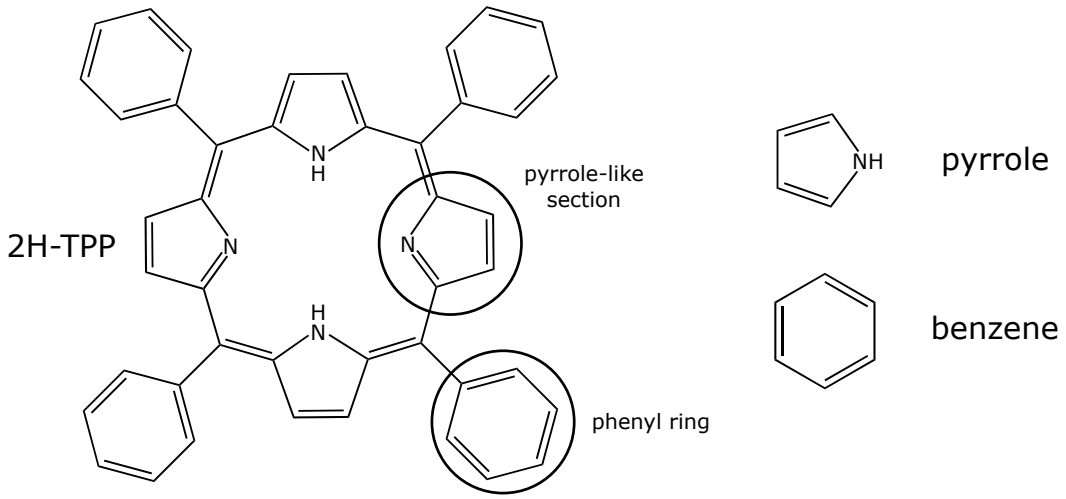

Figure 3.5: The structure of 2H-TPP consists of a central macrocycle and four phenyl rings. The phenyl rings bear a striking similarity to benzene, the only difference being that the bond to one of the hydrogen atoms now attaches to a carbon atom in the macrocycle. This carbon atom joins the phenyl ring to two pentagonal sections that resemble pyrrole, however, the centre of the macrocycle contains two rather than four hydrogen atoms and they are bound as described, losing a further two hydrogen atoms each.

In the case of some simple molecules, one can simply describe them atom-by-atom. Benzene, for instance, is comprised of six sp_2 hybridised carbon atoms arranged in a hexagonal ring. Each carbon atom is bonded to a hydrogen atom 'terminating' the molecule rather than forming an endless sheet: graphene. Because the π orbitals are all bonding to those on either side the electrons inside them are delocalised into a ring. A similar structure is the phenyl group (phenyl ring), which occurs commonly in more complex molecules. A phenyl ring differs from benzene in that one of the carbon atoms is bonded to something else.

Phenyl rings are a part of tetraphenyl-porphyrin (TPP) molecules, which are the main subject of Chapter 7. To make a porphyrin molecule, one first needs four pyrrole-like groups to construct a large ring called a macrocycle. Pyrrole consists of four carbon atoms and a nitrogen atom each bound to a hydrogen atom in

a similar manner to benzene. The nitrogen atoms point into the centre of the macrocycle and the carbon atoms on either side are bonded to carbon atoms which sit between pyrrole-like sections. Just two of the four central nitrogen atoms are bound to hydrogen, creating two species of nitrogen: the iminic nitrogen loses its hydrogen and the aminic nitrogen remains as if it were in pyrrole. So in the centre of the macrocycle, there are commonly only two hydrogen atoms or the hydrogen is replaced by a metal atom that complexes with them.

Tetra-phenyl porphyrins (TPPs) are the case where four bridging carbon atoms are bound to a phenyl group as well as the pyrrole-like sections. Importantly, the phenyl rings are able to rotate around these bonds. 2H-TPP is pictured in Figure 3.5 with showing the two hydrogen atoms in the core. The other porphyrin that is studied frequently in this work is ZnTPP, where a Zn atom replaces the hydrogen atoms.

3.3.2 Conformation

When a molecule adsorbs to a surface it adjusts its geometry to the new environment. In a complex molecule like a TPP different parts of the molecule attempt to distance themselves from each other to reduce 'steric' repulsion from the atoms coming too close and other parts of the molecule will interact with the substrate. Parts of a surface may be preferable for adsorption and if there are few molecules on the surface the majority of molecules will be found there. Double bonds or aromaticity may lead to certain parts of the molecule becoming rigid, further complicating the situation. The deformations in the molecule can be modelled and studied experimentally on different surfaces to learn more about the properties of the molecule.

However, molecules interact not only with the substrate but with each other. In some cases, it is favourable for molecules to lie on top of each other or for their geometry to be dominated by adjusting to other molecules. However, it is also common for beneficial interactions with the substrate to lead to molecules forming 'islands' which expand to cover the entire surface before they begin to lie on top of

each other in order to maximise the interaction with the surface [123]. In such an island they become arranged in a regular lattice referred to here as a molecular network. The exact parameters of the network depend on the balance of the molecule-molecule and molecule-substrate interactions. Examples of experimental studies of these phenomena can be seen in Section 3.4.

3.3.3 Au (111)

The exposed surface of a 3D crystal can vary dramatically depending on its orientation. By cleaving the crystal along a particular crystallographic direction, one can expose a particular surface, which offers different possibilities as an experimental substrate.

A commonly used surface is Au (111). The bulk Au crystal has a three-dimensional face centred cubic (fcc) lattice with lattice constant 4.07825 Å at 25 degrees Celsius [124]. The Au (111) surface could be considered as a 2D triangular lattice with a lattice constant of 2.88376 Å if it weren't for a surface reconstruction. The 'herringbone' reconstruction leads to continuous variation in the distance between atoms in the (110) direction as 2 extra atoms are added into a space which would normally have 22 atoms leading to a $22 \times \sqrt{3}$ unit cell [125, 126]. This leads to a periodic cell with a side 63 Å long, enclosing many times more atoms than a cell including only the atoms closest to a particular molecule.

3.4 Review of molecules on surfaces and conformation

In the development of the simulation used in this work, images of a variety of molecules were simulated. Here, I will discuss the images of these molecules acquired using NC-AFM (non-contact atomic force microscopy discussed in Section 2.4.2) with a particular focus on the tetra-phenyl porphyrin (TPP) molecules. Imaging

these molecules can be difficult because, as discussed in Section 2.4.3, NC-AFM is optimised for imaging planar species and struggles to measure molecules with more topographic variation. I will detail current approaches for acquiring information from tetra-phenyl porphyrins with scanning probe techniques and the information acquired with these approaches. Finally, key to my investigation of Zn tetra-phenyl porphyrins (ZnTPP) are the ways in which many TPP molecules arrange themselves on a metallic substrate. I will discuss the scanning tunnelling microscopy (STM) and polarisation-dependent NEXAFS observations on both the arrangements of the molecules and the ways the molecules adapt within this network by rotating their phenyl rings.

3.4.1 Imaging molecules with non-contact atomic force microscopy

As discussed in Section 2.4.2, the images of pentacene acquired by *Gross et al.* in 2009 first demonstrated the ability to operate NC-AFM with submolecular resolution [8]. The images were acquired by functionalizing the tip apex with a carbon monoxide (CO) molecule, an approach that had been pioneered in scanning tunnelling hydrogen microscopy (STHM: STM with a functionalised tip) [127].

Following the demonstration of sub-molecular resolution NC-AFM many planar molecules could be imaged, raising further questions. A topic of some debate was whether or not hydrogen bonds could be observed. Images of 8-hydroxyquinoline captured by *Zhang et al.* [128] certainly appeared to have observed hydrogen bonding (Figure 3.6a). Clear features could be observed between the molecules matching the expected positions of hydrogen bonds. However, as is discussed in Section 2.6.1, such features can be reproduced without any consideration for the electron orbitals using the Probe Particle Model [42, 43]. Indeed a very close replica of an image collected by *Zhang et al.* was created via the simulation [42] (Figure 3.6b). NC-AFM images of naphthalene tetracarboxylic diimide (NTCDI) molecules were imaged by *Sweetman et al.* [29] (Figure 3.6c) showing similar intermolecular

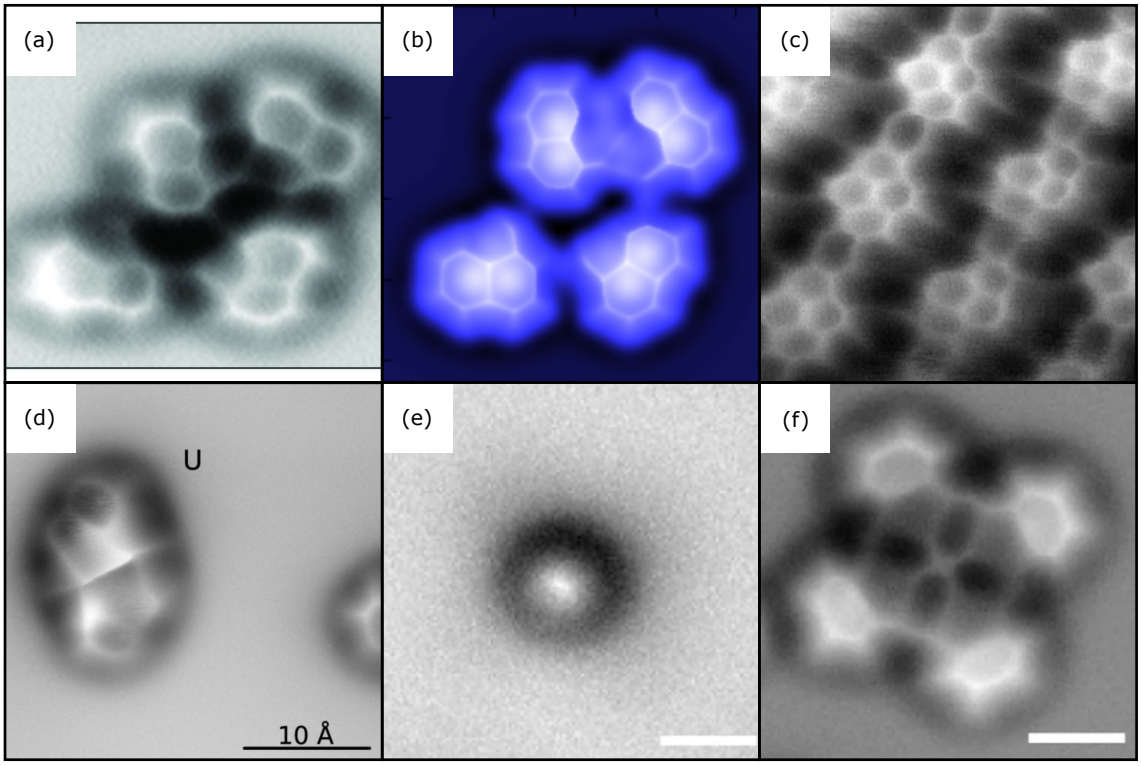

Figure 3.6: NC-AFM images of 8-hydroxyquinoline showing what seem to be hydrogen bonds *(a)* (Zhang J. et al. [128]. Reprinted with permission from AAAS.) are shown in comparison to simulated images *(b)* created with no consideration for bonding, highlighting that it is not possible to assign these features solely to the bond (Reprinted figure with permission from Hapala P. et al. [42]. Copyright 2014 by the American Physical Society.). Similar features seem to be observed in naphthalene tetracarboxylic diimide *(c)* (Reprinted from Sweetman et al. [29]) and a bond which doesn't exist is imaged between two sulfur atoms at the top of a Dibenzo[a,h]thianthrene molecule *(d)* (Reprinted figure with permission fromPavliček N. et al. [129] Copyright 2012 by the American Physical Society.). Finally images of iron phalocyanine with *(e)* and without *(f)* a CO molecule adsorbed on the iron atom (Reprinted from Chen P. et al. [44]).

features, but force curves $F(z)$ measured over those features show insufficient contrast relative to density functional theory simulated force curves expected over hydrogen bonds. The molecule Dibenzo[a,h]thianthrene DBTH is a fine example of this situation [129]. The two adsorption geometries on NaCl are like two frames from a butterfly's flight, one with the wings down and one with the wings up. When the wings are down, the sulfur atoms at its centre are the topmost atoms, but they are not bonded together. Nevertheless, as this part of the molecule marks a watershed for the CO molecule being deflected one way or the other a 'bond' is observed between the sulfur atoms as seen in Figure 3.6d.

The constraints on NC-AFM are clearly illustrated in the work of *Chen et al.* where a CO molecule adsorbed onto a Fe phalocyanine (FePc) was imaged using NC-AFM and compared with simulated images [44]. In the NC-AFM images, the CO molecule is removed via an interaction with the tip, showing that NC-AFM is unable to resolve features at the base of the molecule without interacting with the molecule (Figure 3.6e-f).

3.4.2 Non-planar imaging with frequency modulation atomic force microscopy

Strategies have been developed in order to overcome the limitations of NC-AFM when imaging non-planar molecules. The techniques can be split into two groups: either frequency modulation AFM (FM-AFM) is carried out whilst following a non-planar surface or data is collected over a volume rather than a plane. Often these techniques are used in tandem to get the best of both approaches.

In the first case, the trajectory of the tip can be determined by measuring the frequency shift whilst carrying out constant current STM [130]. Such a process is an established technique [39], but one can also use topographic information from FM-AFM with feedback turned on to approximate a force iso-surface for the long-range forces. Once the initial pass to find this surface is done, one can translate the trajectory closer to the subject and turn the feedback off. The result is that

the tip follows a path resembling another force iso-surface, closer to the subject and measures the deviations from that surface due to short-range forces which played little part in the first pass. The result for both imaging techniques is shown in Figure 3.7b-c.

The alternative method is to approach the surface, collecting frequency shift data $\Delta f(z)$, at many locations in order to create a line or a two-dimensional grid with a force curve or equivalent data at every point [33, 130, 132, 133, 134]. The grid of spectra gives the user a three-dimensional volume of data that can be sliced in many ways to show various pieces of information. By moving on to the next spectrum when the interaction measured by the tip is too strong higher regions of the molecule can be ignored whilst allowing the tip to move lower elsewhere [133] (Figure 3.7d). This approach was used by *Albrecht et al.* to observe the core of tetraphenyl porphyrin molecules and differentiate between those with a metal complex and those without [33] (Figure 3.7e).

Collecting force spectra has also been used to determine the angle of adsorption of ketone-like molecules on a Cu surface [134]. The surface of constant Δf was extracted from a three-dimensional dataset and it is shown in Figure 3.7f. NC-AFM does not give any quantitative information about topography, but a surface of constant Δf corresponds to an iso-surface of an unknown force which can be calculated if so desired. This surface should follow the topography of the molecule and, for a planar molecule such as ketone, one can fit a plane to the surface to extract the angle relative to the substrate.

The more data is collected the longer these techniques take. Thermal drift and error from the equipment can compound to cause significant motion on such a small scale. As a result, atom tracking protocols to continuously correct for drift are key to successful imaging in this manner.

These techniques were used to identify the adsorption geometry of some TPP molecules on metallic surfaces. In the gas phase, porphyrins tend to adopt a planar geometry with the phenyl rings rotated by $\sim 60°$. When adsorbed to a metallic

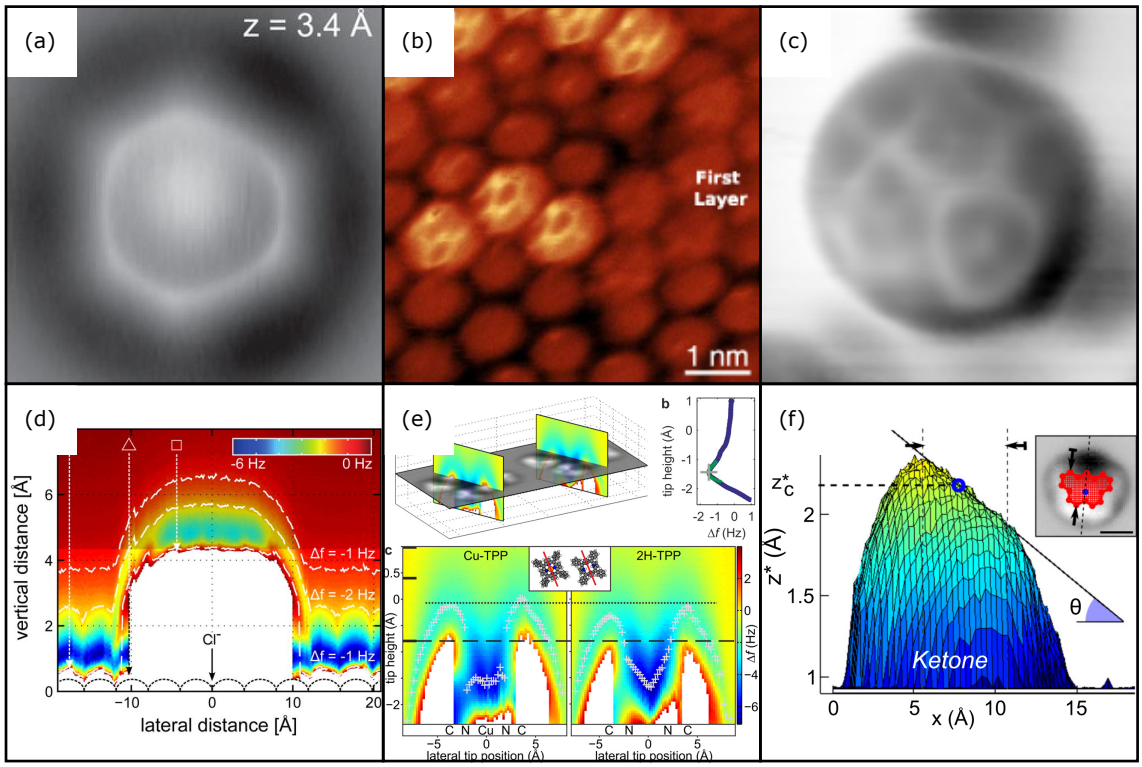

Figure 3.7: C60 imaged by NC-AFM (From Gross et al. [131]. Reprinted with permission from AAAS.) *(a)* and by carrying out FM-AFM during STM *(b)* (Used with permission of Institute of Physics (Great Britain) from "High-resolution imaging of C60 molecules using tuning-fork-based non-contact atomic force microscopy", Pawlak R et al.[130] copyright 2012. Permission conveyed through Copyright Clearance Center, Inc.) and following a trajectory where the long-range force should be constant *(c)* in order to reveal more of the molecule (Reprinted (adapted) with permission from Moreno et al. [132] Copyright 2015 American Chemical Society.). By carrying out force spectra along a line one can collect a two-dimensional image of pentacene *(d)* (Reprinted from Mohn F. et al. [133] with the permission of AIP Publishing.) or by applying the same technique one can discriminate between tetraphenyl porphyrin molecules with and without metalled cores *(e)* (Reprinted (adapted) with permission from Albrecht et al. [33]. Copyright 2016 American Chemical Society.). By collecting a three-dimensional dataset one can extract surfaces of constant frequency shift and determine the angle of adsorption of a molecule *(f)* (Reprinted with Permission from Schuler B. et al. [134]. Copyright 2013 by the American Physical Society.).

surface, many porphyrins rotate their phenyl rings closer to 20° and the macrocycle distorts in order to accommodate this into the 'saddle' geometry [15, 135]. A pair of opposing nitrogen atoms in the macrocycle point downwards slightly, tilting the other end of the pyrrole unit upwards and the other pair points upwards creating a saddle shape. The phenyl rings tilt away from the raised pyrrole, minimising the steric interaction. The raised pyrroles and the edges of the phenyl rings which are tilted upwards beside them create two sets of three raised sections which are observed in the NC-AFM image displayed in Figure 3.8a.

TPP molecules at cryogenic temperatures have been observed to adopt two arrangements at cryogenic temperatures. In an STM study of brominated CoTPP on Cu (111) a saddle and a 'planar' adsorption were initially suggested with the saddle geometry being assigned as the elongated geometry by *Iancu et al.* [136]. Via comparison of STM images of brominated 2H-TPP with DFT *Jarvis et al.* suggested that the square molecule was the standard saddle shape and the elongated version was simply a variation where the phenyl rings were pushed further from the pyrrole groups by the steric interaction [31, 137]. Then studies of 2H-TPP where NC-AFM scans were adapted to avoid the central raised region to image the remainder of the molecule and by imaging a $\Delta f = 0$ iso-surface *Albrecht et al.* were able to show conclusively that the elongated molecule was in fact a peculiar adsorption geometry termed the 'inverted' geometry. Here the iminic pyrrole is tilted to an extreme degree where it is almost vertical and the aminic pyrrole is almost perfectly flat. This, in turn, is the source of the steric repulsion which *Jarvis et al.* identified pushes the phenyl rings into the elongated shape and flattens them against the substrate. The saddle and inverted geometries are shown in Figure 3.8b-c.

3.4.3 Networks of tetra-phenyl porphyrins

When molecules aggregate into groups they influence each other via molecule-molecule interactions, creating new adsorption geometries and arranging themselves into a lattice referred to here as a molecular network. The conformation of TPP

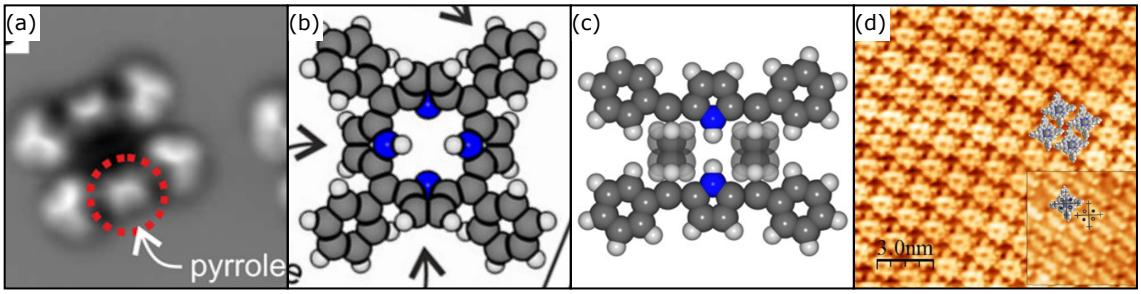

Figure 3.8: An NC-AFM image of CuTPP on Cu (111) in the saddle geometry *(a)*. The saddle and inverted geometries are shown in *(b)* and *(c)*. These three images are reprinted (adapted) with permission from Albrecht et al. [33]. Copyright 2016 American Chemical Society. Porphyrins form molecular networks such as this network of ZnTPP imaged using STM on Au (111) (Reprinted with permission from Ruggieri et al. [123]. Copyright 2015 American Chemical Society.) .

molecules has been studied extensively and some degree of consistency has been found in the parameters of the networks made by the whole family.

Auwärter et al. carried out an STM study on Ag (111) of free base and Fe tetra-pyridyl porphyrins (TPyP) and Fe tetra-phenyl porphyrin [138]. Pyridyl is similar to a phenyl ring, but the carbon atoms furthest from the core are replaced by sulfur atoms. Whilst TPyPs showed two arrangements which alternated, creating a unit cell of 13.9 Å by 27.4 Å containing two molecules, the TPPs had a square cell of 14.3 ± 0.2 Å. In an earlier study by many of the same authors, 2H-TPyP had been found to have a similar cell of sides 13.9 ± 0.2 Å and 27.4 ± 0.2 Å $93 \pm 2°$ apart [139]. These distances seemed to have no factors of the underlying lattice, suggesting that the molecules were not commensurate with the lattice below, a view which is supported by a visible Moiré pattern in STM images. By simulating the aspect ratio of the molecule when the pyridyl groups are rotated at different angles relative to the surface and then comparing the aspect ratios to STM images, the angle of the phenyl rings was determined to be $\sim 60 \pm 5°$.

NEXAFS measurements of FeTPP on MoS_2 measured the angles of the phenyl rings to be 59° by measuring polarisation-dependent measurements [140]. Other metal centres have been studied though. STM images by *Scudiero et al.* were used

to identify the lattice constants of Co and Ni TPP on Au (111) to be 14.1 Å[141]. Similar values of 14.2 and 14.1 Å were acquired for Co-TPP on Cu (111) by *Weber-Bargioni et al.* [142] and 14 Å in another paper by *Auwärter et al.* on Ag(111) [143]. Both works also offer values for the angles of the phenyl rings collected from polarisation-dependent NEXAFS: 35° and 45° respectively. However, on Cu (110) CoTPP experiences an extreme distortion in two possible mirrored domains observed in STM images by *Donovan et al.* [144]. The angles of the phenyl rings in one of the domains were determined through DFT calculations with references to the experimental images. The corrugations of the (110) surface lead to phenyl rings which are rotated by angles ranging between 60° and an extreme 88°. However, this deformation results from the (110) surface and the work discussed so far has been on (111) surfaces.

Further NEXAFS studies were carried out by *Diller et al.* on Cu (111) of a monolayer of 2H-TPP created by annealing a multilayer sample until enough material desorbs [145]. This annealing led to metallation and the angle of the phenyl rings varied between the free base and metalled TPP molecules. 2H-TPP has phenyl rings angled at 20°, but metallation leads to a change to between $40 - 50$ degrees.

In this work, the system under investigation is ZnTPP on Au (111). An STM study of this system by *Ruggieri et al.* gives lattice parameters of 13.1 and 12.6 Å and *Zhang et al.* measure similar values of 13 and 12 Å[123, 146]. However, *Yoshimoto et al.* and *De Luca et al.* measure a much larger unit cell of 14 Å, with *De Luca et al.* measuring a longer side 14.4 Å long [147, 148]. In addition, *Ruggieri et al.* provides a potential unit cell described in terms of the Au (111) lattice vectors which will examined in Chapter 7.

In summary, one can see a clear trend, in most cases the lattice parameters are measured to be approximately 14 Å, though it is notable that two studies measured vectors approximately 12 and 13 Å long in the ZnTPP on Au (111) system specifically and not elsewhere. The lattice vectors are generally reported to be approximately 90° apart and most phenyl rings on (111) surfaces are rotated

between 20° and 60°. This presents a parameter space within which to begin our investigations of conformation in networks of ZnTPP on Au (111).

Chapter 4

Methods

In order to gain as much information as possible about a system it is important to choose the optimal technique. The demands of imaging non-planar molecules stand quite apart from those of imaging exceptionally flat TMD surfaces and, as a result, different approaches are required in order to image these dissimilar systems.

In the case of non-planar molecules the difficulty lies in the variation in height. How can sections of the molecule closest to the substrate be measured without the tip interacting too strongly with other sections of the molecule? However, point defects are located on a single site on a largely flat surface and the core challenge is resolving individual atoms through the noise and contamination of an ambient environment. Here we detail the SPM techniques, and simulations of those techniques, that enable high resolution imaging of their respective systems.

The Isolab facility plays a key role in the resolution of all of our AFM measurements. The facility is separate from the rest of Lancaster University Physics Department on it's own foundations. The work is carried out in pods which are specially adapted to isolating measurements from mechanical vibrations. The equipment rests on top of a 50 ton concrete block which can be raised on air springs; when coupled with heavy tables and granite blocks the vibrations are further attenuated at each interface due to the sudden change in resonant frequency due to a change of mass. As a result the noise floor from mechanical vibration is

exceptionally low. The mains electrical supply is filtered and grounded separately to the Physics Department via multiple earth spikes. Atomic force microscopy and electrical measurements carried out in these pods enjoy exceptionally low noise floors that routinely drop below 10 pm in the topographic signal during ambient measurements. This improves the quality of our data and reveals features which would otherwise be lost in the noise. All of the AFM measurements and the cryogenic photoluminescence measurements have benefited from this facility.

4.1 Constant Force AFM

4.1.1 Measurement of Constant Force AFM

Across my PhD topographical images were taken using a constant force AFM method in ambient conditions. The measurements were taken using a Bruker Multimode 8HR AFM controlled by a Nanoscope controller in PeakForce Tapping mode and NuNano SCOUT probes. This was also the experimental equipment used to collect the images I was interpreting via simulation. The details of the experiment are given in Chapter 7 and the method of simulation will be outlined here.

4.1.2 Simulation of Constant Force AFM

In order to simulate imaging using a constant force method we chose to find the force iso-surfaces that constant force AFM is trying to image. Here I effectively assume that the microscope follows the iso-surface without deviation, which is of course impossible for an instrument which uses feedback. However, there is no point in simulating noise and problems with gain as these are either unpredictable or minimal if the system is operated successfully.

My simulation is written in Python and interfaces with the 'Probe Particle Model' (PPM) [42, 43], which calculates the force experienced by the tip at a point in space. The PPM is provided with atomic coordinates in a .xyz file detailing the

element and the x, y and z coordinates. This data can be used to create a force field of the Van der Waals forces experienced by the tip. This is done by simulating the component of the force experienced by the tip in the z direction at discrete points in a 3D grid with periodic boundary conditions.

Electrostatic forces can also be considered by adding an extra column to the .xyz file detailing point charges for the atoms or by providing a simulation of the Hartree-Fock potential for the simulation cell.

Once the forcefield has been calculated the model simulates tip relaxation. The PPM models the AFM tip as two particles. One particle, the titular probe particle, interacts with the sample and the second particle. This second particle effectively acts as a stand-in for the rest of the cantilever. The probe particle has a Hooke's constant that confines it in the x-y plane and a Hooke's constant that models the interaction with the second particle by providing a 'radial' force acting along a line between the two particles. These two forces are brought into equilibrium with the Van der Waals surface forces by moving the probe particle. As only discrete points in the force field have been found, linear interpolation is used to approximate the force in between these points.

In the standard usage of the PPM slices of the new, relaxed, force field can be used to simulate constant height images. However, by taking this relaxed data I can simulate constant force images. The Python script used in this simulation rearranges the relaxed data into a 2D grid of columns rather than a stack of 2D grids and then finds a value of z from each column. For each column the program considers each voxel, descending from top to bottom; towards the surface. If the force is greater than the setpoint for the desired iso-surface, the program checks if the previous voxel was less than the setpoint. If this condition is met, the z value is recorded and the next column is considered, if not the next voxel in the column is considered. In such a manner a grid of z values corresponding to unique x-y positions has been found that can be plotted. This plot is an approximation of the force iso-surface limited by the resolution of the various sections of the simulation.

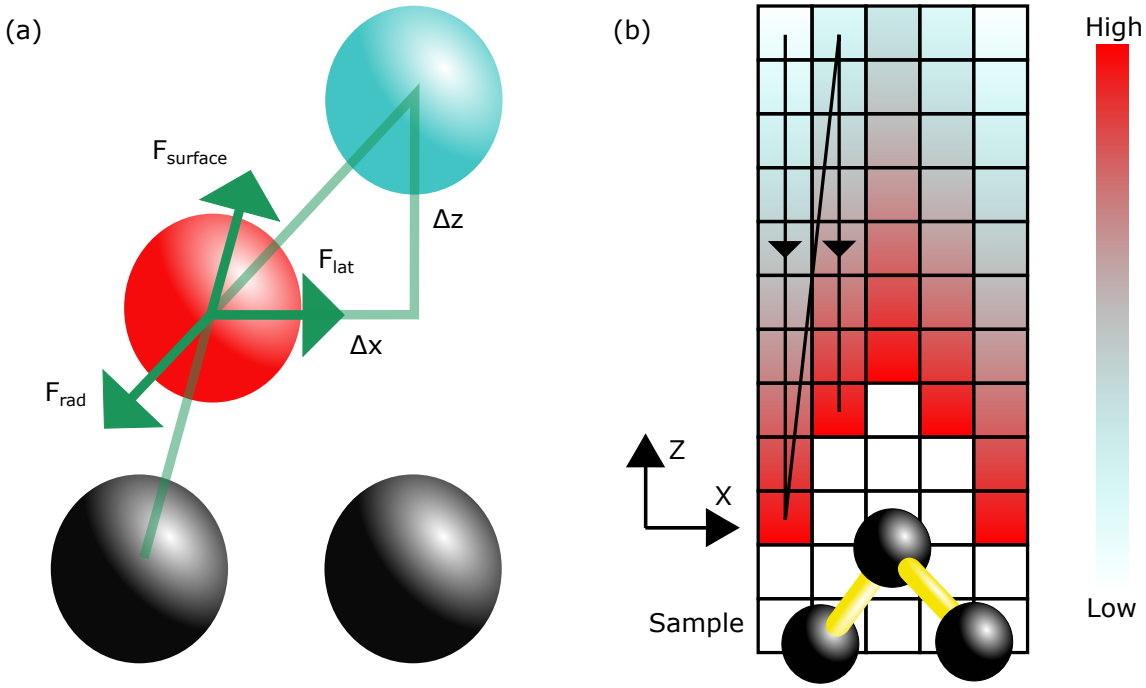

Figure 4.1: A force diagram *(a)* showing the forces considered in the probe particle model. The probe particle (red) experiences restorative forces in the x-y plane (F_{Lat}) and along the 'radial' direction (F_{rad}) from the second particle (teal) balancing the measured force from the atoms inputted ($F_{surface}$). The operation of the constant force AFM simulation script is also shown in a schematic *(b)*. The algorithm descends down columns of voxels in turn until it detects the force setpoint, then moves on to the next column.

In this manner iso-surfaces of molecules on surfaces can be calculated. The final result is outputted as a .gsf file which can be imported into the AFM data analysis software Gwyddion from which the file may be visualized and saved as a variety of useful file formats.

4.2 Conductive Atomic Force Microscopy

The cAFM equipment that I used to collect the cAFM images in this work is pictured alongside a circuit diagram in Figure 4.2. The cAFM measurements were made with the Bruker multimode 8HR AFM from a Nanoscope controller. The conductive probes were Nanoworld CDT-FMR probes with a doped diamond coating which the

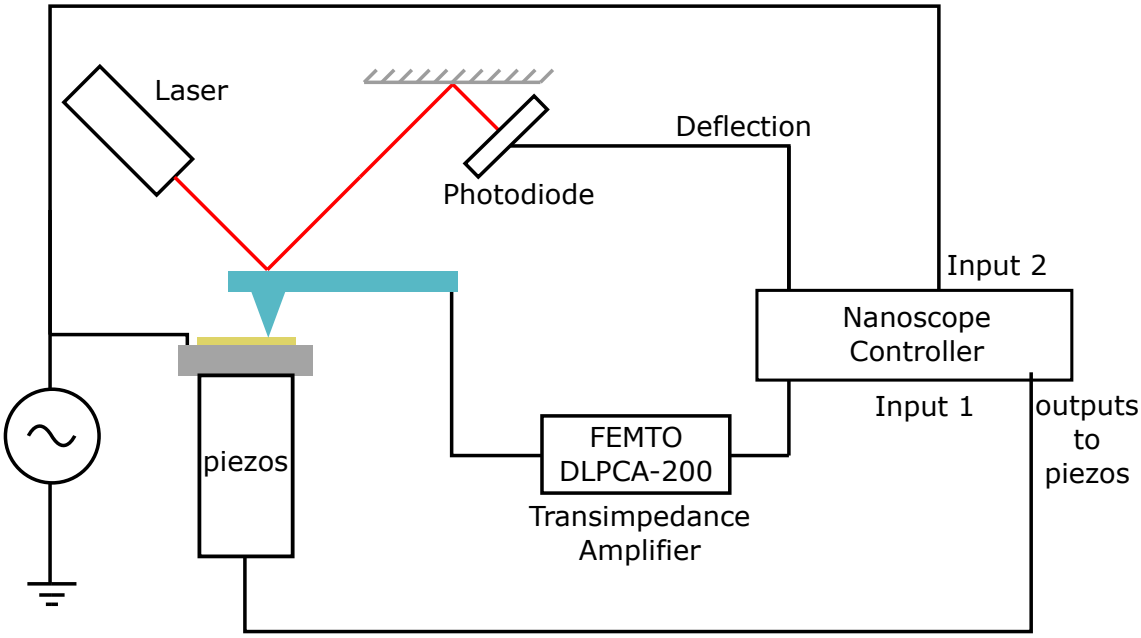

Figure 4.2: A circuit diagram showing the experimental set-up for cAFM used in this work.

manufacturers claim possesses a nanoroughness "in the 10 nm region".

In order to achieve atomic resolution, I made measurements at low deflection setpoints (5 nm or less) with doped diamond tips (Nanoworld CDT-FMR). The doped diamond coating facilitates the conduction but is crucial to our measurements in other ways because it is inert and stable. The high forces experienced in contact with the surface threaten to change the tip apex, blunting tips and preventing the observation of consistent images. The surface of a material in an ambient environment is also covered in many potential reactants to interact chemically with the tip, especially with the addition of the bias voltage. The stability of diamond tips in both a mechanical and chemical sense makes them ideal candidates for attempting to optimise the resolution of cAFM.

4.3 Fabricating Two Dimensional Samples

4.3.1 Mechanical Exfoliation

Methods of mechanical exfoliation can vary based on the resources and equipment available to a group, the experience of its members and the material itself. The method of exfoliation detailed here yields monolayer samples of TMDs often enough that at least one monolayer flake is commonly found on a PDMS stamp.

In this work, I used Nitto Blue Tape (Acrylic/PVC) to exfoliate MoS_2 , WSe_2 and WS_2 and hBN from bulk crystals. The tape pulls a number of layers off the top of the crystal, so by folding the tape onto itself and then pulling the tape apart the material is distributed around the tape and some of the crystals are pulled apart, reducing the number of layers. I initially exfoliated 2D materials onto 'seed' tapes, and then from those tapes onto another piece of tape. This separates the seed tape from the sample, maintaining a cleaner source. I folded my tapes approximately 8 times after exfoliation from a seed tape.

This tape can then be used to exfoliate the flakes onto a PDMS stamp of approximately 1 cm x 1 cm dimensions. The tape is pressed into the PDMS stamp and then carefully pulled back until a corner of the stamp is no longer in contact. I then pulled the tape away rapidly, leaving flakes of various thicknesses behind on the PDMS stamp. In Sections 4.3.2 and 4.3.4 I will detail the process of identifying monolayers and transferring them onto the experimental substrate.

4.3.2 Identification of monolayer TMDs via Raman and photoluminescence spectroscopy

Once flakes have been exfoliated onto a PDMS substrate it is necessary to determine which flakes are monolayers. Photoluminescence and Raman spectroscopy offer a fast and reliable way to differentiate monolayers from few-layer flakes.

I could disregard the majority of flakes by eye when viewed from an optical

microscope. In this work, a Zeiss Axio Lab.A1 optical microscope was used to identify the few possible monolayers on a PDMS stamp. Monolayers are a similar colour to the PDMS relative to the thicker sections which are often blue, purple or even opaque white for the thickest sections.

Once potential monolayers are found, I placed them on the Horiba LabRAM with a Horiba Synapse CCD. I then found the flakes using a x10 magnification lens and then focussed a 532 nm solid state laser onto the flake via a x100 magnification lens.

Between Raman and photoluminescence, monolayers can be identified before transfer to the substrate for cAFM using the features discussed in Section 2.8.

4.3.3 Selection of Experimental Substrates

In order to carry out cAFM, a current must be able to pass between tip and sample. As a result, carriers must be drained or sourced or the sample will act as a capacitor and current will only be measured transiently when the bias voltage is changed. A simple way to do this is to use a conductive substrate and then attach the sample to a metal sample plate via silver paint or by clamping the substrate with a metal clamp. The sample plate can then be connected to a wire via a 'spade' which can be crushed into the sample plate by turning a screw.

In order to ensure a good electrical connection between the 2D flakes and the substrate we desire a conductive substrate with an exceptionally flat surface. Highly ordered pyrolytic graphite (HOPG) seems well suited for such constraints. HOPG is formed of layers of graphene bonded by Van der Waals forces. As a result, the surface of HOPG consists of atomically flat terraces of carbon atoms with occasional steps between the layers. An additional advantage of using a Van der Waals layered material as a substrate is the ability to remove the top layers to reveal a new, clean surface. As a result, I exfoliated HOPG using Loadpoint 6034 Acrylic/PVC Blue Tape before the transfer of the sample flake began. HOPG has been shown to possess domains with differences in potential over the scale of microns in electrostatic force

microscopy measurements [149]. In the experiments measured here we were able to find regions that were consistent enough to acquire our images.

4.3.4 Transfer of samples onto measurement substrate

Once 2D flakes had been exfoliated onto PDMS I needed to transfer them onto the target substrate of either HOPG or SiO_2. Direct exfoliation onto HOPG is not viable because the procedure will likely exfoliate the substrate itself. In this work I used a bespoke transfer system to transfer TMD flakes with the deterministic dry transfer technique. No solvents were used except to clean equipment prior to use. The stamp was simply pulled away from the substrate. For samples on SiO_2 the samples were heated up to $\sim 65°C$ using a heater below the substrate before the slide was raised. Without heating the substrate to soften the PDMS transfer onto SiO_2 had a low rate of transfer and often damaged the flakes.

Annealing samples to remove contamination is possible, but risks the formation of new defects. As we intend to study the defects in the samples after exfoliation we do not want to create extra opportunities for defects to form in this work.

4.3.5 Removing contamination and ensuring surface conformation

Following transfer, contamination is present in the interface between the flake and the substrate. In order to remove the contamination I adopted the approach dubbed the 'Nano-Squeegie' technique in order to ensure I could perform cAFM on a flat surface with a consistent electrical connection to the substrate [22, 150]. In contact mode, using NuNano SCOUT probes in the Bruker Multimode 8HR AFM and the Nanoscope controller, contamination on the surface is easily swept away at a 5 nm deflection setpoint with a scan rate of 2 Hz. The contamination between the flake and the substrate is slowly removed over the course of many scans with a deflection setpoint of 30 nm. A cartoon representation of this process is depicted in Figure 4.3

alongside AFM scans showing the progression of the flattening process. The longer the surface is swept in this manner, the more the contamination is removed, but the user gains decreasing returns as the remaining contamination is sheltered by step edges or in large bubbles. Because the flake can rip due to repetitive forces at the edges, at some point the user must decide when to move on to making cAFM measurements.

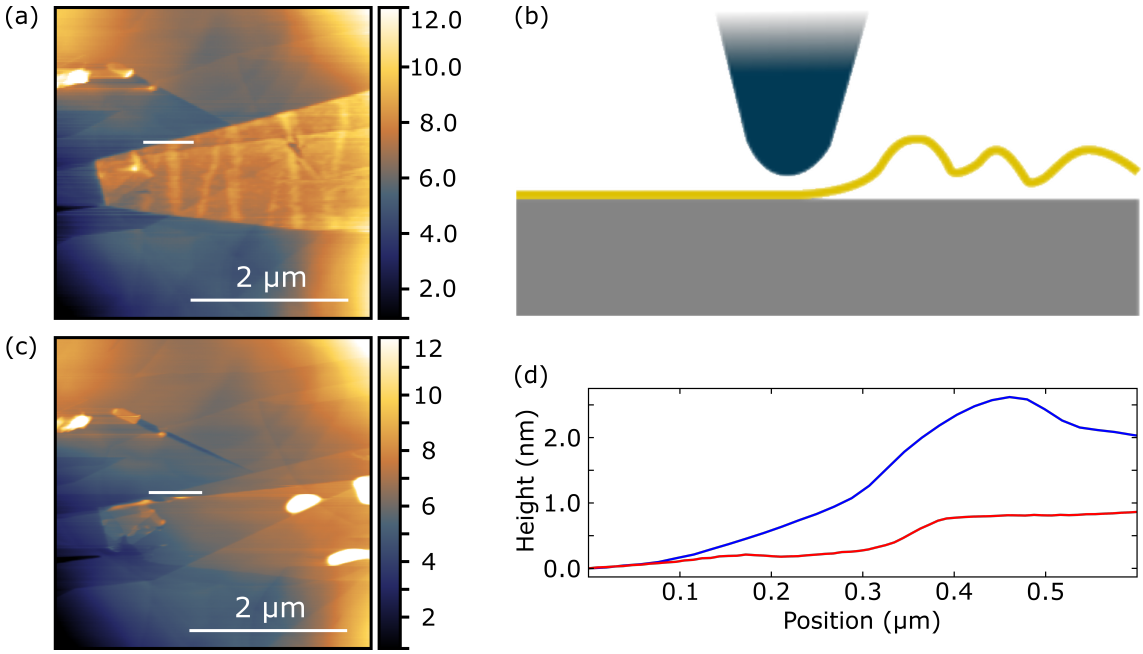

Figure 4.3: After transfer 2D crystals, such as this WS_2 monolayer imaged with contact mode AFM *(a)*, are separated from the HOPG substrate by contamination. The nano-squeegie technique uses an AFM tip to sweep contamination from beneath the flake *(b)* leading to better conformation to the surface *(c)*. Profiles taken before and after from the AFM images are shown in (d), showing a significant decrease in the thickness of the flake.

4.4 Acquiring high resolution in energy for photoluminescence measurements

In order to acquire photoluminescence data in which the individual peaks in a TMD's spectrum can be resolved it is necessary to cool the system to near absolute zero.

As the temperature of the sample falls, thermal broadening due to the Boltzmann distribution of the energy of electrons near the chemical potential is reduced. As a result, the electrons are excited from a more consistent energy, are less likely to interact with phonons during the light-matter interaction and then decay back to a more consistent energy. This means that the energies of emitted photons lie closer to the idealized energy of the decaying exciton.

In order to take measurements at cryogenic temperatures our samples were cooled in an Attocube attoDRY800 cryostat using a Sumitomo HC-4E Compressor. The sample chamber contains Attocube piezo scanners (ANPx311 for x and y and ANPz102 for z) that allow the user to precisely position samples attached to the top of the stack. These scanners can be controlled via the Attocube ANC350 Piezo Motion Controller and ANC350 SpaceNavigator which can be, in turn, controlled by the computer. The chamber is closed with a window through which the sample can be observed and probed optically.

Samples can be illuminated with an LED allowing the user to observe the sample via a camera and a lens which can be positioned above the window. This enables the user to find their sample and focus on it before taking photoluminescence measurements.

During photoluminescence measurements, a PicoQuant PDL 800-D Drives a 560 nm laser in 'continuous wave' mode. A beam splitter samples $\sim 1/6$ of the light to be sampled after attenuation via 2 attenuating disks, enabling the user to select the incident power on the sample. The laser is focused onto the sample through the lens above the window. The reflected and re-emitted light then travels back through the lens and into the SR-500i Spectrometer with an ANDOR Newton^{EM} CCD.

A heater and temperature sensor near the sample allow for more accurate temperature readings and the ability to select a sample temperature. The base temperature of the fridge is approximately 8K in the arrangement used in my work, but it can be raised to near ambient temperature using PID feedback. As a result, the system has two main input variables: Temperature and laser power. A detailed

description of the system can be found in the thesis of Christopher Woodhead [151].

4.5 Defect engineering

In order to generate defects in some of our samples, I exposed them to a N_2 plasma. The basic idea of a plasma reactor is to use an electric field to create charged ions in a gas, which then interact chemically with the subject.

The reactor used in this work was a boro-silicate glass chamber in a cruciform shape, as seen in Figure 4.4, with 4 metallic end pieces at which the chamber could be accessed or elements could be added. The chamber can be pumped down or vented through one of these end pieces, which also contains a pressure sensor for the chamber. A tube connects to a venting valve and via another valve to a cold trap and pump. The trap is filled with liquid nitrogen and significantly improves the ability of the pump. On the opposite end of the cruciform chamber a bottle of compressed nitrogen gas is connected via a regulator and a valve allowing a pressure to be set behind the valve and then, by using the pressure gauge whilst the system is being pumped down, nitrogen gas can be added into chamber to achieve the desired pressure. Samples can be added or removed from the chamber via a 3rd end piece. The electrical field is applied via a coil around the chamber which is connected to a power supply applying signals at 13.56 MHz up to a power of 100 W.

The system is operated by pumping the system down to base pressure and then cleaning with N_2 plasma for 10 minutes at a pressure of 10Pa and a power of 40% without a sample. The system is then vented and samples are placed in a consistent position in the cruciform arm closest to the entrance. The system is then re-evacuated and the samples are exposed to the plasma at the desired parameters.

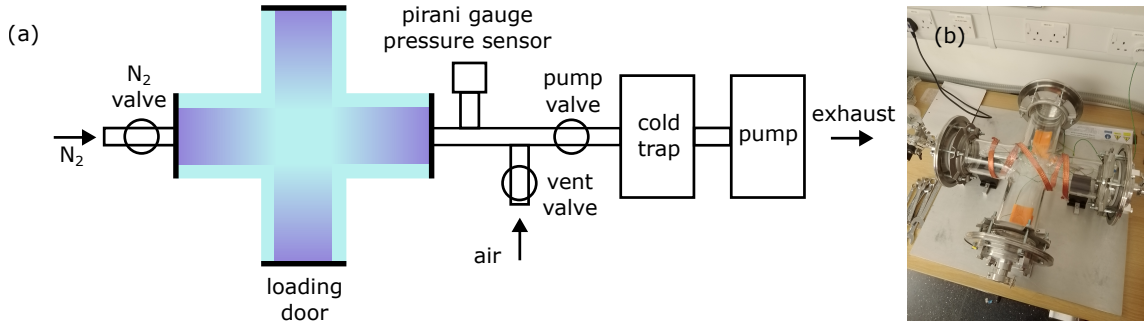

Figure 4.4: A diagram showing the bespoke plasma reactor used to expose samples to N_2 plasma *(a)* and a picture of the cruciform reactor barrel *(b)*.

Chapter 5

Results: formative defect density in transition metal dichalcogenides

The collection of atomic resolution images in an ambient environment is an exciting development that will enable faster and more readily available material characterisation on the atomic scale. In this chapter, I will demonstrate the characterisation of the defects observed in mechanically exfoliated TMD monolayers with cAFM. The samples will not be exposed to any further processing such as annealing or plasma exposure, which will be explored in Chapter 6. Through this lens, we will contrast the density of the defects between MoS_2, WSe_2 and WS_2, which should differ relative to synthetic samples [152], and discuss the chemical origin of the observed features.

Two dimensional TMD monolayers on a substrate of highly ordered pyrolytic graphite were created by the mechanical exfoliation, identification and transfer method outlined in Chapter 4. After using the 'nano-squeegie' technique to remove contamination, the TMDs were observed using cAFM.

5.1 Identification of TMD monolayers

Some representative spectra indicating how monolayers are identified using the criteria in Section 3.2.3 can be found in Figure 5.1. The E^1_{2g} and A_{1g} peaks can be seen to be significantly closer in the Raman spectra of flakes identified as monolayer MoS_2 and WS_2 samples. The monolayer WSe_2 flake, again, can be clearly distinguished from the few-layer sample due to the change in the position of the WSe_2 peak to the opposite side of 260 cm^{-1}. The photoluminescence spectra from WSe_2 and WS_2 see large increases in the intensity of their peaks in the monolayer case and in the case of MoS_2 the disappearance of the 'I' peak at 800 nm could be used if the information from the Raman spectra is insufficient.

5.2 Conductive atomic force microscopy

The samples were approached gently with a deflection setpoint of 5 nm as described in Chapter 4. Topographic images obtained simultaneously with cAFM current channel images show a periodicity due to the lattice but fail to observe atomic imperfections. However, as is shown in Figure 5.2 the current channel images show the presence of defects. The majority of current channel images show the lattice clearly, but in approximately 40% of cases, a Nanoworld CDT-FMR AFM tip observed atomic resolution images on our samples.

The ability to observe atomic resolution images in an ambient environment was not expected, not least because cAFM is a contact mode technique. The high forces involved in contact mode were expected to result in a blunt apex with a resolution of a few nanometres. However, the defect in Figure 5.2 clearly shows a variation in current that is unique to the site of a particular atom. The image clearly achieves atomic resolution. Achieving such resolution requires a sharp tip apex, where a single atom projects beyond the others as discussed in Section 2.5, so this apex must survive the forces. The stability of the diamond conductive coating likely plays a role due to the strength of the sp^3 carbon bonds. However, a 5 nm deflection

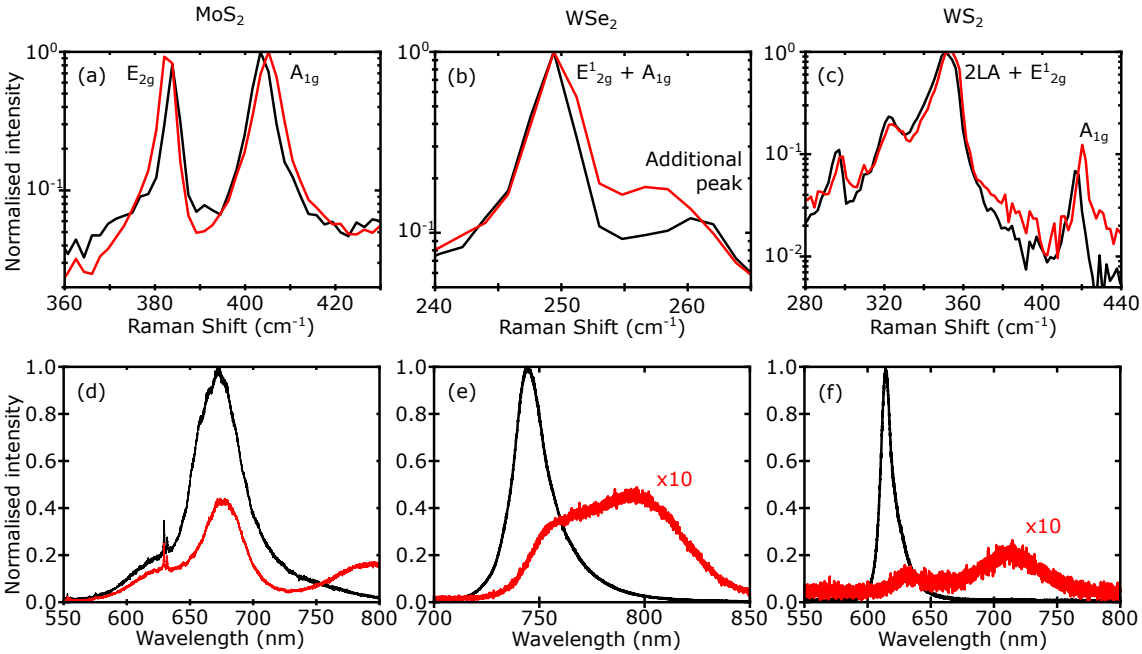

Figure 5.1: The Raman spectra of MoS_2, WSe_2 and WS_2 *(a-c)* normalised individually and PL spectra of the same crystals*(d-f)*, normalised to the height of the monolayer peak. The monolayer spectra are presented in black and the red lines are from thicker regions. Monolayers can be identified using the distance between the E_{2g} and A^1_{2g} peaks of MoS_2 [50, 102], the position of the additional peak above the degenerate combined E^1_{2g} and A^1_{2g} peak [70]. The Raman spectra of WS_2 is more complex. All 3 crystals see a dramatic increase in the peak intensity of the PL signal in the monolayer case, but TMDs containing W saw an increase of over an order of magnitude. Because the PL signal is weaker on MoS_2 thin peaks from the PDMS substrate can be observed [153].

with such tips should result in a force of ~ 31 nN: colossal by NC-AFM standards.

Due to the fact that contact mode is not considered to be an atomic resolution technique, the manner in which software operating contact mode AFM operates may not be optimised for such a use. Nanoscope, which was used to run our measurements, does not account for any drift in the deflection signal during the approach, evidenced by false engages when the signal drifts above the setpoint. Such a change can be minimized by reducing approach times, but it is important to realise that the actual deflection of a tip during contact mode AFM is not exceptionally reliable. It is totally possible that the success rate of atomic resolution measurement

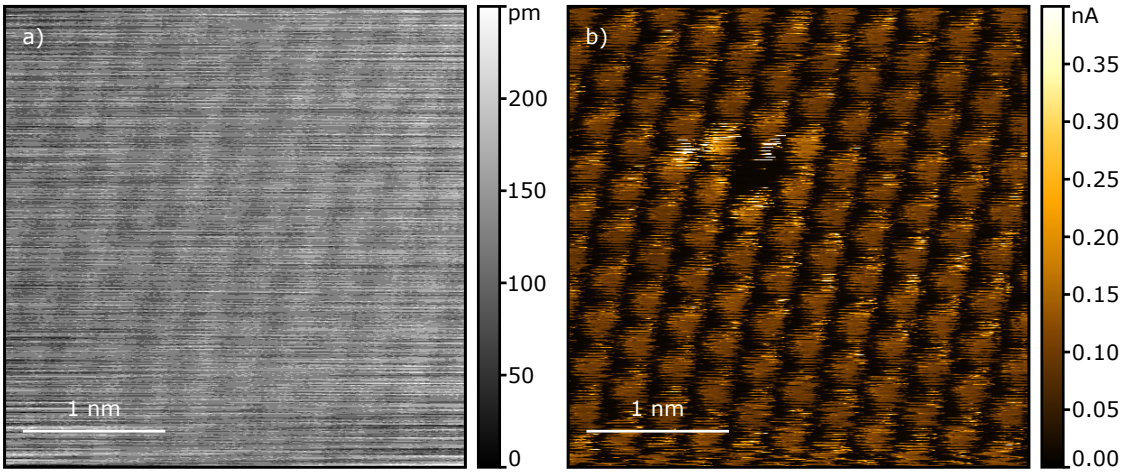

Figure 5.2: Two simultaneous images showing the topography *(a)* and current *(b)* channels from performing cAFM on MoS_2 using a bias voltage of 0.5 V. The resolution in z for the topographic image is very low because small feedback parameters are used and the measurement is optimised for the cAFM signal. Nonetheless, the rows of atoms can be observed, but the defect is not resolved in the topography, but the current channel image shows clear depletion over the defective atom and an augmentation on the nearest neighbour sites.

could be dramatically improved by an increase in the reliability of this information.

5.3 Defects in MoS_2

Initially MoS_2 was chosen as a subject because there is a great deal of work with other techniques which our observations can supplement [24, 72, 75, 77, 78, 104, 105, 106, 107, 108, 109]. The most commonly observed defects are localised depleting defects, such as the defect in the current channel image of Figure 5.2. The depletion on the site is contrasted by its nearest neighbours, which have been augmented by approximately 50% relative to the surrounding atoms which has been observed in STM images and simulations [9, 72, 75, 78, 115] Further images in Figure 5.3 show additional examples over a larger region of space, displaying their density.

A second type of defect is also on display in Figure 5.3, localised augmenting defects. Assignments as augmenting or depleting defects must be done with care

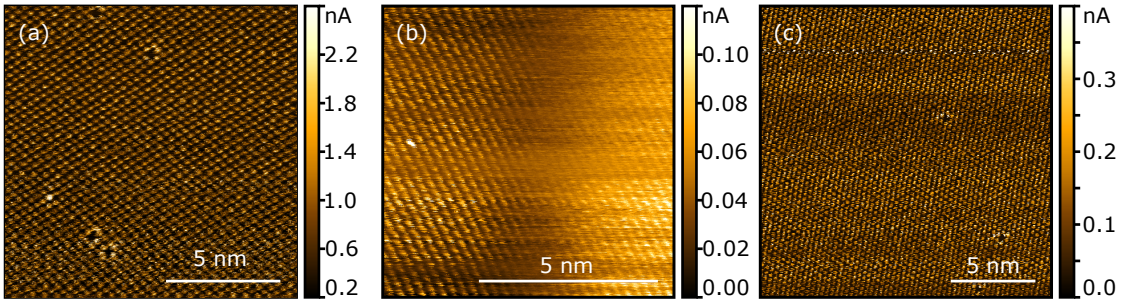

Figure 5.3: A current channel cAFM image showing augmenting and depleting defects in MoS_2 *(a)*. This image displays the density of defects and captures both types of localised defects in one scan without a significant tip change. An image of a localised augmenting defect is shown on its own *(b)*, but later in the same imaging session the only defects observed were depleting defects *(c)* which indicates the need to consider how the tip influences images. The images were taken by applying a bias voltage of 0.5 V.

because cAFM is a contact mode technique. Measurements can be subject to frequent tip changes due to picking up and depositing contaminants and changes in the structure of the tip apex. Such changes lead to variations in the current, resolution and, in some cases, the appearance or disappearance of artefacts such as a double tip. However, by taking a large number of images across many imaging sessions some level of consistency emerges. Figure 5.3b shows a defect that appears augmenting however, after a tip change, the only defects visible in the sample were depleting defects in Figure 5.3c. As the defect in Figure 5.3c is more consistent with other measurements such as Figure 5.3a this is thought to be a more reliable representation of the defects in that sample. A more thorough discussion of the variation in our images will be presented in Section 5.5.

When the cAFM cannot image localised defects with atomic resolution they often appear as augmenting defects. This may be because the augmentation that surrounds depleting defects sums to a greater increase in the current than is lost to the depleting defect itself. Obviously, the tip will not interact with the defect by simply summing all of the contributions equally, but this indicates that we should only make these assignments based on atomic resolution images. As discussed in

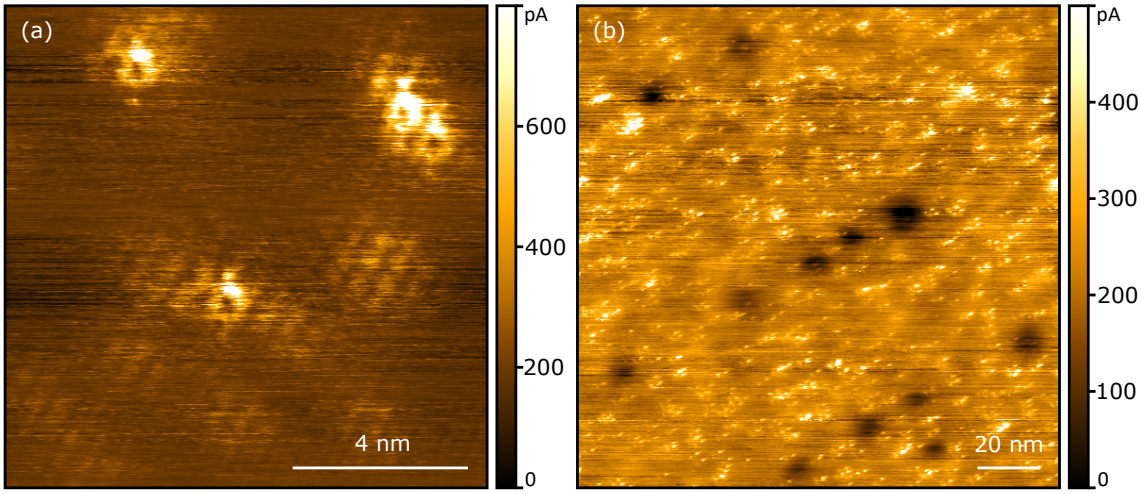

Figure 5.4: Current channel cAFM images of augmenting *(a)* and depleting *(b)* diffuse defects on MoS_2, shown alongside localised defects that are not properly resolved, but clearly have a smaller radius of influence.

Section 3.2.4, in the work of Rosenberger *et al.* [22], the defects observed all appear as augmenting defects in cAFM images, but the resolution is not high enough to resolve individual atoms.

Localised defects constitute the majority of defects in our mechanically exfoliated samples. Based on the observations by Barja *et al.* [9] and theoretical works outlined in Section 3.2.4 the most likely attribution seems to be oxygen substitutions. They also indicate that the augmenting site-specific defects are likely to be caused by the oxygen substitution lying in the bottom chalcogen layer, whilst those on the top layer are depleting, which corresponds to the majority of the defects observed in this work. As our samples have been exposed to air there is very little chance of any vacancies not being converted into oxygen substitutions. Our samples are stored in a vacuum environment, but many of the measurements, such as the cAFM measurements, were taken in ambient conditions.

We also observe diffuse defects which extend over a wider area in MoS_2. They are frequently attributed to Transition Metal Substitutions in studies using cAFM [24, 104]. As shown in Figure 5.4 both augmenting and depleting diffuse defects have been observed on MoS_2, though considering the broad array of transition metals

that could be substituted into MoS_2, this is not surprising.

5.4 WSe_2 and WS_2

Diffuse defects occur most frequently on WSe_2 and an example is shown in Figure 5.5. We rule out charged defects because a characteristic feature of these defects is their band bending as described in Section 3.2.4. Figure 5.5b shows a diffuse depleting defect in WSe_2 imaged at a bias voltage of -1 V and the same defect is observed in Figure 5.5c, imaged with a bias of 1 V. If this was a charged defect, Figure 5.5c would be augmenting, but it is in fact depleting, ruling out this assignment. The diffuse defect has a width of approximately 5 nm, which is similar to that of the diffuse defects on MoS_2.

The smaller defects in Figure 5.5c seem to be localised defects. Their sudden appearance does not seem to be caused by the change in bias, but rather an increase in resolution after a tip change, evidenced by other images taken at 1 V bias which do not reveal these defects. Some vague sign of the defects could be argued in Figure 5.5b in fact. The localised defects appear to be both augmenting and depleting, but they are not properly resolved.

Localised defects are also much more prevalent than diffuse defects in WSe_2. Figure 5.5a shows localised depleting defects on WSe_2 which look similar to those on MoS_2. The ratio of augmenting and depleting localised defects favours depleting defects on MoS_2, but on WSe_2 this seems to be more acute. This could be caused by faster degradation of the TMD in atmospheric conditions, leading to the upper face of the TMD being favoured.

It is expected that WSe_2 and MoS_2 should have similar vacancy formation energies, but that WSe_2 is more susceptible to oxygen adsorbing onto the surface based on the literature discussed in Section 3.2.4. This could be responsible for the increase in defects on WSe_2, especially the number of depleting defects as, naïvely, it seems that the top layer of chalcogens would be more exposed.

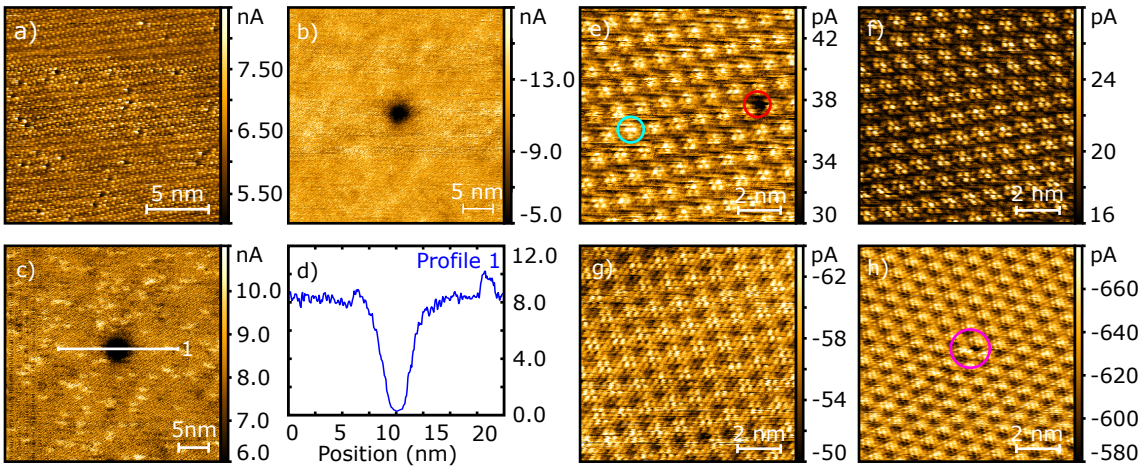

Figure 5.5: Current channel cAFM images of WSe_2 *(a-d)* and WS_2 *(e-h)*. An image taken with a 0.5 V bias voltage shows that the localised defects WSe_2 are predominantly depleting and very frequent *(a)*. A diffuse defect on WSe_2 is imaged at -1 V *(b)* and 1V *(c)*, showing that it is consistently depleting. The profile in *(c)* is shown in *(d)*, showing that the influence of the defect extends over a diameter of ~ 5 nm. Examples of both augmenting and depleting localised defects on WS_2 can be made out through the Moiré pattern at 0.5 V bias. Further images show the Moiré pattern at 0.5 V *(f)* and -1 V *(g)*bias, showing the broad range of bias voltages that are affected. The Moiré pattern can obscure the nature of defects, preventing reliable information *(h)*.

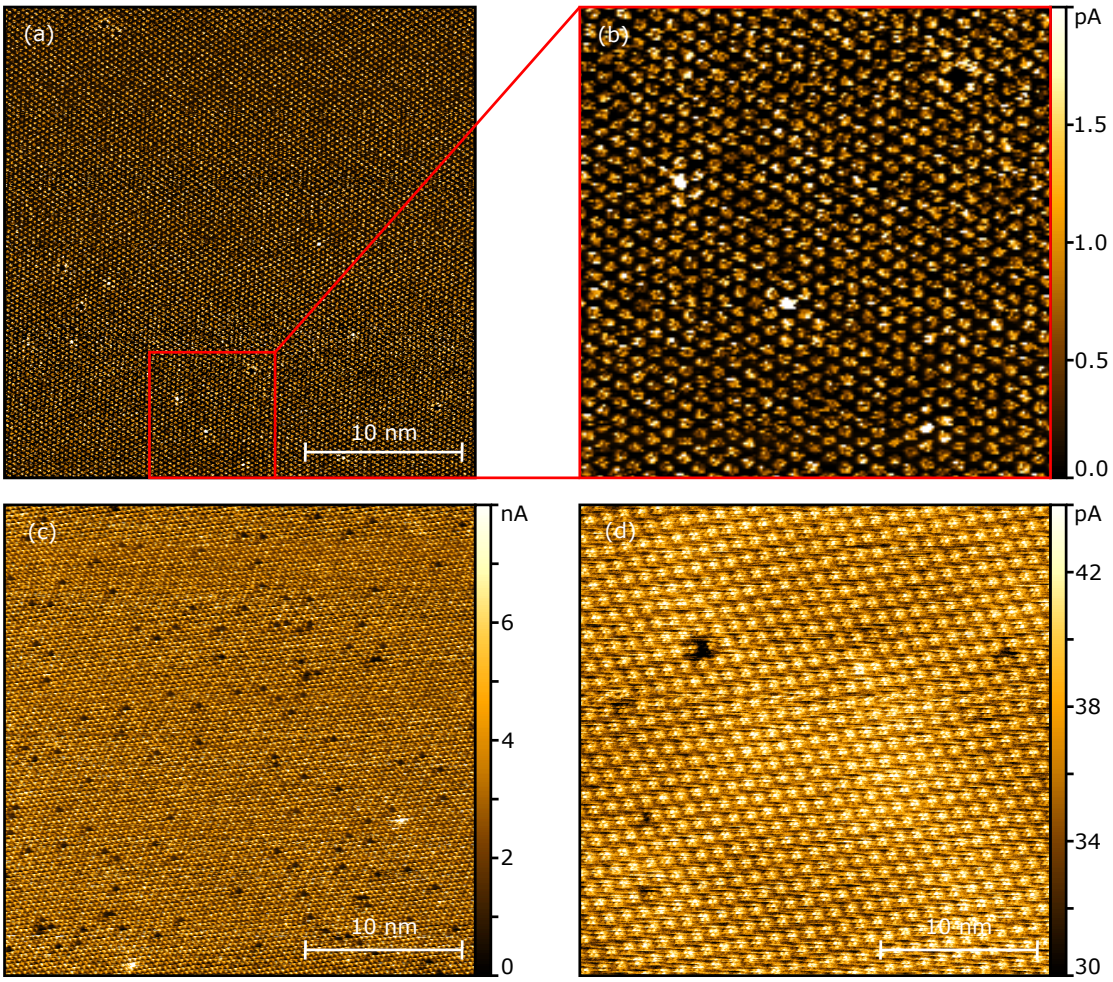

Figure 5.6: 30 nm by 30 nm current channel images of MoS_2 *(a)*, WSe_2 *(c)* and WS_2 *(d)* taken at a bias voltage of 0.5 V. A close up of the MoS_2 image *(b)* is provided to highlight the features. The density of defects is significantly higher in the WSe_2 image and the WS_2 contains much fewer defects and a strong Moiré pattern.

Such an argument also makes a prediction for WS_2: that it will have fewer chalcogen vacancies and this seems to be supported by our data. Figure 5.5e-h show images taken on WS_2. They are all dominated by Moiré patterns that obscure the defects. We can observe both augmenting and depleting localised defects on WS_2, but it is difficult to gather any more information about them. The strength of a Moiré pattern can be very bias-dependent on other TMD samples, but here we show that at 0.5 V (Figure 5.5f) and 1 V (Figure 5.5g) the Moiré pattern was dominant and this is representative of the work on WS_2; the data was obscured between -1 and 1 V.

By considering images taken across the three crystals we can calculate the density of the localised defects. One cannot create a statistically significant sample of the defect density from SPM images in a reasonable amount of time, so here the number of defects in the 30 nm by 30 nm images in Figure 5.6 are counted in order to give an impression more than a reliable figure. The density of localised defects are 1.4×10^{13}, 1.6×10^{12} and 6.7×10^{11} defects per cm^2 for WSe_2, MoS_2 and WS_2 respectively. One can see that there is a clear order of magnitude difference between WSe_2 and MoS_2 and at least twice as many defects in MoS_2 than in WS_2, in agreement with the theoretical works discussed earlier.

5.5 Variation in imaging

In the images displayed above we have presented the results based on the features which seem most consistent. The depleting localised defects in MoS_2 and WSe_2 displayed in Figures 5.2, 5.3, 5.5 and 5.6 show a great deal of similarities from four measurement sessions and across two materials. They also bear a great resemblance to images shown in Chapter 6. However, the images are not completely consistent.

In some images a sort of 'needle-like' resolution has been observed on WSe_2 and MoS_2 samples which makes it difficult to interpret the images. The signal on each site is incredibly sensitive and it is difficult to distinguish between defects and

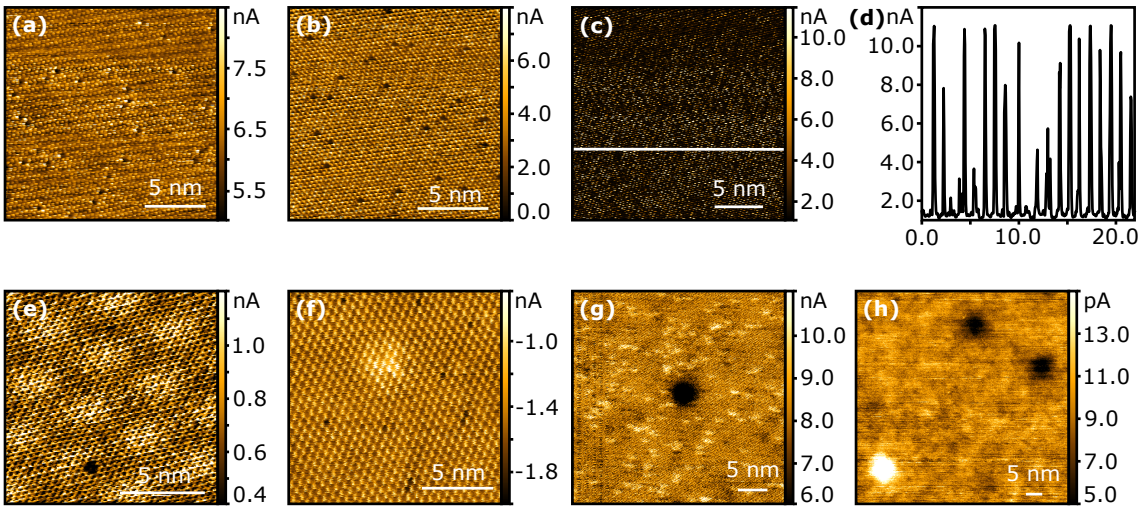

Figure 5.7: As observed in Figures 5.5 and 5.6, two images of the depleting localised defects in two WSe_2 samples *(a-b)* look similar and are comparable to images taken on MoS_2. In some images, the signal from each atom is very strong and sensitive to variation leading to difficult to interpret images *(c)* and 'needle-like' profiles *(d)*. Moiré patterns can feature heavily *(e)* and in some cases, either the atoms are depleting or the augmentation in current is observed between the atoms in bridges as well. In other images, *(f)* the signal from defects lies between the augmenting signal which one would normally attribute to the atoms. Diffuse defects can be observed as both augmenting and depleting, but there is often less variation in their appearance *(g-h)*. These images are taken on WSe_2 at bias voltages 0.5 V *(a-e, h)*, −0.8 V (f), 1 V (g).

noise. An example of WSe_2 is shown in Figure 5.7c-d where the profile shows the needle-like spikes that are observed in the current channel. Other observations, shown in Figure 5.7, include a lattice of depleting sites, which could indicate that the contrast is inverted or that the area in between the atoms is producing a similar current. Defects are also seen in between the augmenting regions which would typically be assigned to atoms. This could be assigned as an observation of defects in the transition metals but, given the number of defects in the image and the fact that this has occurred once, it is much more likely that this is a tip artefact.

Diffuse defects tend to be more consistent. They have been observed as both augmenting and depleting, but in Figure 5.7 one can see both augmenting and depleting defects in the same scan. This difference was consistent across a range of bias voltages in multiple images, so it is unlikely that this is a result of a tip artefact.

In addition to this variation in seeing features which we commonly observe, we also encounter defects with more unusual behaviours. Some defects show behaviour that is bias-dependent. These changes can be reversible, or irreversible such as the unusually clear images of localised defects on WS_2 shown in Figure 5.8a-d. In these images, some defects appear when the bias voltage travels below a threshold and then the defects begin to behave like localised depleting defects after being imaged at -1.1 V. This could be due to a tip change induced by the high bias voltage.

In Figure 5.8e-f a diffuse depleting defect seems to be overlaid by the Moiré pattern that dominates the contrast in the image when the bias is reduced from -0.2 V to -0.6 V.

Due to the low resolution the augmenting defect with a depleting halo shown in Figure 5.8g may simply be a diffuse depleting defect very close to a more localised augmenting defect. Other defects observed in this measurement were augmenting defects with a relatively small radius, as is common when atomic resolution is not achieved. Similarly, Figure 5.8h may be another cluster of defects. The well resolved, smaller features of the Moiré pattern confuses this further though without any defects in this region this could be an instance of 'lattice resolution' discussed

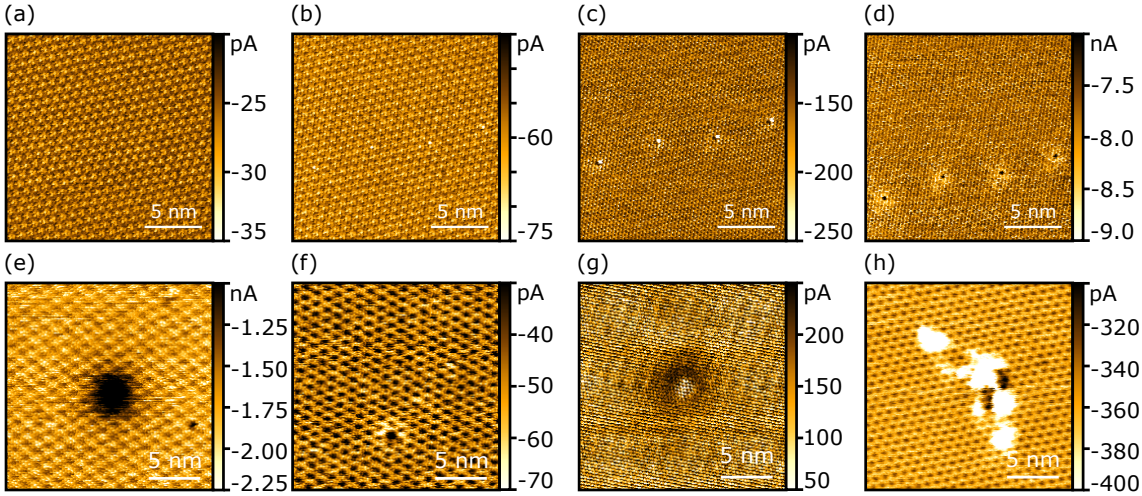

Figure 5.8: A localised bias dependent defect on WS_2 is invisible at -0.4 V bias *(a)* and above, but appears as an augmenting defect at -0.6 V and then increases in intensity at -0.8 V *(c)*. At -1.1 V *(d)* the defect becomes depleting and then behaves as a localised depleting defect. A diffuse defect on WS_2 seems to shrink as the bias reduces from -0.2 V *(e)* to -0.6 V *(f)*, perhaps due to the strong moiré pattern. A defect with a depleting halo around an augmenting core was observed on MoS_2 at 0.5 V bias *(g)* and a mix of augmentation and depletion is imaged on WS_2 at -1 V *(h)* despite finer features observed in the lattice/Moiré pattern.

in Section 2.5.

5.6 Conclusions

This work demonstrates that cAFM can be used to survey the defects in TMDs with atomic resolution, allowing for the density of particular defect types to be considered rather than simply counting the density of defects in general. This is an important step towards the realisation of TMDs as impactful materials. However an identifying tag, such as those discussed at the beginning of the chapter, would be unusable if it had to be read via SPM. In order to realise an identifying tag based on the defects in a sample it would likely be measured using the optical properties of TMDs and the density of defects which are common will vary on length scales beneath the resolution of optical techniques.

In order to create a successful tag one would need to engineer a sample with defects that significantly impact the optical signal and vary on length scales longer than those we observe here. Single photon emitters are good candidates because one defect that acts as a single photon emitter stands out against the rest of the emission from the sample. To create engineered devices we must understand how defects can be modified and created in TMDs.

Chapter 6

Results: creation of defects in transition metal dichalcogenide monolayers

The use of conductive atomic force microscopy (cAFM) to study defects in transition metal dichalcogenide (TMD) monolayers with atomic resolution was demonstrated in Chapter 5. Here we expand on that work by creating new defects via annealing and exposure to N_2 plasma. In order to understand how defects can be used to create unique tags accessible by optical methods I will now detail the progress made towards identifying correlations between the defects observed with cAFM and the optical response in photoluminescence (PL) measurements.

6.1 Studying defect formation due to annealing

In Figure 6.1a one can see the effect of the substrate on the PL signal. The highly oriented pyrolytic graphite (HOPG) substrate leads to a slight reduction in the signal and a slight blue shift, but improving the contact with the 'Nano-squeegie' technique detailed in Section 4.3.5 leads to a further reduction of over two orders of magnitude and a more significant redshift. Because the substrate is conductive the

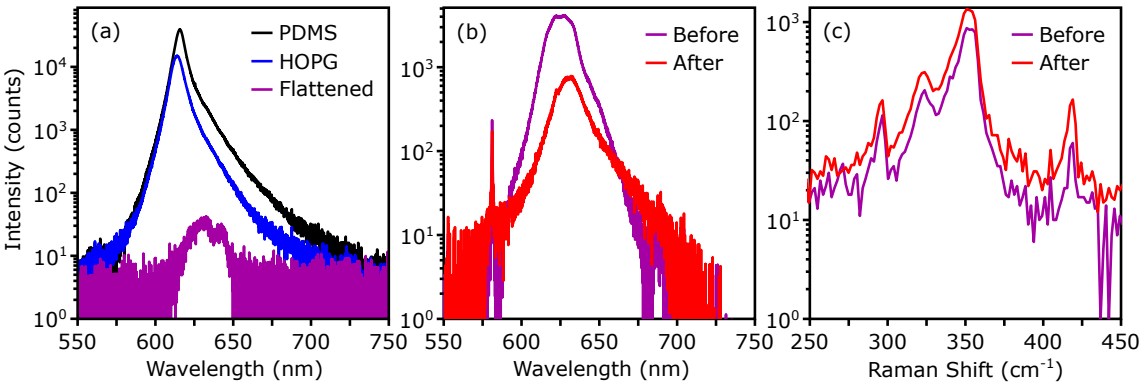

Figure 6.1: Changes to the intensity of the photoluminescence signal of WS_2 measured over 20 s due to the substrate can be clearly seen *(a)* during fabrication. Here 'Flattened' refers to after the use of the 'nano-squeegie' technique on HOPG. Annealing the sample at up to 450 degrees led to a further reduction in intensity *(b)*. Spectra were taken before and after using 100 times more incident power in order to increase the signal. Despite this the Raman signal increased *(c)*.

carriers may decay inside the HOPG rather than the TMD, leading to the loss of carriers without the emission of a photon; non-radiative recombination. The changes in the peak wavelength of the PL emission could be due to changes in strain or due to changes in the population of excitons. A good connection to a metallic substrate should neutralise the TMD because it is connected to a much larger reservoir of charge.

In order to not overcomplicate the experiment, the first attempt to introduce defects into TMDs was carried out by annealing samples in a UHV environment. With the assistance of my colleague, Alessio Quadrelli, a sample of WS_2 on HOPG was loaded into X-ray Photoelectron Spectroscopy (XPS) apparatus. The chamber was pumped out and by measuring the energy of electrons ejected from the sample when X-rays are incident information about the elemental composition and bonding can be inferred. If the thermal energy is great enough one would expect defects to begin forming due to the introduction of additional thermal energy with a preference for defects with the lowest formation energy.

The temperature of the chamber was increased from room temperature to 450 K whilst carrying out XPS measurements on a bulk WS_2 flake. During this process,

a clear shift in the energy of the peaks representing the Sulfur (S) 2p and Tungsten (W) 4f orbitals was seen towards lower binding energies relative to the C 1s peak as shown in Figure 6.2.

The intensity of the C 1s peak decreases, whilst the small bump at $\sim$ 290 eV remains the same size. This small bump represents aromaticity, indicating that little change has occurred to the HOPG substrate, but the decrease in the main peak indicates a decrease in some other carbon. Strangely the peaks relating to the TMD both increase in intensity, possible mechanisms will be discussed later.

cAFM measurements following the XPS measurements reveal that a layer of contaminants now covers the surface 6.2. It is possible that these contaminants were due to the tapes and PDMS used in the transfer and were then distributed evenly across the sample during annealing, reducing the size of the C 1s peak. Desorption of polymer material from the surface could have also contributed to the reduction, as it would reduce just the amount of carbon on the surface that does not have an aromatic component. The increase in the TMD peaks can similarly be explained by the removal of a capping layer of contamination via either of the processes described.

The cAFM tip initially engaged on a different bulk flake. By measuring at high bias voltages a signal could be detected and defects were observed, though the tip was brushing aside contaminants, which led to unstable measurements. The defects were mostly diffuse and depleting; they were notably different from smaller augmenting defects which could also be resolved. Many of the diffuse depleting defects appear to be surrounded by a small augmenting halo.

Returning to the optical spectroscopy results in Figure 6.1 we can see that annealing led to a further reduction in the signal. Of course it is possible for these signals to vary substatially due to focus and other factors, but a change of an order of magnitude is too great a factor to be accounted for in this way. The reduction in intensity would align with the idea that defects had been created as they can increase non-radiative recombination. The slight increase in the intensity of the Raman peaks is peculiar because the peak due to HOPG (not pictured) remains

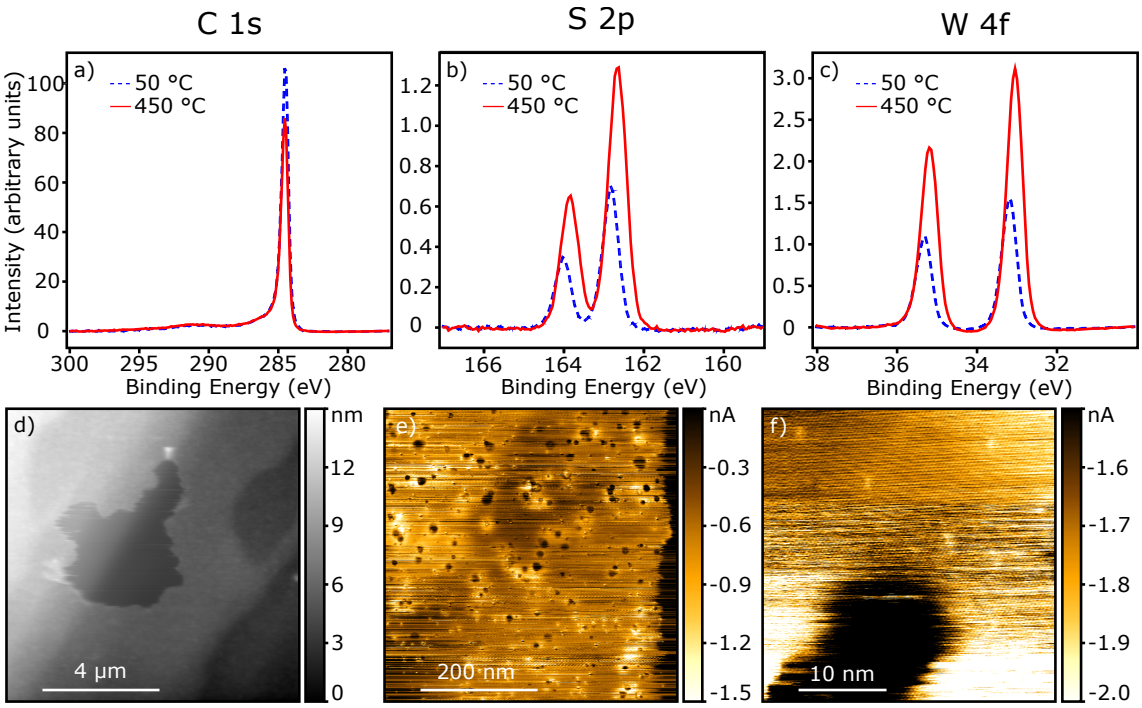

Figure 6.2: As WS_2 is annealed in a UHV environment XPS measurements were made. The S 2p *(b)* and W 4f *(c)* peaks in the XPS signal shift to lower energies relative to the C 1s peak *(a)*. Topographic data collected during conductive atomic force microscopy showed that a layer of contamination covered the sample *(d)*. At a bias voltage of -1 V the current channel showed lots of defects with a large radius of influence *(e)*, confirmed by the presence of smaller features that were resolved by the tip *(f)*

approximately the same height. Knowing that there were polymers on the TMD flake, the annealing could have further spread out the contaminants, but it is difficult to determine if this is the case. Clearly, minimising contaminants would minimise uncertainty on many aspects of the results.

6.2 Minimising Contamination

Following the discovery of contamination, the efforts of the experiment were directed towards ensuring the mechanically exfoliated samples were as clean as possible. Highly oriented graphite (HOPG) substrates were cleaved following transfer in order to remove the HOPG coated with conductive silver paint that held them in place and had previously acted as a conductive link to the sample plate. Samples were now held in place by crushing the opposite end of the substrate into the sample plate with a metallic strip fastened by screws. The substrate was removed from the sample plate when they were placed in vacuum environments in order to minimize the presence of contaminants from the sample plate.

Because samples had come out of the cryostat with a layer of contamination, which could be observed in AFM images such as Figure 6.3, the procedure for cryostat use was refined to ensure that the chamber was properly evacuated before cooling and a cold shield was reinstated above the sample to further protect it.

Further experiments into the introduction of defects were carried out by exposing TMD monolayers to a N_2 plasma. A plasma contains ionized material that instigates chemical reactions in the surface. By exposing the surface for a very small amount of time it is hoped that defects will form, but the samples will not be changed beyond recognition as a WSe_2 flake. The effect of this change on the cleanliness of the samples is unknown as plasma cleaners are frequently used to clean substrates, but at the short exposure times used here, the exact effect is more uncertain. Further to this, it is possible that the plasma could facilitate chemical reactions between the polymer and the TMD. However, as the sample has been exposed to the ambient

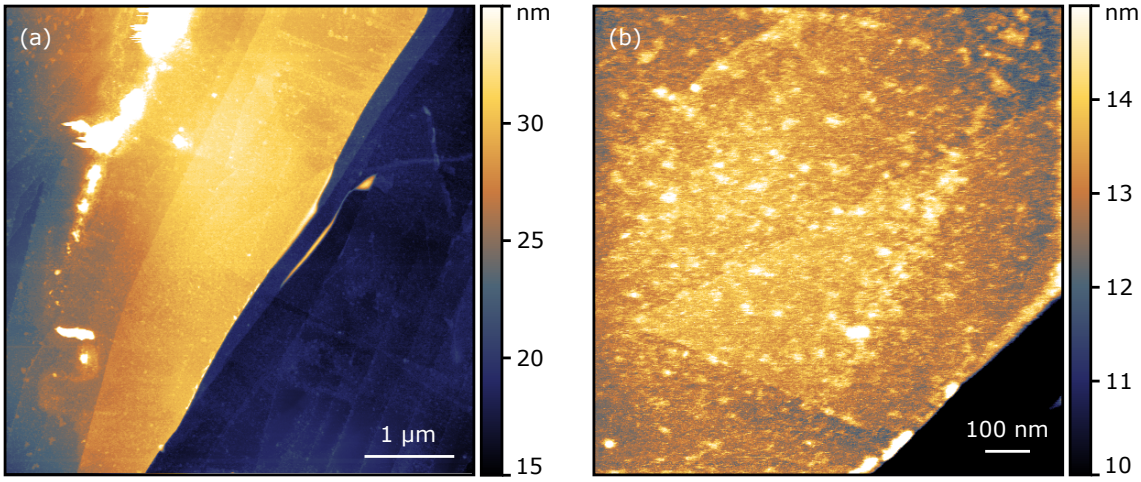

Figure 6.3: Off-resonance AFM images of contamination on an HOPG substrate with a WS_2 monolayer. In a larger image *(a)*, the ridge of material created by the 'nano-squeegie' technique is clearly visible as the white stripe in the top left, but the surface and WS_2 flake are now covered in contamination. In a smaller image *(b)* the rough, clumped nature of the contamination can be observed in greater detail.

environment the total exclusion of contaminants without a more aggressive approach is infeasible.

6.3 MoS_2 on HOPG and hBN

The PL signal of TMDs on HOPG was measured to be significantly lower than measurements with identical parameters on PDMS. This effect is likely due to the loss of carriers to the conductive substrate. Carriers may lose energy by moving into the band structure of the HOPG layer where there is no band gap to prevent the loss of energy by non-radiative means. Figure 6.4b shows the effect of various substrates on the photoluminescence of MoS_2.

The conductive substrate was a necessity for cAFM measurements, but if the same flake could be draped such that it also lay on an insulator then a higher PL signal could be measured. This is important because the signal of TMDs reduced during exposure to plasma as defects will create alternative non-radiative decay paths and generally disrupt the idealised lattice. Combined with a conductive

substrate the signal from plasma irradiated MoS_2 on HOPG was very small, leading to great uncertainty in the measurement and the possibility that smaller peaks would be indiscernible from noise.

Hexagonal boron nitride (hBN) is another Van der Waals layered material, but it possesses insulating properties. It is commonly used to isolate two dimensional samples from the environment around them [154]. By fabricating a relatively thin hBN sample through mechanical exfoliation I was able to build a Van der Waals heterostructure by simply transferring the MoS_2 flake on top of the hBN flake, shown in Figure 6.4a.

In cryogenic PL measurements shown in Figure 6.4 there are three distinct peaks, though they are broad and likely contain contributions from multiple states at such low temperatures. The peak above 1.9 eV increases linearly as a function of the incident power, whereas the peaks at lower energies are observed to have a much weaker power dependence. The population of excitons bound to defects should saturate at a lower intensity because the number of defects which excitons can bind to is much smaller than the number of carriers in the sample. In order to form an exciton an electron must interact with a hole, and both are plentiful, but to form a defect-bound exciton an existing exciton must then find a defect which is not already bound to an exciton. As a result, the probability of defect-bound excitons forming drops at relatively low powers as the probability of the exciton finding an unbound defect during its lifetime becomes vanishingly small. Such restrictions do not apply to unbound excitons if there are significant populations of both carriers, so on this basis, it is likely that the peaks at lower energies are created by defect-bound excitons and the peak above 1.9 eV, the reported bandgap of monolayer MoS_2, is likely due to unbound excitons. This assignment seems reasonable because one would expect defect-bound excitons to have a higher binding energy; resulting in the emission of photons with less energy.

A section of the MoS_2 protruded over the edge, onto the HOPG substrate enabling the collection of cAFM data, but due to the low PL signal, measurements

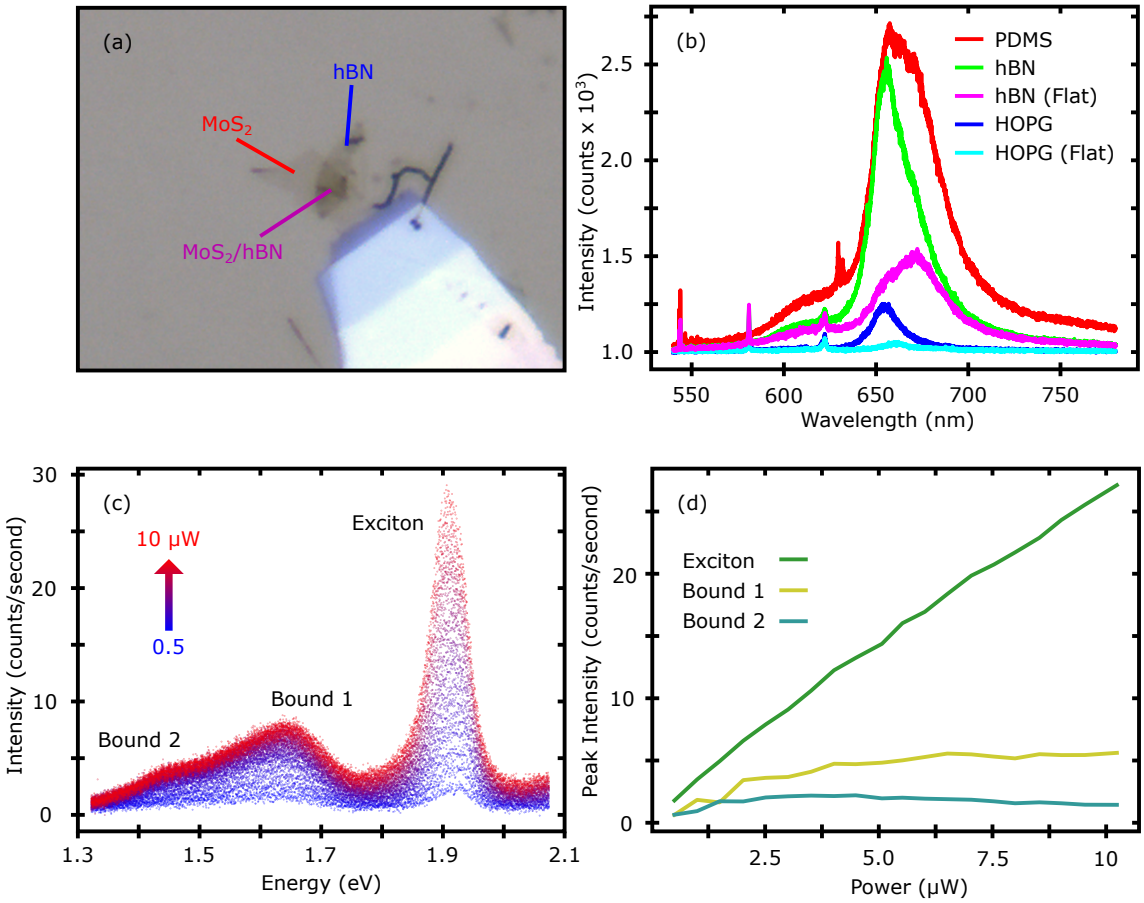

Figure 6.4: An optical microscope image shows an MoS_2 flake lying over a multi-layer hBN flake on HOPG *(a)*. Photoluminescence spectra were collected over 20 s from this sample in a variety of environments at room temperature as the sample was fabricated *(b)*. Further spectra were taken on the MoS_2 on hBN at 8 K *(c)* where three broad peaks can be seen. By fitting the peaks to Gaussians it becomes clear that the peaks at lower energies do not grow at the same rate as the higher energy peak when the power is increased. *(d)*.

were not taken. WSe_2 was selected as the material for future samples. The W containing TMDs have significantly higher PL signals than MoS_2, as discussed in Section 3.2. The problems with Moiré patterns observed on WS_2 led us to select WSe_2 in particular.

6.4 WSe_2 on HOPG and hBN

Tests were carried out on three WSe_2 samples on an HOPG substrate. The samples were exposed to 10, 30 and 60 seconds of nitrogen plasma and room temperature PL spectra were taken before and after. This provides preliminary information about the rate at which the samples are damaged.

The faint lines in Figure 6.5b represent the three samples prior to plasma exposure. They show relatively similar signals, but the PL signal of samples falls during exposure, leading to a total disappearance of the signal in the case of the sample exposed for 60 s. Peculiarly, the sample exposed for 10 s seems to have suffered a greater change in signal than the sample exposed for 30 s. This may be due to difficulties in keeping the conditions in the plasma reactor consistent, but repeat measurements would be needed to eliminate human error such as mislabelling samples.

Off-resonance atomic force microscopy topographic images show a significant amount of distortion characteristic of loose material on the surface. Repetitive imaging of the same region quickly cleared the region of this material to reveal that the monolayer flake had disappeared. This section of the crystal seems to have completely disintegrated.

To simplify fabrication, three WSe_2 flakes were used in the creation of the next sample. One was placed on HOPG and the other two were placed on hBN so that there was no need to drape a flake off the hBN.

Measurements with cAFM were taken before and after exposure with N_2 plasma and they are shown in Figure 6.6. Before plasma exposure localised depleting defects

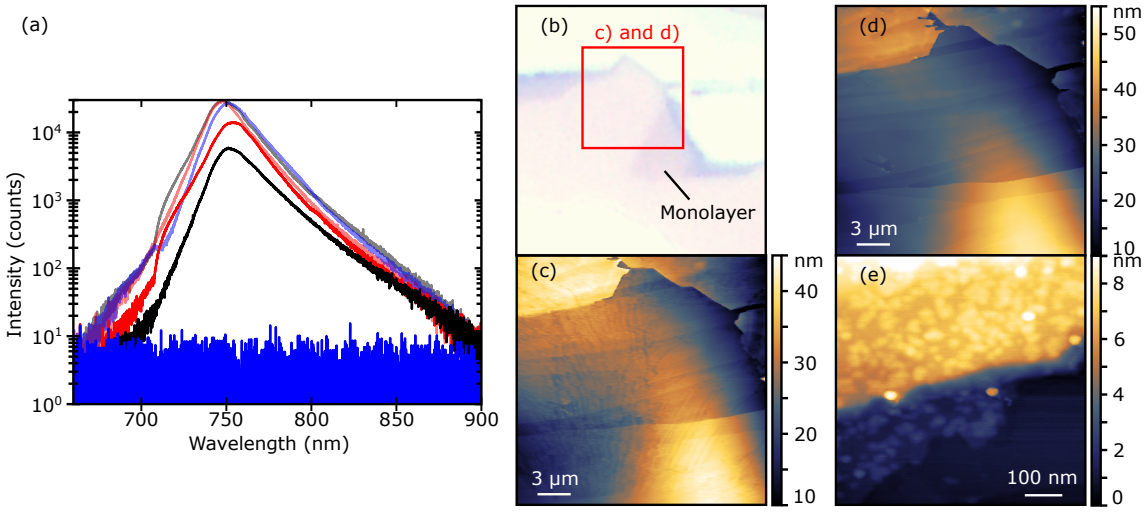

Figure 6.5: In PL spectra using a measurement time of 20 s *(a)* the reduction in signal due to plasma exposure can be seen for three samples on HOPG. The faint lines show the signal before exposure and the solid lines show the same samples after 10 s *(black)*, 30 s *(red)* and 60 s *(blue)* of plasma exposure. An optical microscope image of the WSe_2 flake which was the source of the black spectra in panel (a) before plasma exposure *(b)*. The region in the red box was imaged with off-resonance AFM after 60 of plasma exposure, showing excessive amounts of material present on the surface *(c)* and after multiple scans the material clears to reveal the absence of the flake *(d)*. After moving the imaging region to find a thin section of WSe_2 one can see that it is now textured and rough *(e)*.

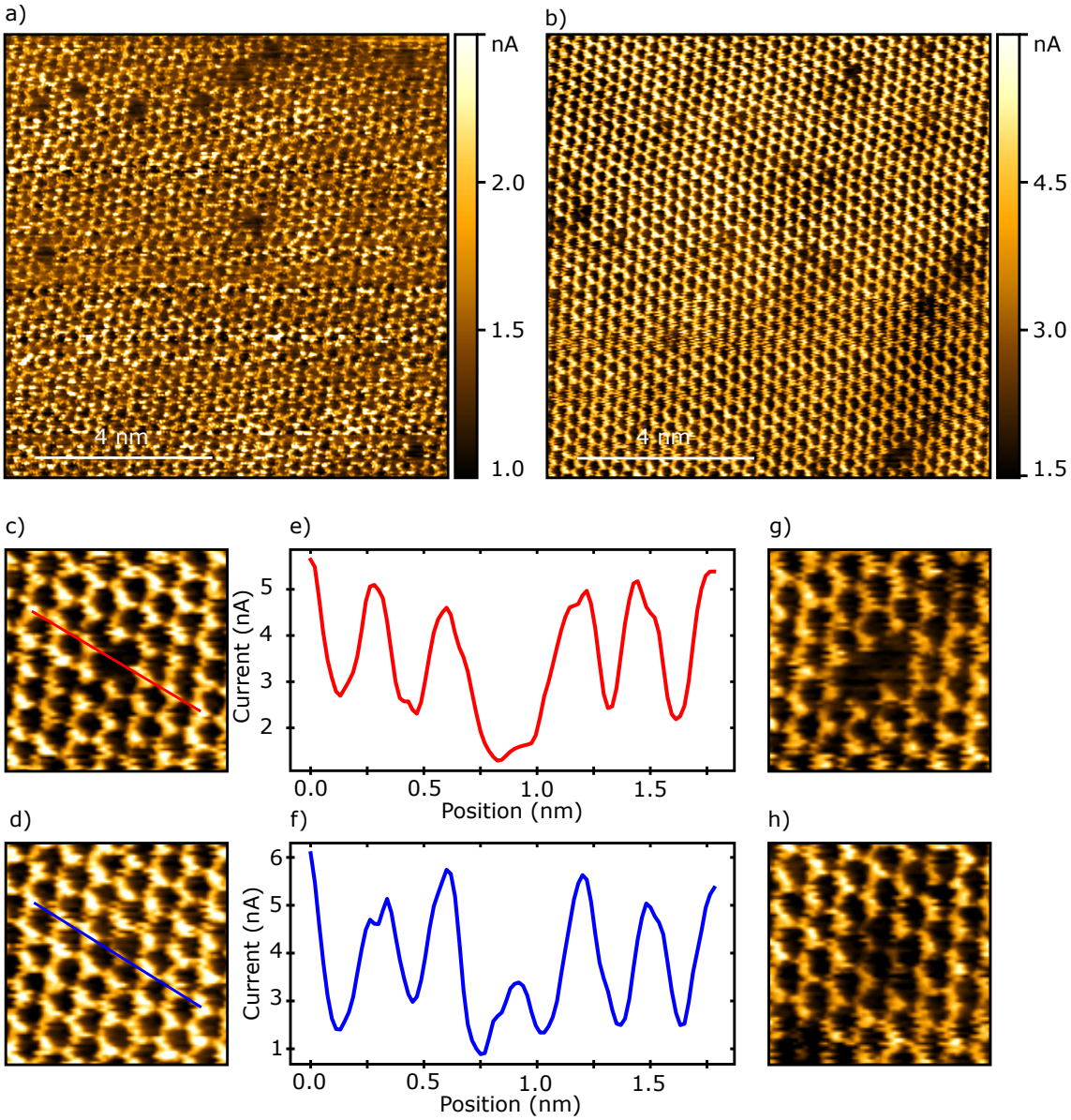

Figure 6.6: Current channel images taken at a bias voltage of 1 V before *(a)* and after *(b)* 10s of exposure to N_2 plasma. Before plasma exposure, many depleting defects are seen, as is common on WSe_2, but afterwards, the number of defects increases and a different type of defect is present. A close-up image of a depleting defect is shown in *(c)*, which can be compared to the new 'faint' defects such as the close-up in *(d)*. Profiles taken across the defects (*e* and *f* respectively) show that there is a signal at the faint sites, but it is very weak, whereas the depleting defects show no signal at the defect site. In addition, both these defects can now be seen in pairs (*g* and *h* respectively), a behaviour not seen elsewhere.

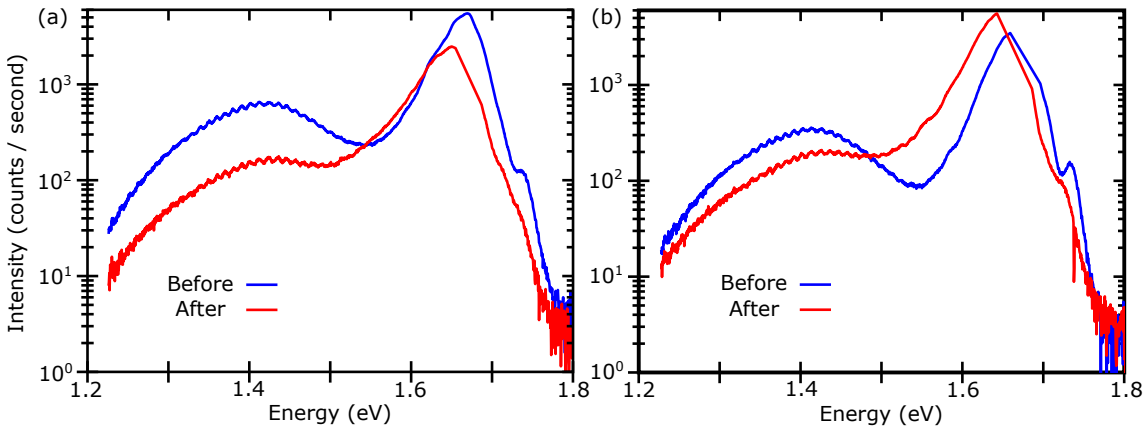

Figure 6.7: Cryogenic PL measurements from two additional WSe_2 flakes placed on hBN (*(a) and (b)*) from the same sample as the cAFM measurements in Figure 6.6. The high energy peak moves to lower energies, but it increases in one sample and decreases in the other. The other, lower energy peak, decreases in intensity for both flakes.

were observed as expected. However, after exposure to 10s of N_2 plasma fainter defects were observed in addition to the formative defects. Profiles taken across the defects confirm a small signal on the sites of these defects, relative to the apparent absence of the standard localised defects in the scan. If we are to assign the formative localised depleting defects to be oxygen substitutions, we can perhaps make an even more tentative assignment that the 'faint' defects represent nitrogen substitutions because this is the element in the plasma. As discussed, it is difficult to determine that some form of contaminant is not responsible for these defects instead of the plasma. To be sure of the composition the sample would need to be studied with an XPS to see if there was a significant increase in the nitrogen signal from the sample after exposure.

Interestingly, in addition to the presence of the new faint defects both faint and standard localised depleting defects are now observed in pairs, where two neighbouring sites are defective. This has not been observed in any other sample.

Cryogenic PL measurements, shown in Figure 6.7, do not resolve peaks thin enough to represent a single state in this sample, instead, the peak between 1.6 and 1.7 eV represents a combination of exciton states at similar energies. Again, less

intense peaks that are possibly caused by defect-bound excitons are present at lower energies. There is a significant movement in the position of the peak towards lower energies after the same 10s of plasma exposure, indicating a reduction in the band gap.

Interestingly, the peak previously assigned as defect-bound excitons is reduced in the spectrum taken after plasma exposure. This could be because this is not the cause of the peaks, or because damage to the sample, in general, has reduced the intensity of all PL emission due to a loss of coherence. For instance the introduction of deep trap states would lead to non-radiative recombination. However, though there is a significant reduction in the intensity of the higher energy peak in one of the spectra there is an increase in the height of this peak in the other sample.

The disagreement between the two flakes was concerning. Both flakes had undergone the same process, so the different outcome implies that a factor is not being properly accounted for. The hBN substrates were a significant source of concern. The presence of bubbles in the flakes could be observed and the PL signals for one of the flakes was observed at a spot where the contact was better. There was a significantly lower signal in regions of worse contact and the hBN layer was providing unnecessary variation in the flakes that was difficult to account for with confidence.

In another sample of WSe_2 on hBN on HOPG shown in Figure 6.8 changes in the bubbles between the hBN and the substrate can be seen as the plasma exposure progressed. The results of room temperature optical spectroscopy studies such as this (Figure 6.8f-g) show a significant reduction in the signal from flakes, but this is simply consistent with the damage the flakes are sustaining. Cryogenic measurements are likely to be necessary in order to extract more information.

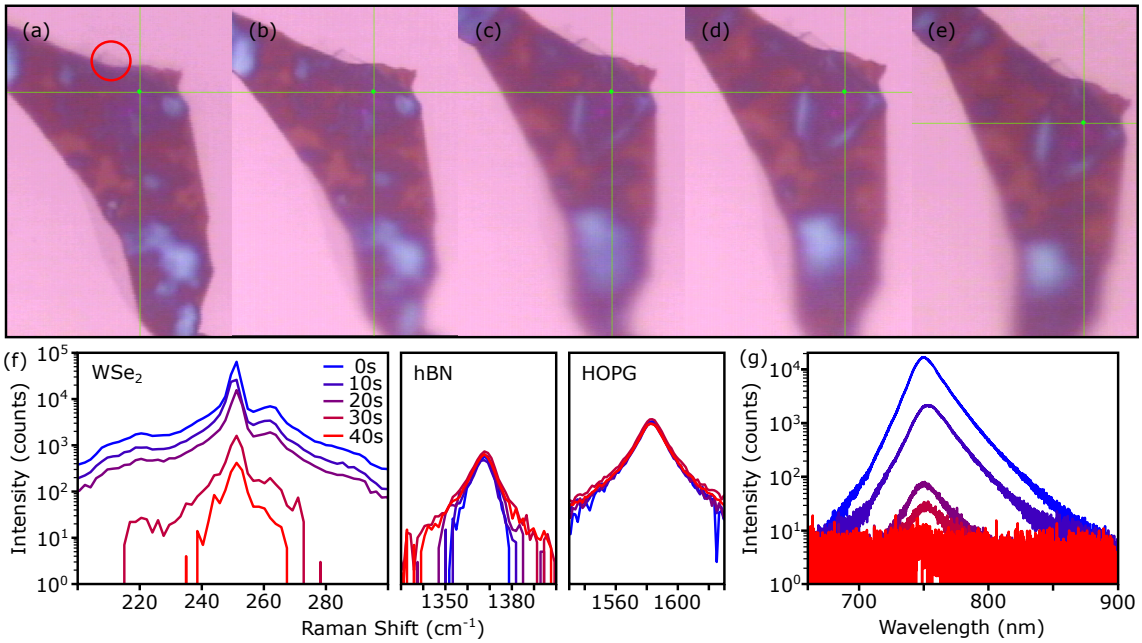

Figure 6.8: Optical microscope images of a sample taken to record the position of the laser during optical spectroscopy measurements after *(a)* 0s, *(b)* 10s, *(c)* 20s, *(d)* 30s and *(e)* 40s of plasma exposure. The thick hBN between the WSe_2 sample and the HOPG substrate can be clearly seen, but the sample itself is difficult to observe, save for a small section projecting off the hBN and onto the substrate (red circle). The Raman spectra, taken using a measurement time of 60 s *(f)* show a significant decrease in the intensity of the peaks of WSe_2, but little change in peak position as the exposure progressed. There was relatively little change in the HOPG and hBN related peaks. The PL spectra, taken over 20 s, show a similar loss of signal, but little else can be made out from such broad peaks.

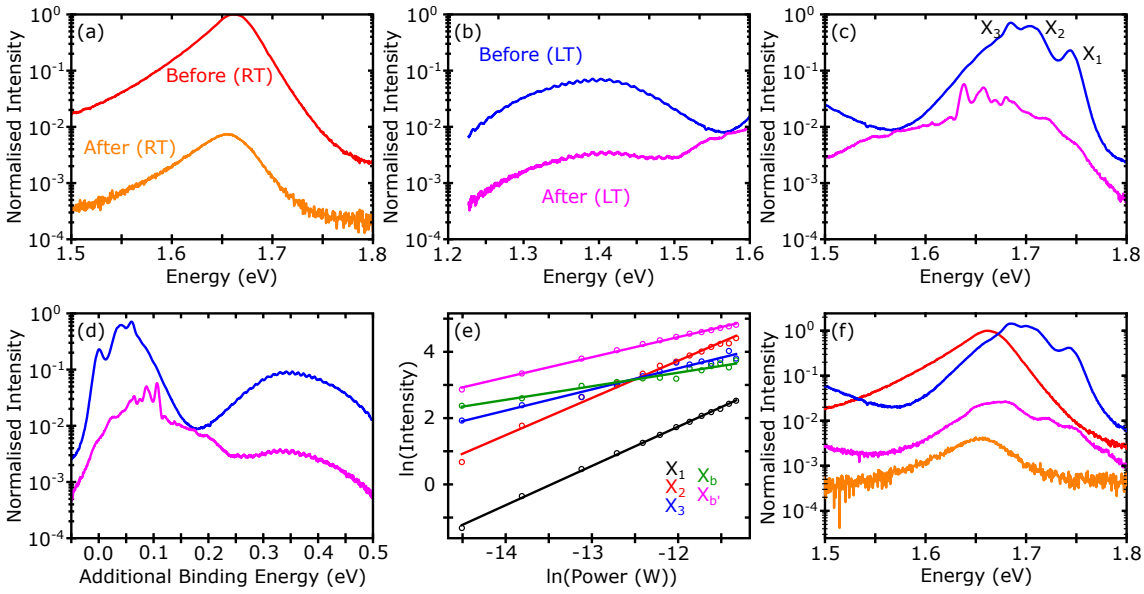

Figure 6.9: Room temperature PL (RT) using the Isolab PL equipment before and after 20s of plasma exposure *(a)*. All peaks in this figure are normalised to the height of the room temperature peak before exposure. A broad peak $X_{b'}$ was observed at low energies in cryogenic measurements (LT) but then decreased both in intensity and as a proportion of the signal after exposure *(b)*. At higher energies three sharp peaks X_1, X_2, X_3 were observed protruding from a broader peak X_b in the spectrum from before exposure *(c)*. After exposure the sharp protrusions appear at lower energies, but the signal at the initial positions is still observed. Taking X_1 to be the free exciton, we can plot the same data as a function of the additional binding energy relative to that peak *(d)*. Fitting the peaks allows the exponent of the power dependence to be calculated from the gradient of the 'log-log' plot *(e)*. A similar spectrum is acquired from a section of the flake that was torn away during transfer, but the features are not so well defined *(f)*. All spectra were collected at an incident power of ~ 60 μW, with the obvious exception of (e).

6.5 WSe_2 on Si

In order to acquire PL spectra from WSe_2 before and after plasma exposure with a greater degree of confidence the next sample was fabricated on a SiO_2 substrate. The substrate was cleaned prior to exfoliation by sonication in acetone and then in isopropyl alcohol and excess solvent was removed from the samples with compressed nitrogen gas. During transfer onto the Si substrate, the sample ripped and the other part of the sample was also transferred to ensure that a usable sample was present. A PL signal could be acquired from both samples so they were both studied throughout the course of the experiment.

The sample was then exposed to nitrogen plasma for 10s twice whilst the signal was monitored before and after each exposure with room temperature PL and Raman measurements. The reduction in the signal due to the damage from the plasma proved concerning after two exposures as the signal needed to be significant enough that reliable data could be acquired. The cryogenic PL system was also used to collect spectra displayed in Figure 6.9 before and after plasma exposure at room temperature and a cryogenic temperatures (~ 9 K).

In the room temperature measurements the intensity dropped by over 2 orders of magnitude after 20s of exposure. Before exposure, there were clear peaks in the cryogenic PL spectrum, labelled X_1, X_2 and X_3 here, which seemed to project out of a broader peak. The broad peak seems comparable with the defect peak X_b assigned to sulfur related defects by *Wu et al.* [80, 120]. However, in their work this peak is distinct from the free exciton peak, alongside other observations [69].

If we take the highest energy peak X_1 to be the free exciton peak we can plot the same data in terms of the additional binding energy relative to X_1. If the carriers involved in the formation of excitons begin closer together in energy due to carriers occupying defect states, we will observe defects which are bound deeper into the band gap. Oxygen substitutions for chalcogens have been shown to create local states just above the valence band. X_b is observed between 0 and 0.2 eV below X_1, which could correspond to the involvement of holes occupying these defect states.

Initially, the two flakes resolved thin peaks shown in Figure 6.9. Both room temperature and cryogenic PL measurements show a shift in the average emission energy towards a lower value, but emission up to 1.75 eV can be seen after plasma exposure, indicating that this is not simply a shift in the energy of the peaks. Nonetheless, the peak emission wavelength has dropped by ~ 0.5 eV.

Wu et al. also observed a 'deeper' defect peak $X_{b'}$ at photon energies of 1.35 eV which is attributed to tungsten vacancies, defect clusters or antisites. This bares some resemblance to the peak we observe at ~ 1.4 eV. As this peak lies between 0.2 and 0.5 eV below X_1 it is possible that this is caused by defects further into the band gap, but it is not clear what they would be if this were the case. To collect chemical information about the cause of these changes one would need to carry out additional measurements with equipment such as an XPS.

Exposure to nitrogen plasma reduced the signal in cryogenic measurements as well. It also led to a reduction in the intensity of the PL signal at higher energies such as X_1 with the highest signal now measured over 0.1 eV below X_1. A signal is still collected at these higher peak positions and there is a noticeable impact of these peaks on the gradient of the spectrum. This suggested that we are not observing a shift in the energy of the exciton states, but a preference for lower energy states. As this preference is to be expected, the change is likely caused by the introduction of new in-gap defect-related states.

Again, there are sharp peaks projecting out of X_b, but they are at lower energies consistent with the overall shift. Interestingly $X_{b'}$ sees a reduction in intensity as a proportion of the total signal as well as in absolute terms. This seems to say that less excitons are bound this deep in the band gap. It is possible that the N_2 plasma has removed these states by changing the population of defects. We have observed the introduction of faint defects and the creation of paired defects during exposure to N_2 on HOPG, which would lead to more defect states and even possibly a change in the energy of the defect states, but oxygen substitutions do not have deeper states that could be removed when converted to a nitrogen substitution if

X_1	1.18
X_2	1.12
X_3	0.64
X_b	0.41
$X_{b'}$	0.61

Table 6.1: The gradient of each line in Figure 6.9e indicating the power dependence of each peak.

this was the source of change in the cAFM images.

In order to consider the nature of the peaks I studied their power dependence. The three clear peaks in the cryogenic PL spectrum before plasma exposure were fitted to lorentzian functions along with X_b and $X_{b'}$. Figure 6.9e shows the natural logarithm of the height of these peaks plotted against the natural logarithm of the power and linear fits for each peak. If the dependence was perfectly linear, the gradient would equal 1 or 2 for a purely quadratic function; reflecting the exponent of the dominant power. The gradients are shown in Table 6.1, indicating that the first two peaks have an approximately linear dependence. This would suit the common attribution that the highest energy peak (X_1) is the free exciton and the second highest (X_2) trion peak [120, 121, 114]. These peaks are not limited by the number of defects in the sample and they are not bi-excitons which require exciton-exciton interactions and thus have a quadratic relationship on the power. X_3, X_b and $X_{b'}$ have much lower gradients closer to 0.5, indicating some form of saturation is occurring. This would be in line with the excitons which cause these peaks binding to defects. There are a limited number of defects and thus it becomes more difficult to form excitons at this energy as their number increases.

The high resolution observed in the peaks of the first sample was not seen at the site of the second flake, as can be seen in Figure 6.9. However, the same overall reduction in the energy of the PL emission can be seen here. After measuring at the second flake I returned to the original flake and found that I was not able to recreate the high resolution. The presence of the sharply defined peaks was consistent across

a long time and during calibration they were observed in this manner at multiple locations. This seems to indicate a change that occurred during the experiment. For this reason I recalibrated the PL system, but I only saw a minimal improvement in the resolution.

6.6 Conclusion

In this study the ability to observe changes in the defect population due to plasma exposure with cAFM has been demonstrated alongside the impact of plasma exposure on the PL spectrum. This is a solid foundation for further work to tie these strands together. More cAFM images are necessary in order to increase the reliability of these results and more photoluminescence spectra.

In particular, cAFM images after longer exposure times would illuminate the changes that occur as the density of defects in a sample becomes very high. There must become a point where the sample is very far from WSe_2 and begins to act in a different manner; assuming that the sample remains intact.

Further observations using different plasmas to see if different defects can be created would help us identify what causes the PL features. Argon plasma, followed by flushing the chamber with a gas of choice may enable the implantation of different elemental species or simply result in physisorbed molecules as has been observed with Nitrogen on MoS_2 following annealing [69].

The work carried out here shows that there are observable features to study with this method that could be used to carry out the further studies discussed above. Although decisive conclusions are beyond the scope of the data collected thus far, the data collected so far indicates that there could be much to be discovered in further study.

Chapter 7

Results: simulation of constant force atomic force microscopy

Experimental images with sub-molecular resolution were collected by my colleague Leonardo Forcieri in ambient conditions using PeakForce tapping mode atomic force microscopy (AFM). This technique is an off-resonance technique (described in Section 2.4.3), so this image is created with force feedback: an example of a constant force image. Figure 7.1 shows the features of Zn tetra-phenyl porphyrin (ZnTPP) observed when it formed a molecular network on the Au (111) surface. From these images, it is not immediately clear which sections of the molecules are contributing to the lobe-like shapes. If the images were taken using a constant height technique the Probe Particle Model (PPM) would be an ideal tool for attempting to understand the origin of these features, but there is no easily accessible method of determining the origin of features for a constant force technique. As a result, the simulation described in Section 4.1.2 was developed to attempt to understand the images.

The simulation of constant force images has applications both in and outside the vacuum environment. In the ambient environment, the use of constant force AFM simulations can be used to determine what was imaged with existing constant force techniques. However, simulating constant force AFM images offers us the

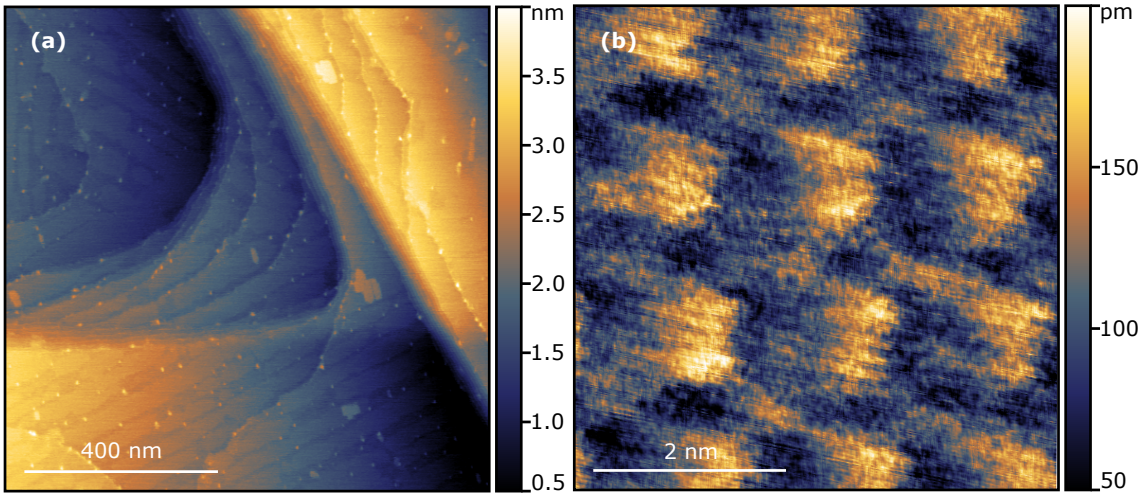

Figure 7.1: ZnTPP imaged by Leonardo Forcieri using PeakForce tapping mode, an off-resonance technique that uses force feedback. ZnTPP forms islands on Au(111) at sub-monolayer coverages *(a)* inside which, the repeating ZnTPP molecules can be resolved *(b)*. It is not clear from this image alone which parts of the molecules contribute to the image. The sub-molecular resolution image has been drift corrected so that the network lattice vectors are the same length and approximately 90 degrees apart. This is based on the literature in Chapter 3.4, of course, the correct dimensions of the lattice are not known.

opportunity to consider idealised images which represent an upper bound for measurement in a UHV environment. As discussed in Section 2.4.3, constant force images offer the ability to image parts of non-planar molecules which are closer to the substrate and thus hidden as constant height AFM cannot move close enough to measure a signal from them.

7.1 Simulation of individual molecules

To my knowledge, there are no examples of the experimental usage of constant force techniques in the UHV environment. However, as is discussed in Section 3.4, it is common to use a constant frequency as a feedback parameter, which is related to force. By measuring the frequency shift of a cantilever in a 3D grid representing a region of space the iso-surface of 0 frequency shift can be found. This is a force

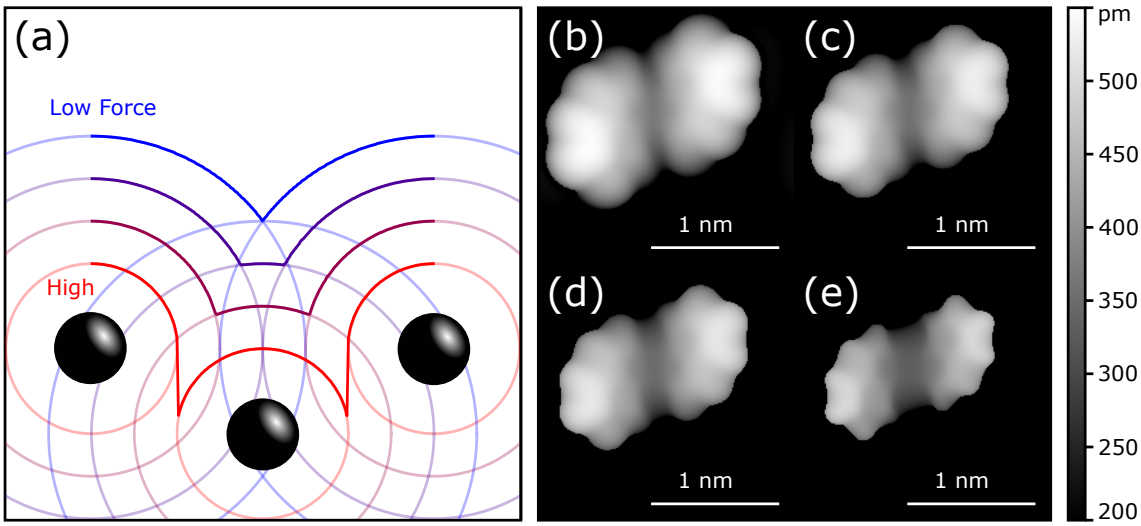

Figure 7.2: A cartoon *(a)* showing that if the force iso-surface is derived from drawing a sphere around each atom, images using small positive forces are unable to observe the lower atom. Also shown are simulated constant force AFM images of dibenzo [a,h]thianthrene (DBTH) using force set-points of 0 pN *(b)*, 50 pN *(c)*, 100 pN *(d)* and 250 pN *(e)*. As the force set-point is increased, the more space is observed between the two sections of the molecule and the more the variations in the surface due to the ring structure of the molecule stand out.

iso-surface that can reliably be attributed to a particular force: when $\frac{dF}{dz} = 0$ at the most negative part of the Lennard-Jones potential [33, 132, 134]. The majority of the data recorded via such a technique is discarded, leading to long measurement times that necessitate atom tracking and incredibly stable conditions. Such data is incredibly difficult and time-consuming to record and, due to the unreliability of converting non-zero frequency shifts into forces it is uncommon for any other iso-surface to be measured. Measuring force iso-surfaces closer to the subject increases the risk of damage to the tip or subject, but reveals more information. Figure 7.2 shows that the greater the force (positive) experienced by the tip, the more details can be resolved. If we consider an individual atom, a force iso-surface should create a sphere around the atom due to the radial symmetry of the Van der Waals force. The measured surface would not be a sphere because we only measure the force in the z direction, but this serves as a good way to demonstrate the advantages of using

a larger positive force. If we consider the force iso-surface of a molecule to consist of the highest points on the surface of one of the spheres at any x-y co-ordinate, then it is clear that using larger spheres will cover features that would be observable with smaller spheres and perhaps create new artefacts where two spheres meet. In reality, the force from the atoms is convoluted and we only measure the z component of the force, as discussed, but it still holds true that higher resolution can be achieved by using higher forces. Simulations of dibenzo[a,h]thianthrene (DBTH), imaged with different force set-points, are shown in Figure 7.2 clearly showing that as the force is increased, the gap between the two sections becomes clearer. In addition the rings in the sides of the molecule are clearer at higher force set-points.

It is clear then, that a technique that can measure positive forces with a high enough accuracy and measure in a single scan would be very beneficial to the measurement of force iso-surfaces. As discussed in Section 2.4.3, there are significant challenges to overcome in order to realise such measurements experimentally, but here we outline the additional information about molecules that could be gained.

Because constant height AFM plots the abstract value of frequency shift rather than z the angle between a section of a molecule and the surface cannot be measured reliably using NC-AFM. As mentioned above, measurements of frequency shift in a 3D spatial grid have been measured, allowing a zero frequency shift iso-surface to be extracted. This surface follows the geometry of the underlying molecule and the angle of absorption of ketone on Cu (111) has been measured in this way [134]. Here I will demonstrate how an idealised experimental implementation of constant force AFM would perform measuring the angle of phenyl rings in 2H-tetraphenyl-porphyrin (2H-TPP) as a form of upper bound.

7.1.1 Benzene and pyrrole

As 2H-TPP is a complex molecule, we begin our investigation by studying two smaller molecules, benzene and pyrrole, that could be considered to form a part of 2H-TPP. A comparison of the form of 2H-TPP and these molecules was made

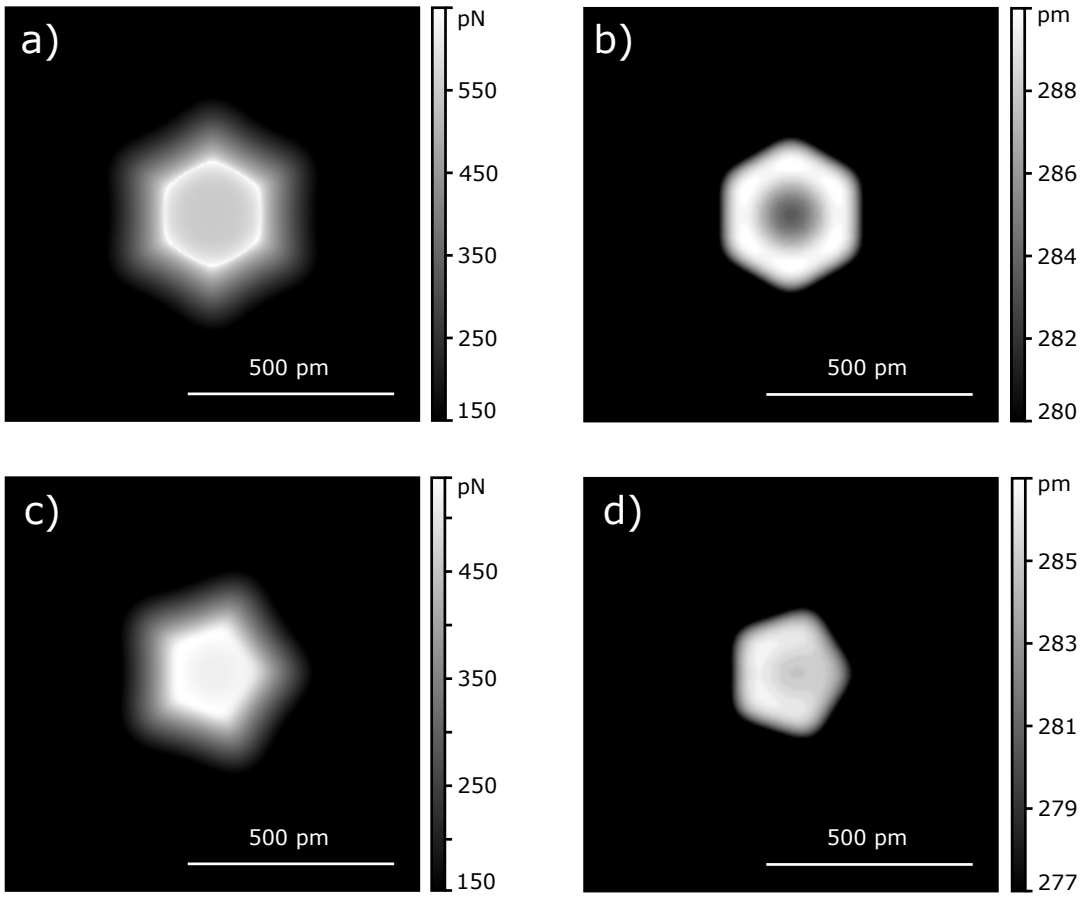

Figure 7.3: In simulated images of benzene at a constant height of 2.6 Å *(a)* a clear hexagonal shape can be made out with sharp edges. Using the constant force approach at a setpoint of 250 pN *(b)* the sharp edges are lost, but the ring is still observed at the very top of the data scale. Pyrrole has a smaller five-sided loop, leading to the sides being less distinct in both the images taken at a constant height of 2.6 Å *(c)* and a constant force of 250 pN *(d)*.

in Section 3.3.1. Due to their relevance, constant force and constant height AFM images of benzene and pyrrole were simulated with the molecule lying flat against the substrate and are shown in Figure 7.3. The constant height images were simulated using the Probe Particle Model, discussed in Section 2.6.1 and the constant force images were simulated using my simulation, discussed in Section 4.1.2. The substrate itself was neglected as it has an impact on how a molecule is arranged, but there is little contribution to the measured signal from the atoms in the surface in AFM images of molecules. In the constant height images, the bonds appear to have been

imaged, but the simulation was simply given the position and element of the atoms and only the Lennard-Jones force is calculated. The origin of these features in NC-AFM is discussed in Section 2.6.1.

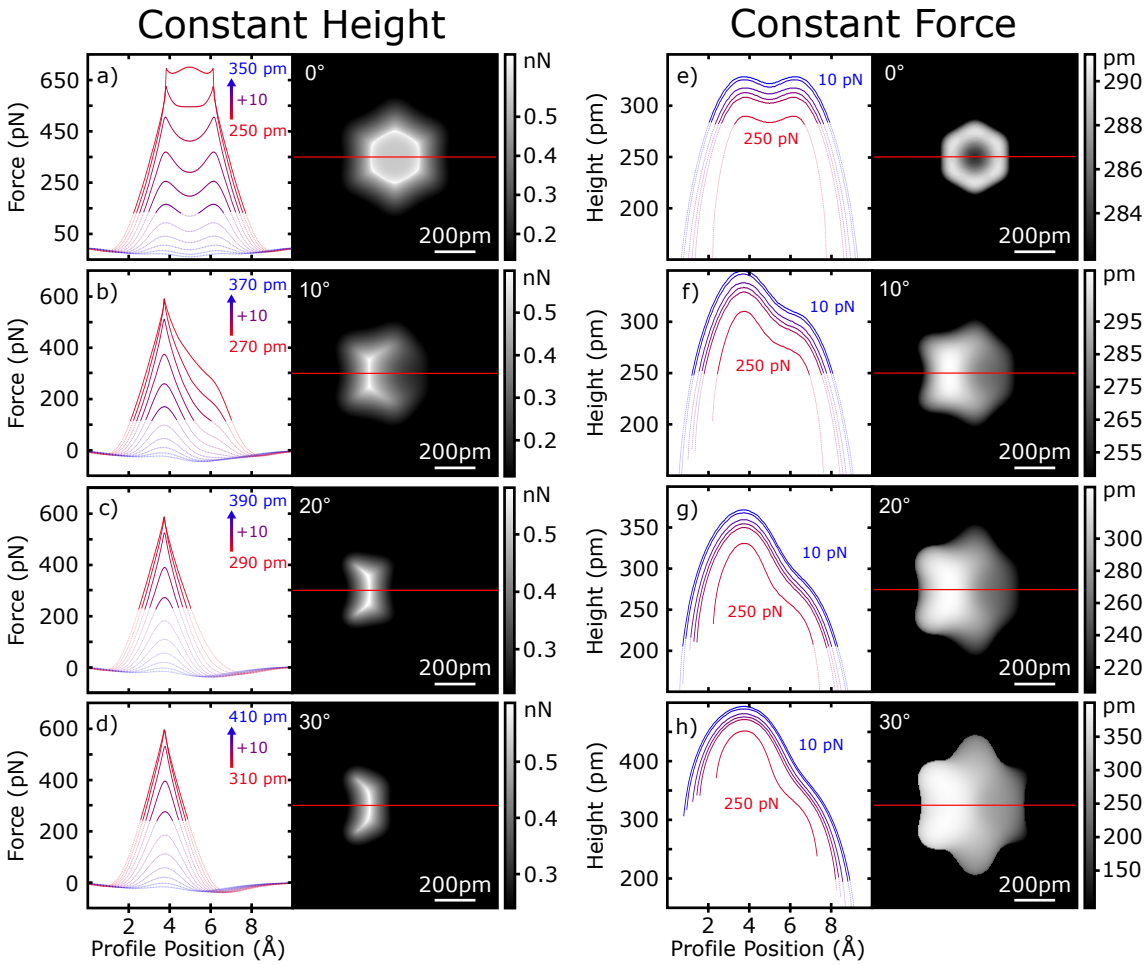

Figure 7.4: Constant height *(a-d)* and constant force *(e-h)* images of benzene, simulated at increasing angles of rotation. Red lines across the images indicate the line along which profiles were taken and then plotted to the left of the image. The profiles of the constant height images were taken over a range of 100 pm in 10 pm steps, beginning 250 pm above the height of the highest carbon atom. The constant height images are taken 260 pm above the highest carbon atom. The constant force profiles were taken using force set-points of 10, 20, 50, 75, 100 and 250 pN with the final force set-point pictured beside it. The region of the profiles that lies outside the range of the colour scale for the accompanying image is faded to indicate which features do not appear in the images.

In order to determine how constant force AFM compared with constant height AFM images using both techniques were simulated of benzene and pyrrole across a range of angles between the plane the molecule's atoms lie in and the surface. In Figure 7.4, the constant height image taken at a 0 degrees angle of rotation and 260 pm above the molecule is very clear, depicting a hexagon with sharp, well-defined sides. However, as the molecule tilts, the ability to resolve all six sides is lost. Images of the molecule were simulated at eleven heights for each rotation angle, resulting in a spectrum of profiles taken across the benzene molecules. The closer to the molecule the profile is taken, the sharper the increase in force when the tip is at its closest to the atoms. In the closest profile, the tip becomes so close that the contributions from all the atoms create a collective peak in the middle of the ring.

As the molecule is rotated, the closest 'bond' remains sharp, but the remainder of the molecule quickly disappears. In the profiles, the second peak can be seen disappearing as the force measured over it becomes negligible. The profiles are taken at the same heights above the highest carbon atom at all four rotation angles and the images always correspond to the second closest profile. Using a constant height technique is clearly not a viable way to measure the angle a benzene molecule is adsorbed at relative to the surface.

In constant force images, taken at a force setpoint of 250 pN the lower sections of the molecule are always visible. Even though at higher angles of rotation the contributions from higher atoms can begin to extend over those below the lower atoms can still be clearly inferred. However, this is done at the cost of the sharp features of the constant height image. Such features derive from the abstract nature of those images though, whereas the force iso-surfaces probed in the constant force images follow the geometry of the molecule. In the accompanying profiles, taken at a range of forces, the iso-surfaces can be seen to lie at an angle on top of the molecule. There are bumps over the positions of the 'bonds' and a dip in the centre though which complicate the measurement of the conformation angle. For measurements of non-planar molecules, the constant force images offer more information than the

constant height images then, though there is a clear loss of clarity in observing planar molecules.

Of course, these simulations are assuming that there is a single atom in contact with the object and perfect symmetry. A larger tip may smear out features and anisotropy may lead to a particular direction in which this effect is more pronounced.

In order to discover if the angle of rotation could be recovered from these images, a plane was fitted to the surface. The z height of a pixel in the 250 pN images was compared to that of the plane and a least squares method was used to find the plane of best fit. The angle between the plane and the surface was then taken to reflect the angle between the surface and the molecule. Figure 7.5 shows that for both the benzene and pyrrole molecules the angle of rotation is recovered accurately within a tolerance of 1 degree.

7.1.2 2H-TPP

Having shown that simulated constant force images can recover the angle of rotation of benzene and pyrrole, the technique was applied to 2H-TPP. There are two common adsorption geometries of this molecule that have very different phenyl positions. In the 'saddle' geometry, the phenyl rings are at an angle of ~ 27 degrees relative to the substrate. The measurement of these angles should be relatively similar to that of the benzene rings imaged above. In the 'inverted' geometry, the phenyl rings lie almost flat against the substrate at an angle of ~ 4 degrees. We should be able to tell the difference between these geometries and successfully determine the angles of the phenyl rings. The phenyl rings were fitted as shown in Figure 7.6 and the angles of all four rings were extracted and then plotted against the true value measured directly from the atomic co-ordinates in panel (a) of Figure 7.5.

The 'inverted' geometry is measured extremely well with the values 3.9, 3.9, 3.8 and 3.9 degrees and an error of ± 0.5 degrees which encompasses the 'true' values of 4.1, 4.1, 3.9 and 3.9 respectively. By contrast, the phenyl rings in the 'saddle' geometry were measured to have angles of 22.5, 22.5, 22.7 and 22.5 degrees with

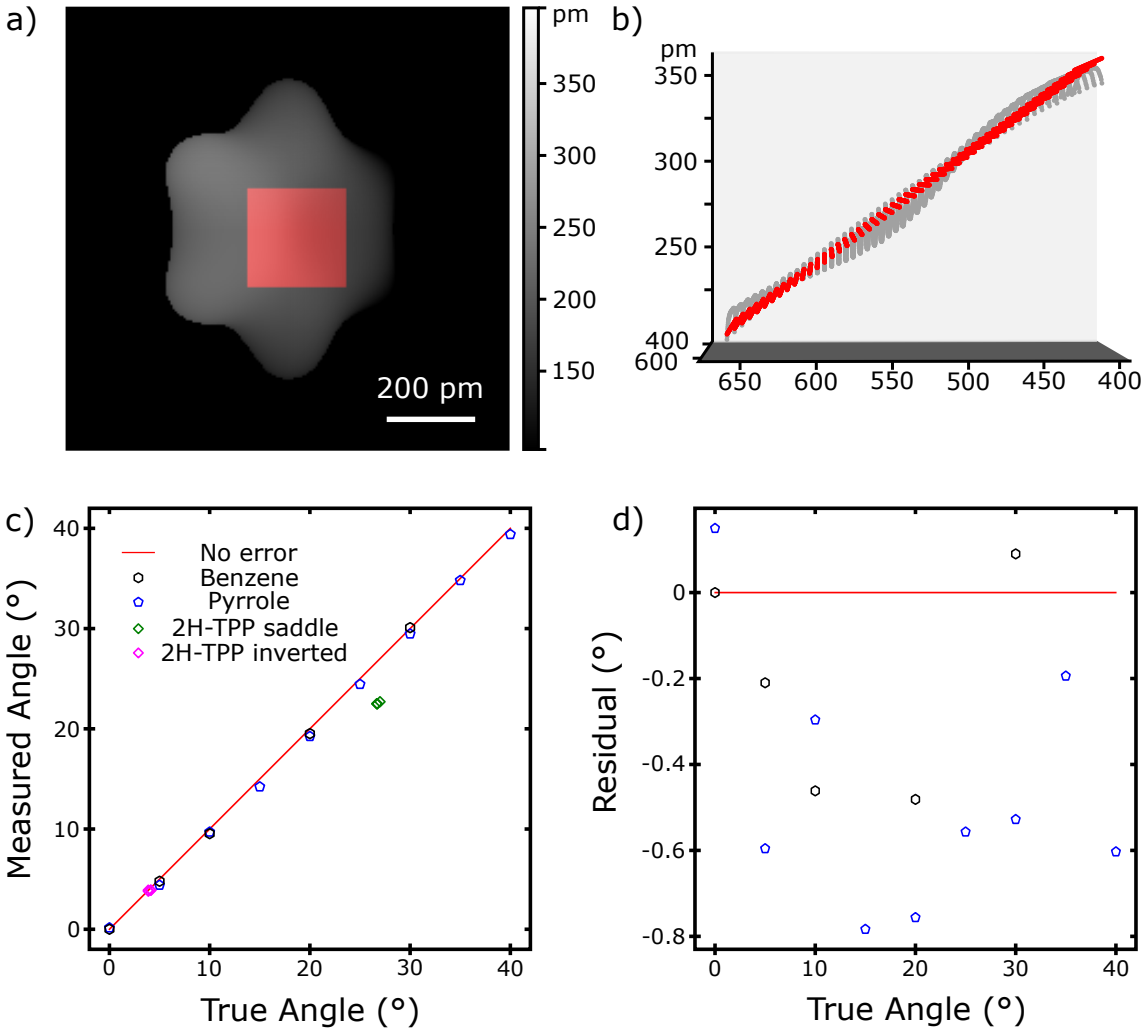

Figure 7.5: Squares such as the one overlaid on the constant force image simulated with a force set-point of 250 pN in *(a)* were fitted using a least squares method to the force iso-surface (grey). This is illustrated further in a 3D plot of the square region *(b)*. The fitted square is shown in red and the data it is fitted to is shown in grey. The measured angle of rotation for benzene and pyrrole is plotted against the angle the co-ordinates were rotated by *(c)*. All of the data for both pyrrole and benzene lies close to the red line indicating where the measured angle equals the true angle. The measured angle of phenyl rings in 2H-TPP in the saddle and inverted geometries are also plotted. The difference between the measured angle and true angle (residual) is plotted showing a deviation that is consistently less than 1 degree.

an error of 0.9 degrees. This does not include the 'true' values of 26.7, 26.7, 27.0 and 26.7 degrees. The angle of benzene could be recovered well at angles near 27

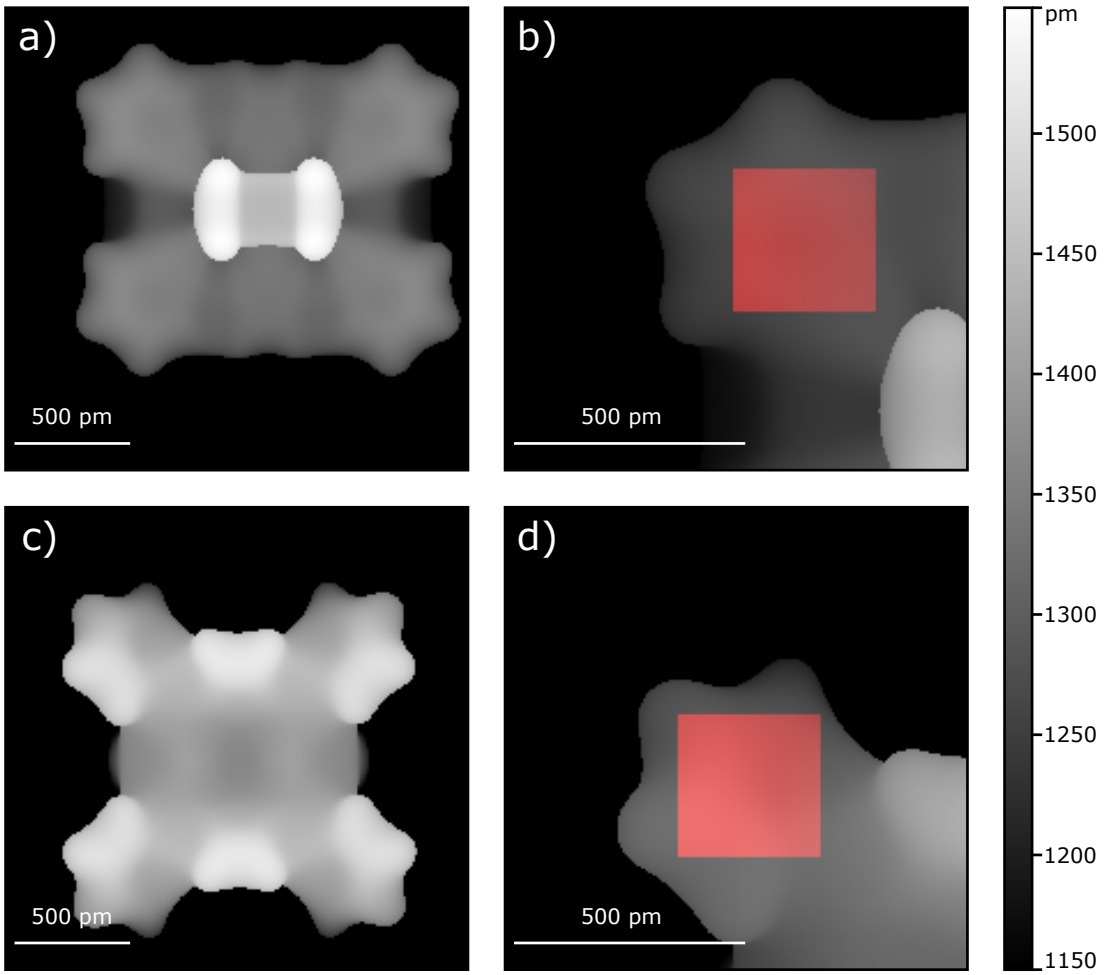

Figure 7.6: Images of 2H-TPP simulated with a force set-point of 250 pN and a lateral stiffness of 4 N/m. In the inverted geometry *(a)* the phenyl rings can be seen to lie relatively flat. The phenyl rings were then simulated alone such as the top left ring depicted here *(b)*; the red square shows the section used for plane fitting. The same process was carried out for the 'saddle' geometry *(c)-(d)* where the phenyl rings are tilted at ~ 23 degrees.

degrees, so it seems that the difference here originates from the remainder of the molecule. In Figure 7.6 one can see that a shoulder protrudes into the phenyl ring, which could affect the angle that the plane is fitted to. At lower angles, such as in the 'inverted' geometry, the phenyl ring is at an angle which is closer to the angle of the macrocycle and, as a result, the rest of the molecule may have less of an influence on the measurements.

7.1.3 Valid parameter space

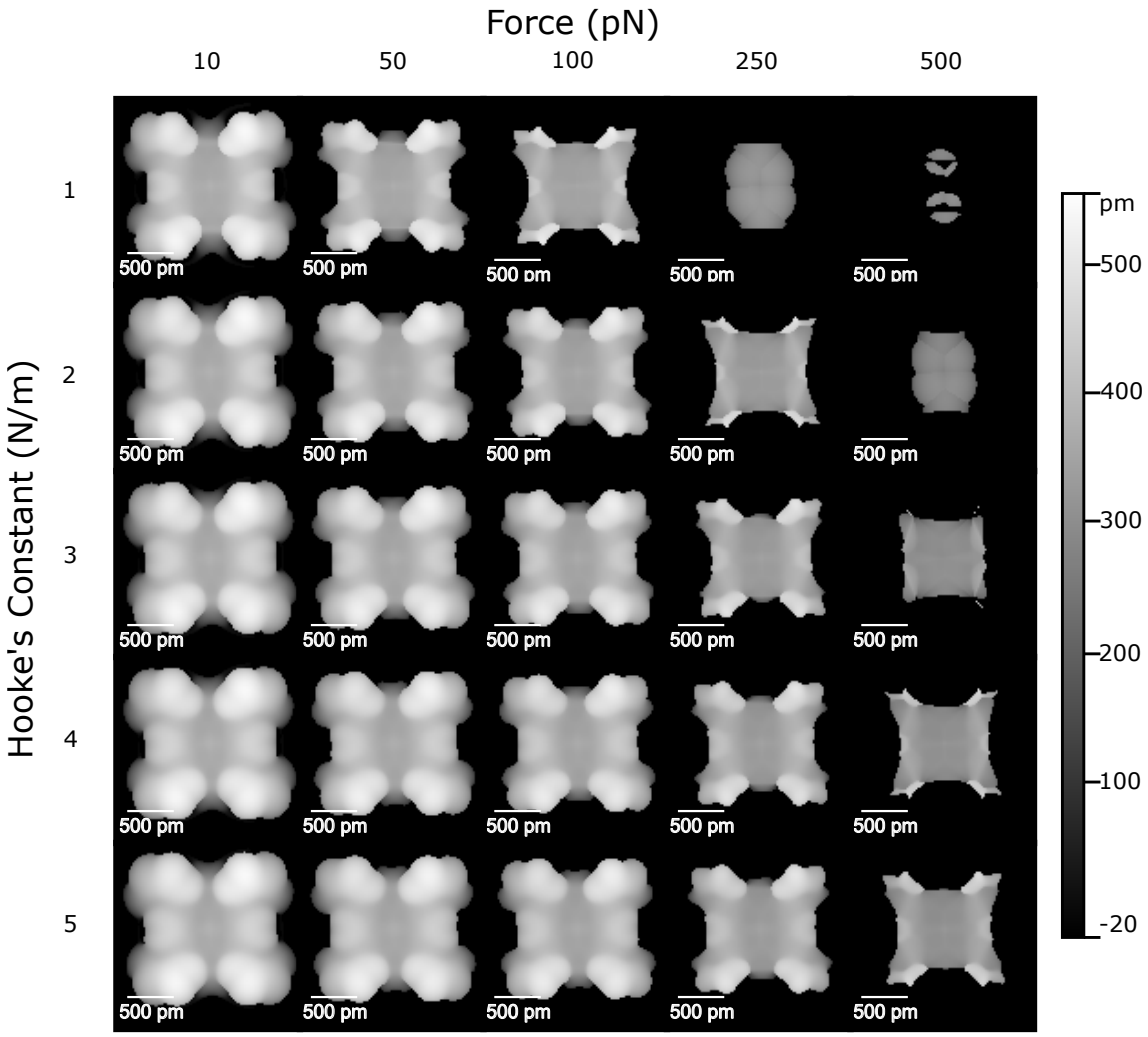

Figure 7.7: At high forces and low Hooke's constants the simulation begins to create aphysical images. The higher force also reduces the size of the lobe-like features in a constant force image of ZnTPP.

The simulation functions well when the parameters lie within a particular region of the parameter space, but if parameters are not set thoughtfully the simulation can fail. Assuming that the user has inputted sensible values that could be encountered in the real world, the main region for error comes from the resolution of the simulation. Space is, of course, continuous and simulating a continuous space numerically has its problems.

The first point at which problems could arise is during the simulation of the Van der Waals force field when using the Probe Particle Model. The force field is calculated as a grid of discrete points specified by the user. If the simulation requires the force in between the points in this grid, the value is calculated using interpolation. If the points in the grid are too sparse, sharp features in the field will disappear and the Van der Waals forces will be more erroneous in general.

Once the grid has been generated, the user then specifies a second grid detailing, for each initial tip position, the position of the probe particle and the force experienced after relaxation. If this grid is created with a too-low resolution, the sharp rise in the force as the tip nears the sample can be missed. The window for this is larger than one might think, because of the relaxation. A tip can relax to areas of lower force when measuring in areas of the molecule with high topographic variation and eventually, the probe particle may be placed in aphysical places before the force set-point is measured. It is key to understand that the probe particle is not lost due to high lateral forces that would stop measurements in an experiment and the only particle that can experience a force is the probe particle. The simulation breaks down in such situations and the probe particle effectively moves through the molecule and returns an aphysical value of z.

Both problems can be solved by improving the resolution of the simulation, but improving the resolution too far requires an unreasonable amount of processing power or time. The relaxation of the probe particle is also affected by the chosen parameters though. Figure 7.7 shows how an image of ZnTPP changes when it is subjected to different values of the lateral Hooke's constant k_{lat} and the force set-point. A k_{lat} is increased, the distance travelled during relaxation is reduced, meaning that the force set-point is likely measured before the probe particle is placed in an aphysical location. Decreasing the force set-point has the same effect as lower values of force can exceed the set-point. Because of this, the simulation begins to fail if the force set-point is too great, or the value of k_{lat} is too high.

As one can see from the Figure 7.7, the parameters that were used as a default,

a force set-point of 250 pN and k_{lat} of 4 is a reliable combination that still retains the benefits to resolution from a higher force.

7.1.4 Simulations of additional molecules and quantum clusters

In addition to 2H-TPP, benzene and pyrrole a number of additional molecules and quantum clusters have been simulated and are shown in Figure 7.8.

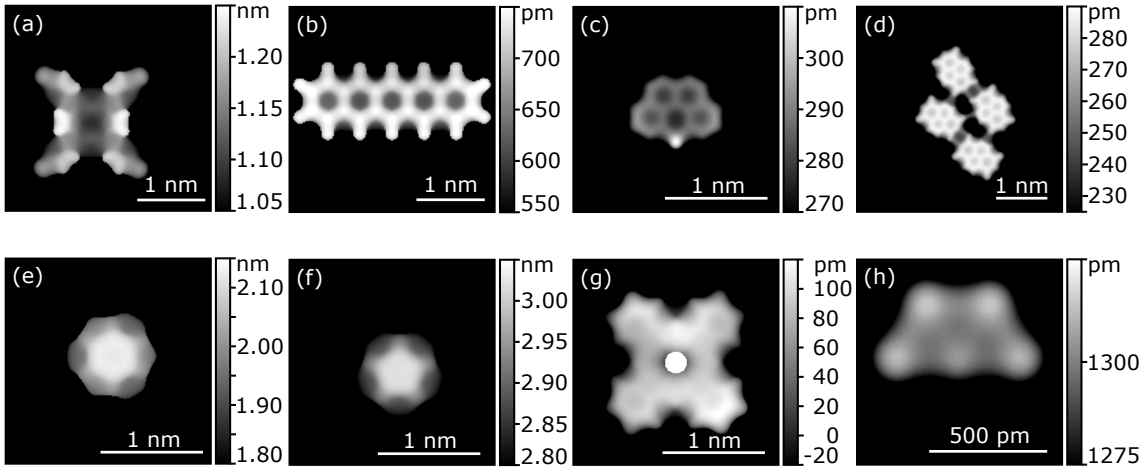

Figure 7.8: Br_4TPP *(a)* has a bulge at the tips of the phenyl-like groups where the bromine atom lies. Pentacene *(b)* has much thicker 'bonds' in a constant force image relative to the constant height images observed in literature. In the case of Olympicene *(c)*, the carbon atom with two hydrogen atoms rather than one is perceived as higher in a topographic image. The apparent hydrogen bonds between NTCDI molecules can be clearly seen *(d)*, as can the difference between the pentagonal and hexagonal sides of C_{60} fullerene *(e-f)*. Iron phthalocyanine with a carbon monoxide molecule complexed on the iron atom can be observed beneath the adsorbed molecule in this simulated constant force image. Finally, the atoms in a Cu_5 can be made out in these simulated coordinates.

Replacing the hydrogen atom at the tip of each phenyl ring in 2H-TPP with a bromine atom creates Br_4TPP, which can be differentiated due to the varying strength of the Van der Waals interaction on different elements. The much larger bromine atoms are much more prominent than hydrogen atoms, leading to large

bulges at the tips.

As discussed in Section 3.4, pentacene was the molecule used to show sub-molecular resolution with NC-AFM. In this constant force image, the linking sections between atoms in the image are much thicker than in CO-functionalised NC-AFM images.

Using the co-ordinates provided by *Mistry et al.* [155] I simulated constant force images of olympicene, a benzo[cd]pyrene which consists of five carbon rings which share atoms like a small piece of graphene. One of the carbon atoms has two hydrogen atoms attached and this atom stands out clearly in the constant force image as a raised section.

A good molecule for benchmarking the resolution of images is NTCDI (naphthalene tetracarboxylic diimide) because NC-AFM images show the once controversial features which look like hydrogen bonds. These features were discussed in detail in Section 3.4 where it was determined that other factors are able to produce these features without the relatively weak interaction from the bond itself. Sure enough, in our simulated image of NTCDI, we observe these features even though the image was produced solely with the Van der Waals interaction and atomic coordinates.

C_{60} fullerene is a carbon allotrope where the carbon atoms form a spherical cage. The cage consists of hexagonal and pentagonal sections. As a result, there are two possible ways for a C_{60} to arrange on a surface: either a hexagon faces upwards (Figure 7.8e) or a pentagon faces upwards (Figure 7.8f). The difference in this top face can clearly be seen, but in addition, one can make out that the pentagonal faces adjacent to the top face appear to be higher than the hexagonal faces, allowing for the nature of the neighbouring sides to be determined as well.

As discussed in Section 3.4, a carbon monoxide (CO) molecule can be adsorbed onto an iron phthalocyanine (FePc) molecule at the site of the iron atom. This CO-FePc molecule was observed by *Chen et al.* using NC-AFM [44]. Until the CO molecule was removed, the base of the molecule was invisible using NC-AFM, but after the molecule was removed by its interaction with the tip the molecule could be

brought close enough to observe the base. Using co-ordinates provided in this work I have simulated a constant force image (Figure 7.8f), showing that the base can be seen even with the CO molecule adsorbed, assuming that the molecule would not be removed by an interaction with the tip. Nonetheless, this illustrates the benefits of using force feedback, the lower sections of the molecule are visible and the force in z never exceeds 250 pN.

Finally, Cu_5 is a quantum cluster comprising of five copper atoms which can be arranged in either a 3D or 2D structure [156]. Density functional theory simulations carried out by Qingqing Wu at Lancaster University provided the coordinates for the cluster which were simulated to create constant force AFM images. The individual atoms can be resolved and the side of the structure with two Cu atoms appears slightly higher.

Having become satisfied that the simulation results in plausible images and having determined a valid parameter space we now turned our attention back to the ZnTPP molecule at the heart of the simulated study.

7.2 Network of ZnTPP on Au (111)

With a successful simulation of constant force AFM, work could begin on simulating a molecular network of ZnTPP on Au (111). Before constant force AFM images can be simulated our collaborators at Luleå University of Technology must simulate the atomic coordinates representing how a molecule positions itself on the surface. This is achieved by relaxing the molecule in density functional theory (DFT) simulations, but due to the large computational load it is infeasible to simulate a large system and it is common to find a small periodic cell which can be repeated to create the system. During DFT the periodic cell is simulated with periodic boundary conditions enabling a much larger system to be reduced to a much smaller number of components whilst still retaining reliability. This meant that the first step in simulating the creation of these images was to find a periodic cell.

	Porphyrin	ϕ_1 (°)	ϕ_2 (°)	λ_1 (Å)	λ_2 (Å)
Controlled Metalatio... [138]	FeTPP			14.3	14.3
Self-assembly and co... [139]	H2-TPyP	60	60		13.9
Physical Properties ... [141]	CoTPP			14	14
	NiTPP			14	14
Orbital-specific dyn... [140]	FeTPP	59	59		
Visualizing the Fron... [142]	CoTPP	35	35	14.2	14.1
Site-specific electr... [143]	CoTPP	45	45	14	14
Self-metalation of 2... [145]	2HTPP	20	20		
	CuTPP	40-50	40-50		
Zinc(II) tetraphenyl... [123]	ZnTPP			13.1	12.6
Identifying the Asse... [146]	ZnTPP			13	12
Molecular assemblies... [147]	ZnTPP			14.0	14.0
Zinc(II) tetraphenyl... [148]	ZnTPP			14.4	14.0

Table 7.1: The lattice parameters and phenyl ring rotation angles for monolayer networks of porphyrin molecules on metallic surfaces. These values came from STM and NEXAFS studies.

Finding a periodic cell for the simulation might have been trivial, but the surface of Au(111) has a 'herringbone' surface reconstruction which complicates the system, as discussed in Section 3.3.3.

To reduce the computational load we opted for approximating the surface to a non-reconstructed surface, but this would require further modification in order to achieve a meaningful representation of the surface. Because relatively small changes in the distances between atoms can collectively lead to a much larger lattice cell, it is possible to simply stretch the non-reconstructed cell in order to retain the periodicity of the lattice, but extend it over a larger area of space. Essentially, if molecule-molecule interactions are the dominant factor in the conformation of the molecules, this method allows us to focus on that interaction.

However, a viable periodic cell for the non-reconstructed surface containing an entire ZnTPP molecule needed to be found as a starting point. Networks of tetra-phenyl porphyrin molecules have been studied extensively on coinage metal substrates with STM, providing a wealth of information on how they are typically

arranged [15, 123, 138, 139, 140, 142, 143, 144, 145, 141, 146, 147, 148]. This information is presented in Table 7.1 where we can see a number of clear trends.

By reviewing these studies we can see that a molecular network of porphyrin molecules typically has network lattice vectors λ_1, λ_2 of $\sim$ 14 Åin length with an angle γ in between of $\sim$ 90 degrees. The phenyl rings tend to be rotated by angles of less than 60 degrees relative to the surface. As they are typically arranged in two pairs with similar angles of rotation the angles are denoted here as ϕ_1 and ϕ_2, where $\phi_1 > \phi_2$.

There are two reports of ZnTPP on Au (111) that show much lower network lattice parameters [123, 146]. As this seems to be limited to ZnTPP on Au (111), these reports may demonstrate that this molecule deviates from the general trend of $\lambda_1 \sim \lambda_2 \sim 14$ Å and so it is important that a cell of this size is investigated. In addition, a particular periodic cell, defined in terms of the lattice vectors of Au (111) is given by *Ruggieri et al.* [123]:

$$\begin{pmatrix} \lambda_1 \\ \lambda_2 \end{pmatrix} = \begin{pmatrix} 5 & -2 \\ -1 & 5 \end{pmatrix} \begin{pmatrix} a_1 \\ a_2 \end{pmatrix} \tag{7.1}$$

This periodic cell was adopted by our collaborators and relaxed using density functional theory. After relaxation, the parameters used were: $\lambda_1 = 12.6$ Å, $\lambda_2 = 13.1$ Å and $\gamma = 94.3$ Å, to three significant figures, which is very close to the desired cell. The main difference is that $\gamma \neq 90$ degrees. As our simulation assumed an idealized face-centred cubic lattice, this may be the cause of the discrepancy. Nonetheless, this is a good place to start. As shown in Figure 7.9, the cell is very small for these molecules and the phenyl rings must lie very close to each other, leading to the phenyl rings twisting to be almost perpendicular to the surface. This means that the ϕ values are well out of our expected range. The twisting of the phenyl rings has very little cost in the gas phase compared to tilting the bonds, but the phenyl rings repel the surface as they are twisted and this leads to the bond tilting upwards [144, 157]. Tilting the bond is very costly and it is often compensated

for by flattening the macrocycle. In the saddle geometry, the pyrrole-like sections of tetra-phenyl porphyrins alternate between the nitrogen atom pointing up and down as one travels around the core. This distortion is removed when the phenyl rings tilt up and we observe this in our images as all four pyrrole sections are similarly prominant. The nitrogen atoms are all tilted downwards to a similar degree and the carbon pair opposite is tilted upwards.

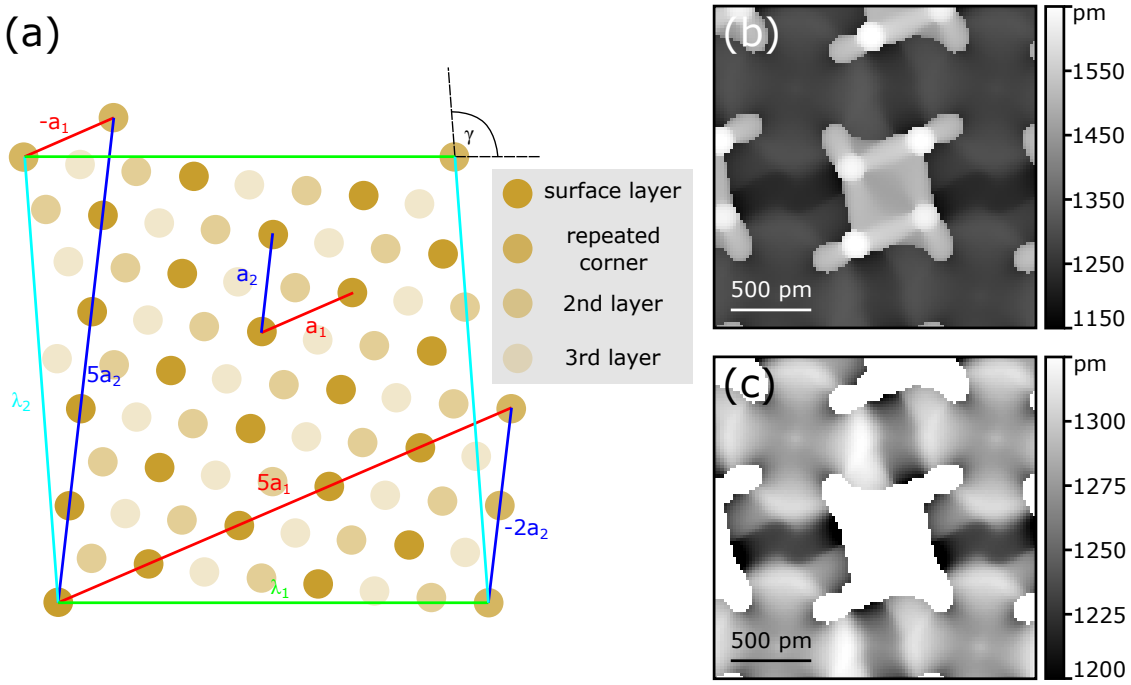

Figure 7.9: A diagram of the initial periodic cell detailed by *Ruggieri et al. (a)* showing the top 3 layers of Au atoms. After relaxation with a ZnTPP molecule above it using DFT a constant force AFM image was simulated at a force setpoint of 250 pN and $k_{lat} = 4$ N/m *(b)*. If the colour bar only spans the data from the phenyl rings *(c)* it is clear that they are perpendicular to the surface and, if the colour bar focuses on the macrocycle *(d)*, the four raised sections in-between the phenyl rings are at similar heights showing that pyrrole-like sections are all tilted so that the nitrogen atom points down.

Due to the extreme rotation of the phenyl rings, we looked at other possible cells that had similar dimensions. Approaching the problem from a perfect Au (111) lattice with no reconstruction, we found two periodic cells that lay close to the cells measured in the literature. Starting from an idealized fcc Au lattice with a lattice

	λ_1 (Å)	λ_2 (Å)	γ (°)	Matrix
Cell A	12.6	13.2	94.3	$\begin{pmatrix} 5 & -2 \\ -1 & 5 \end{pmatrix}$
Cell A (stretched)	13.7	14.4	94.3	$\begin{pmatrix} 5 & -2 \\ -1 & 5 \end{pmatrix}$
Cell B	15.3	16.1	88.1	$\begin{pmatrix} 6 & -2 \\ -1 & 6 \end{pmatrix}$

Table 7.2: The network lattice vectors λ_1 and λ_2 that define the computational cells used when they are by an angle γ apart. The network lattice vectors can be described in terms of the Au (111) lattice vectors though these matrices, such as in Equation 7.1. Cell A is a scaled up version of Cell A, including the lattice vectors of the Au (111) surface itself, meaning that the lengths of the network lattice vectors are the only values that change.

parameter of 4.07825 Å[124], the Au (111) plane was selected and two lattice vectors were chosen to build the lattice a_1, a_2 lying 60 degrees apart with a length of 2.88376 Å.

The first cell can be described by the same matrix as the one detailed in Equations 7.1, but the sides were calculated to have a marginally different value to those given by *Ruggieri et al.* in their work. They may have based their work more directly from the reconstructed lattice. The details of these cells are detailed in Table **??**.

As Cell A has similar parameters to the cell of *Ruggieri et al.* it was expected to result in a similar structure. Cell B has lattice parameters that are considerably larger than 14 Å, so the molecules are likely to not interact in a similar manner to those observed experimentally. Because the surface of Au (111) is reconstructed, neither of these cells are likely correct but, by stretching Cell A, we may be able to approximate the way that the molecules conform to the surface if their arrangement is predominantly determined by molecule-molecule interactions. In order to do this, Cell A was stretched so that the average of the two lattice vectors is 14 Å but the relative proportions remain the same.

Our colleagues at Luleå University of Technology simulated placing a ZnTPP molecule above the lattice such that the Zn atom sat directly on top a Au atom on

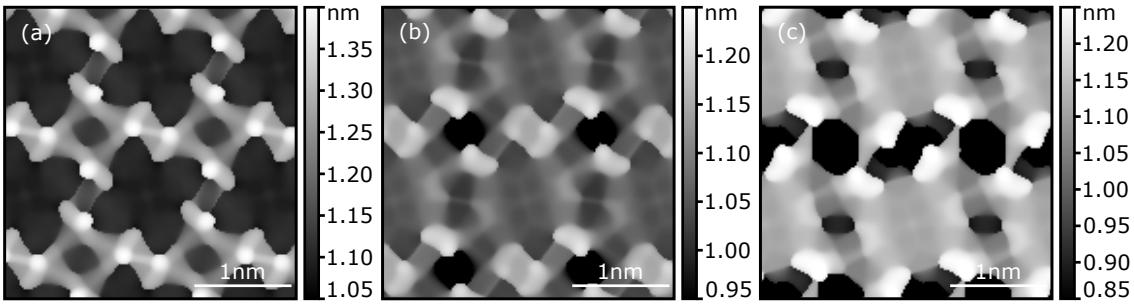

Figure 7.10: Constant force AFM images of ZnTPP monolayers simulated with a force set-point of 250 pN and a lateral Hooke's constant $k_{lat} = 4$ N/m of Cell A *(a)*, a stretched version of Cell A *(b)* and Cell B *(c)*. Cell A shows sharp features representing phenyl rings perpendicular to the surface, similar to Figure 7.9, whereas Cell B shows the classic saddle form. The stretch version of Cell A shows that the phenyl rings in different ZnTPP molecules are much closer, but they are not perpendicular to the surface.

the top layer and then the coordinates were relaxed using DFT simulations. The relaxation included the top 3 layers of Au and the layers could be fixed in place. There was very little distortion in the Au when it was allowed to relax for both cells, but the Au atoms drifted considerably in the stretched cell. This makes sense as the first two cells are actually periodic cells of Au (111), whereas the stretched cell is not. A good middle ground can be found by fixing the bottom layer of Au atoms, but allowing the other atoms to relax, but there was little difference between the simulated constant force AFM images, showing that the molecule-molecule interaction seems to be the dominant factor in the geometry of the molecules. In Figure 7.10 one can see that Cell A looks very similar to the cell simulated in Figure 7.9 as expected; Cell B shows ZnTPP in very typical 'saddle' geometry, indicating little inter-molecular interaction and the stretched cell lies in-between the two. The phenyl rings lie very close to sections of other molecules, yet they don't twist to angles close to the perpendicular. As a result, the classic saddle geometry with the alternating tilting on the pyrrole-like sections is clear. The highest sections of the molecules are still clearly the phenyl rings, though the two pyrrole-like sections with nitrogen atoms pointing down create a 2nd medium-height section, leaving the

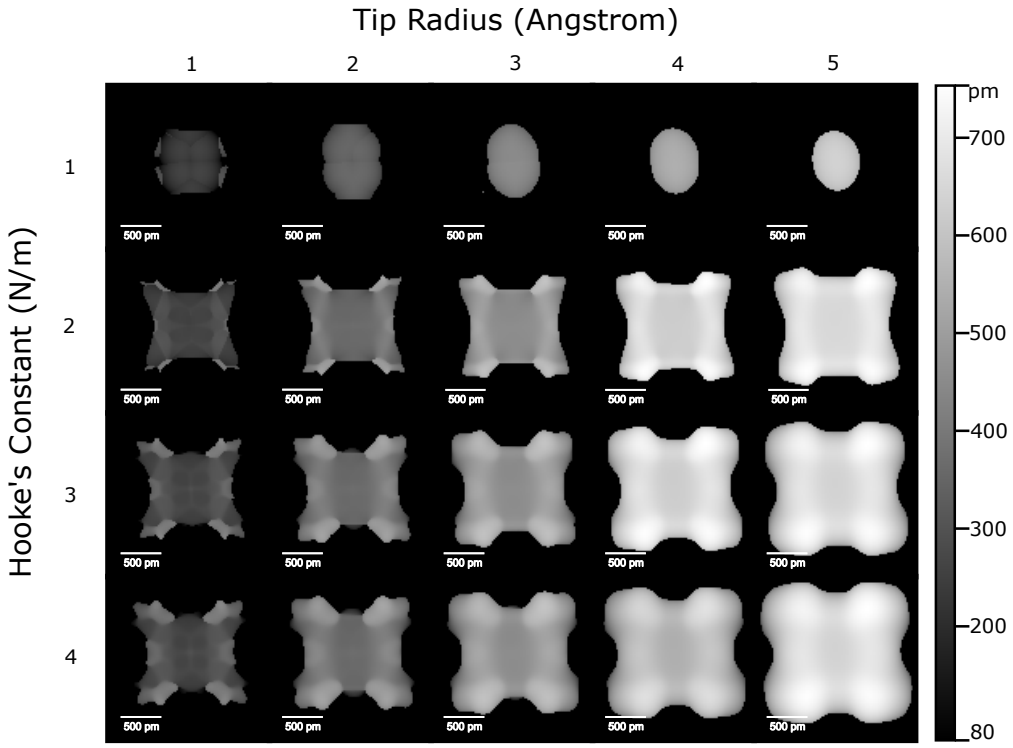

Figure 7.11: Images of a single ZnTPP molecule simulated at a constant force set-point of 250 pN and a range of values of tip radius and k_{lat}. When $k_{lat} = 1$ N/m, the simulation fails to image the molecule due to problems discussed in Section 7.1.3, but the general trend is that increasing tip radius increases the size of the features, resulting in the loss of the ability to resolve the Zn centre.

lowest section over the porphyrin core. The resulting shape is effectively a rough stripe that runs laterally across Figure 7.10 with vertical stripes forming between the molecules. This differs significantly from the experimental image in Figure 7.1 where the middle ground lies diagonally between the raised sections, indicating that the second highest section should be the centre of the macrocycle.

Further to this, the phenyl rings are not collected together, but instead form a lightning bolt pattern along the interfaces between the rows of ZnTPP. In order to resolve this, the molecule in the stretched cell was rotated by 10 degrees anticlockwise to see if there was a minimum in the formation energy when the phenyl rings were closer together. After relaxation a local minimum was found, resulting in the image in Figure 7.12b) which better resembles our experimental data.

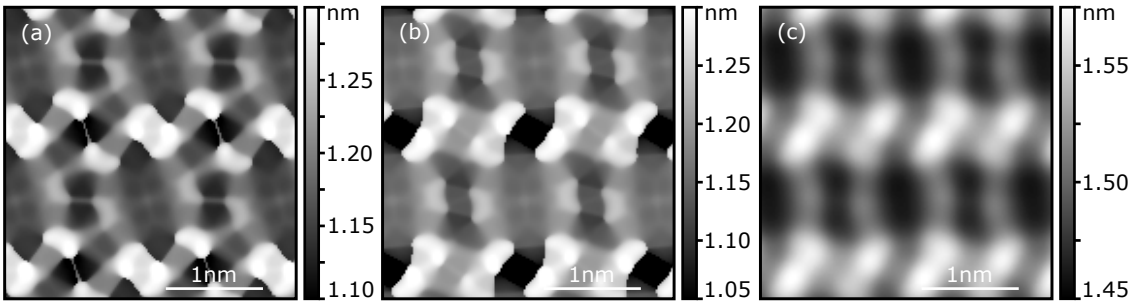

Figure 7.12: Constant force AFM images of ZnTPP monolayers simulated with a force set-point of 250 pN and a lateral Hooke's constant k_{lat} = 4 N/m of the stretched cell with all Au atoms fixed in place *(a)* and the same Au cell with the molecules rotated so that their phenyl rings are closer together *(b)*. These images were simulated with a CO tip, but the effects of a more likely tip apex can be simulated by increasing the size, such as in the third image where the tip has a radius of 5 Å.

As the phenyl rings move closer together due to rotating the molecule the central pair in Figure 7.12a is separated and the phenyl rings of each molecule interact with the rings of those above and below to form the L-shapes in 7.12b. Together they create a single highest section that repeats in a similar manner to our experimental images in Figure 7.1. Further to this, the split between the two L-shapes in each cluster seems like a likely origin for the coffee-bean-like splitting that is observed experimentally. This still leads to vertical stripes due to the pyrrole-like sections with two carbon atoms pointing upwards. By simulating Figure 7.12c with a 5 Å radius tip we can see how a tip with a lower resolution than a CO molecule terminated apex would observe the features of 7.12b. Similar to the unrotated image in 7.12a, we still observe horizontal rows of phenyl rings which are just about separable into clumps of 4 phenyl rings and vertical stripes from the pyrrole-like sections.

Increasing the radius of the tip apex lowers the resolution of the resulting image. In Section 2.5 the mechanism for this process is described. By simulating images of an individual ZnTPP molecule with a force setpoint of 250 pN and a range of tip radii and values of k_{lat} Figure 7.11 was created. At low values of k_{lat} the system suffers from the problems detailed in Section 7.1.3, but in the other panels the

features increase in size as the radius is increased, obscuring the finer details.

This minimum after the rotation was a local minimum, so there still remained the question of why the porphyrin would adopt this configuration. It is possible that the remaining differences between the experimental and simulated images observable in Figure 7.13, would be resolved through the resolution of this question. After all, the areas of middling height in the experimental images lie over the porphyrin cores rather than in between the porphyrin cores. Reviewing the literature we see that the phenyl rings seem to be close together in STM images, even though one would expect the hydrogen atoms to repel each other. As a result we will continue this study by considering whether the phenyl rings would rotate such that their π orbitals overlapped.

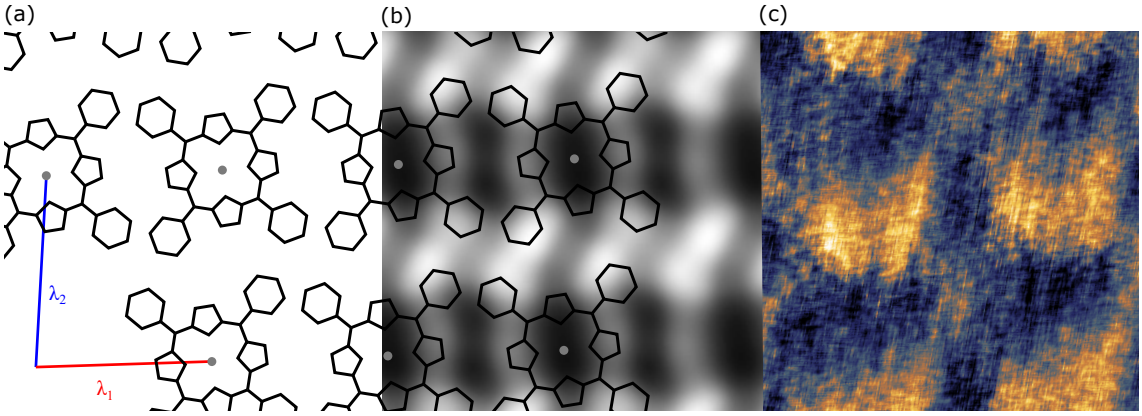

Figure 7.13: A cartoon of the structure of ZnTPP molecules in a network *(a)* may be compared to the simulated image *(b)* and the experimental image that inspired this work *(c)*.

7.3 Conclusions

To summarise the progress that has been made in the simulation of constant force images of molecules in this work: a simulation has been created that demonstrates that constant force methods can extract the adsorption angle of molecules and moieties and it has supported work to determine the adsorption geometry of ZnTPP on Au (111).

The implementation of constant constant force techniques in a vacuum has a clear drawback, in that off-resonance techniques will ring. In order to reduce the effects of ringing the drive frequency will have to be reduced significantly, leading to long measurement times in a vacuum. However, the ability to probe the peak force rather than the average force provides an opportunity to probe strong, short-range forces whilst the apex experiences very small forces for the majority of the oscillation cycle.

The applications of off-resonance techniques to acquire constant force images in ambient conditions are already widely practised and, as the limits of resolution in ambient conditions are tested, the need to interpret the features of images grows. The use of constant force simulations such as the example in this work can help with the identification of features through comparison of atomic coordinates from DFT simulations with experimental images and further validated with information from X-ray techniques such as NEXAFS.

Chapter 8

Conclusions

Across these studies there has been a unifying theme: pushing the boundaries of resolution in an ambient environment. At the start of this work, we considered how improvements in microscopy can support scientific study and, as a result, lead to significant impacts on everyday lives. In this work we have discussed improvements in ambient resolution which have been demonstrated by myself or a colleague and then shown how such improvements can be used to collect additional information. The ability to acquire more information about a material in an ambient environment allows for efficiencies in time, cost and the availability of equipment that can be used in the research and development of materials science.

The ability to use conductive atomic force microscopy (cAFM) to survey the density of defects in a sample with atomic resolution has been demonstrated. Further work could expand the materials which cAFM can analyse with this resolution and build on the current understanding of what is observed in cAFM images. The ability to consider the defects in a material without a vacuum environment could lead to the efficient assessment of materials. Coupled with the ability to identify changes in the defects in a material on either side of processing steps, one can begin to gain a more complete understanding of how a process affects a material.

Optical spectroscopy complements microscopy well as microscopy reveals a very small area and spectroscopy can be used to assess a much larger region. By using

microscopy to determine the origin of features in spectroscopy signals one can begin to consider the changes taking place across a larger sample with reference to the nanoscale origins of the effects. Here, we showed the beginnings of such a process, opening the door for further study. Nanoscale changes were observed after exposure to plasma and they were reflected in photoluminescence (PL) spectroscopy. Further work is necessary in order to identify more specific information about features in PL spectroscopy and to simply improve our confidence through repetition of the experiments.

Finally, the observation of molecular networks in an ambient environment dramatically accelerates the rate at which one can iterate on the preparation of molecules on the surface to achieve the desired parameters. If the conformation of molecules can be inferred in an ambient environment, one can identify this information without using a vacuum environment and interesting samples could be rapidly identified for a more detailed vacuum study. This could assist studies in topics such as molecular electronics, coatings and on-surface reactions for polymerisation. Further to this, it is clear that the development of constant force techniques in a vacuum could lead to increases in resolution and simpler ways to ability to navigate non-planar molecules. There are significant technical challenges in this respect, but it is clear that there are significant gains to reap from advances here.

New ground has been broken in all three studies that I hope will form the basis for future work to improve the acquisition of data in surface science. Developing these fundamental demonstrations into more standardised approaches will require a great deal more work. I hope that I have shown here that it is worth following these paths for future research and that a solid foundation has been laid.

Bibliography

[1] The Editors of the Encyclopaedia Brittanica. *Encyclopaedia Brittanica*. 2023. URL: https://www.britannica.com/science/science (visited on 04/20/2023).

[2] *The birth of the Web*. https://www.home.cern/science/computing/birth-web. May 2023.

[3] Richard P Feynman. "Plenty of Room at the Bottom". In: *APS annual meeting*. 1959.

[4] William J Croft. *Under the microscope a brief history of microscopy*. World Scientific, 2006.

[5] Albert Van Helden, Sven Dupré, and Rob van Gent. *The Origins of the Telescope*. Amsterdam University Press, 2010.

[6] Cameron Bjelkevig et al. "Electronic structure of a graphene/hexagonal-BN heterostructure grown on Ru(0001) by chemical vapor deposition and atomic layer deposition: extrinsically doped graphene". In: *Journal of Physics: Condensed Matter* 22.30 (2010). DOI: 10.1088/0953-8984/22/30/302002.

[7] Po-Chun Yeh et al. "Probing substrate-dependent long-range surface structure of single-layer and multilayer MoS 2 by low-energy electron microscopy and microprobe diffraction". In: *PHYSICAL REVIEW B* 89.155408 (2014). DOI: 10.1103/PhysRevB.89.155408.

[8] Leo Gross et al. "The Chemical Structure of a Molecule Resolved by Atomic Force Microscopy". In: *Science* 325.5944 (2009), pp. 1110–1114. DOI: 10.1126/science.1176210.

[9] Sara Barja et al. "Identifying substitutional oxygen as a prolific point defect in monolayer transition metal dichalcogenides". In: *Nature Communications* 10 (1 2019), pp. 1–8. DOI: 10.1038/s41467-019-11342-2.

[10] Hiroyuki Sugimura and Nobuyuki Nakagiri. "Scanning probe anodization: Nanolithography using thin films of anodically oxidizable materials as resists". In: *Journal of Vacuum Science and Technology A* 14 (1996), pp. 1223–1227. DOI: 10.1116/1.580271.

[11] E Sierda et al. "Quantum simulator to emulate lower-dimensional molecular structure". In: *Science* 380 (6649 2023), pp. 1048–1052. DOI: 10.1126/science.adf2685.

[12] Thomas Olsen et al. "Simple Screened Hydrogen Model of Excitons in Two-Dimensional Materials". In: *Physical Review Letters* 116.056401 (5 2016). DOI: 10.1103/PhysRevLett.116.056401.

[13] Kristian S. Thygesen. "Calculating excitons, plasmons, and quasiparticles in 2D materials and van der Waals heterostructures". In: *2D Materials* 4.022004 (2017). DOI: 10.1088/2053-1583/aa6432.

[14] Thomas McGrath et al. "A PUF taxonomy". In: *Applied Physics Reviews* 6.011303 (1 2019). DOI: 10.1063/1.5079407.

[15] Willi Auwärter et al. "Porphyrins at interfaces". In: *Nature Chemistry* 7 (2015), pp. 105–120. DOI: 10.1038/nchem.2159.

[16] Xintai Wang et al. "Thermoelectric properties of organic thin films enhanced by π–π stacking". In: *JPhys Energy* 4.024002 (2022). DOI: 10.1088/2515-7655/ac55a3.

[17] Franz J. Giessibl. "Advances in atomic force microscopy". In: *Rev. Mod. Phys.* 75 (3 2003), pp. 949–983. DOI: 10.1103/RevModPhys.75.949.

[18] G Binnig et al. "Tunneling through a controllable vacuum gap". In: *Appl. Phys. Lett.* 40 (1982), pp. 178–180. DOI: 10.1063/1.92999.

[19] Gerd Binnig et al. "7 × 7 reconstruction on Si (111) resolved in real space". In: *Physical Review Letters* 50.2 (1983), p. 120. DOI: 10.1103/PhysRevLett.50.120.

[20] Rebecca Howland and Lisa Benatar. *A Practical Guide: To Scanning Probe Microscopy*. Park Scientific Instruments, 1993.

[21] Greg Haugstad. *Atomic Force Microscopy : Understanding Basic Modes and Advanced Applications*. John Wiley and Sons, Incorporated, 2012.

[22] Matthew R Rosenberger et al. "Electrical Characterization of Discrete Defects and Impact of Defect Density on Photoluminescence in Monolayer WS_2". In: *ACS Nano* 12 (2 2018), pp. 1793–1800. DOI: 10.1021/acsnano.7b08566.

[23] Astrid Weston et al. "Atomic reconstruction in twisted bilayers of transition metal dichalcogenides". In: *Nature Nanotechnology* 15 (2020), pp. 592–597. DOI: 10.1038/s41565-020-0682-9.

[24] Saima A Sumaiya, Jun Liu, and Mehmet Z Baykara. "True Atomic-Resolution Surface Imaging and Manipulation under Ambient Conditions via Conductive Atomic Force Microscopy". In: *ACS Nano* 16 (12 2022). DOI: 10.1021/acsnano.2c08321.

[25] T. Tiedje et al. "Tip contamination effects in ambient pressure scanning tunneling microscopy imaging of graphite". In: *Journal of Vacuum Science and Technology A* (1988). DOI: 10.1116/1.575418.

[26] Xintai Wang et al. "Scale-Up of Room-Temperature Constructive Quantum Interference from Single Molecules to Self-Assembled Molecular-Electronic Films". In: *Journal of the American Chemical Society* 142 (19 2020), pp. 8539–9080. DOI: 10.1021/jacs.9b.

[27] Daniel Platz. "Reconstructing force from harmonic motion". PhD thesis. Royal Institute of Technology, Stockholm, Sweden, 2013.

[28] Mark Theodore Noble. "New Methods of Measurements in Superfluid Helium". PhD thesis. Lancaster University, Lancashire, United Kingdom, 2013.

[29] A. M. Sweetman et al. "Mapping the force field of a hydrogen-bonded assembly". In: *Nature Comms* 5 (1 2014), p. 3931. DOI: 10.1038/ncomms4931.

[30] A. M. Sweetman et al. "The Force Needed to Move an Atom on a Surface". In: *Science* 319 (5866 2008), pp. 1066–1069. DOI: 10.1126/science.1150288.

[31] Sam Jarvis et al. "Measuring the mechanical properties of molecular conformers". In: *Nature Communications* 6 (12 2015), p. 8338. DOI: 10.1038/ncomms9338.

[32] D P Allison et al. "Immobilization of DNA for scanning probe microscopy". In: *Proc. Natl. Acad. Sci. USA* 89 (1992), pp. 10129–10133. DOI: 10.1073/pnas.89.21.10129.

[33] Florian Albrecht et al. "Direct Identification and Determination of Conformational Response in Adsorbed Individual Nonplanar Molecular Species Using Noncontact Atomic Force Microscopy". In: *Nano Lett.* 16 (12 2016), pp. 7703–7709. DOI: 10.1021/acs.nanolett.6b03769.

[34] Franz J. Giessibl. "AFM's path to atomic resolution". In: *Materials Today* 8 (5 2005), pp. 32–41. DOI: 10.1016/S1369-7021(05)00844-8.

[35] Jian Shi et al. *Method and apparatus of using peak force tapping mode to measure physical properties of a sample.* U.S. Patent US8650660B2, published 2014.

[36] P Pou et al. "Structure and stability of semiconductor tip apexes for atomic force microscopy". In: *Nanotechnology* 20.264015 (2009). DOI: 10.1088/0957-4484/20/26/264015.

[37] Ayhan Yurtsever et al. "Understanding image contrast formation in TiO_2 with force spectroscopy". In: *Phys. Rev. B* 85.125416 (2012). DOI: 10.1103/PhysRevB.85.125416.

[38] Samuel Paul Jarvis, Lev Kantorovich, and Philip Moriarty. "Structural development and energy dissipation in simulated silicon apices". In: *Beilstein J. Nanotechnol.* 4 (2013), pp. 941–948. DOI: 10.3762/bjnano.4.106.

[39] Yoshiaki Sugimoto et al. "Simultaneous AFM and STM measurements on the Si(111)-(7 × 7) surface". In: *Physical Review B* 81.245322 (2010).

[40] C. Baüerle et al. "Studies of 2D Cryocrystals by STM Techniques". In: *Journal of Low Temperature Physics* 113.5/6 (1998). DOI: 10.1023/A:1022523510598.

[41] Naokazu Kitamura, Atsushi Oshiyama, and Osamu Sugino. "Atomic and Electronic Structures of Deformed Graphite Sheets". In: *J. Phys. Soc. Jpn.* 67 (1998), pp. 3976–3984. DOI: 10.1143/JPSJ.67.3976.

[42] Prokop Hapala et al. "Mechanism of high-resolution STM/AFM imaging with functionalized tips". In: *Phys. Rev. B* 90.085421 (8 2014). DOI: 10.1103/PhysRevB.90.085421.

[43] Prokop Hapala et al. "Origin of High-Resolution IETS-STM Images of Organic Molecules with Functionalized Tips". In: *Phys. Rev. Lett.* 113.226101 (22 2014). DOI: 10.1103/PhysRevLett.113.226101.

[44] Pengcheng Chen et al. "Breaking a dative bond with mechanical forces". In: *Nature Communications* 12.5635 (1 2021). DOI: 10.1038/s41467-021-25932-6.

[45] Samuel Paul Jarvis et al. "Intermolecular artifacts in probe microscope images of C60 assemblies". In: *Physical Review B* 92.24 (2015), p. 241405.

[46] Daniel S. Wastl, Alfred J. Weymouth, and Franz J. Giessibl. "Optimizing atomic resolution of force microscopy in ambient conditions". In: *Physical Review B* 87.245415 (2013). DOI: 10.1103/PhysRevB.87.245415.

[47] J. Mannhart S. Hembacher * F.J. Giessibl. "Evaluation of a force sensor based on a quartz tuning fork for operation at low temperatures and ultrahigh vacuum". In: *Applied Surface Science* 188 (2002), 445±449. DOI: 10.1016/S0169-4332(01)00976-X.

[48] L.D. Landau and E.M. Lifshitz. *Fluid Mechanics*. Pergamon Press, 1987.

[49] Jordan M. Klingsporn et al. "Intramolecular Insight into Adsorbate–Substrate Interactions via Low-Temperature, Ultrahigh-Vacuum Tip-Enhanced Raman Spectroscopy". In: *J. Am. Chem. Soc.* 136 (10 2014), pp. 3881–3887. DOI: 10.1021/ja411899k.

[50] Hong Li et al. "From Bulk to Monolayer MoS2: Evolution of Raman Scattering". In: *Advanced Functional Materials* 22.7 (2012), pp. 1321–1538. DOI: 10.1002/adfm.201102111.

[51] Kin Fai Mak et al. "Atomically Thin MoS 2: A New Direct-Gap Semiconductor". In: *Physical Review Letters* 105.136805 (2010). DOI: 10.1103/PhysRevLett.105.136805.

[52] D. A. Long. *Raman Spectroscopy*. McGraw-Hill International Book Company, 1977.

[53] S. Reich et al. "Tight-binding description of graphene". In: *Physical Review B* 66.035412 (2002). DOI: 10.1103/PhysRevB.66.035412.

[54] J. Gonza´lez, F. Guinea, and M. A. H. Vozmediano. "Electron-electron interactions in graphene sheets". In: *Physical Review B* 63.134421 (2001). DOI: 10.1103/PhysRevB.63.134421.

[55] K. S. Novoselov et al. "Electric Field Effect in Atomically Thin Carbon Films". In: *Science* 306 (5696 2004), pp. 666–669. DOI: 10.1126/science.110289.

[56] Charles Kittel. *Introduction to Solid State Physics*. Eighth. John Wiley and Sons, Incorporated, 2005.

[57] S. M. Lindsay. *Introduction to Nanoscience*. Oxford University Press, 2010.

[58] Matthew James Fong. "Novel Physical Security Devices Exploiting the Optical Properties of Low-Dimensional Materials". PhD thesis. Lancaster University, Mar. 2022.

[59] Andrea Splendiani et al. "Emerging Photoluminescence in Monolayer MoS_2". In: *Nano Letters* 10 (4 2010), pp. 1271–1275. DOI: 10.1021/nl903868w.

[60] Sajedeh Manzeli et al. "2D Transmission Metal Dichalcogenides". In: *Nature Reviews Materials* 2 (8 2017), pp. 1–15. DOI: 10.1038/natrevmats.2017.33.

[61] Philipp Tonndorf et al. "Photoluminescence emission and Raman response of monolayer MoS_2, $MoSe_2$, and WSe_2". In: *Opt. Express* 21.4 (2013), pp. 4908–4916. DOI: 10.1364/OE.21.004908.

[62] Daniel Rhodes et al. "Disorder in van der Waals heterostructures of 2D materials". In: *Nature Materials* 18 (3 2019), pp. 541–549. DOI: 10.1038/s41563-019-0366-8.

[63] Mahito Yamamoto et al. "Self-Limiting Oxides on WSe2 as Controlled Surface Acceptors and Low-Resistance Hole Contacts". In: *Nano Letters* 16 (4 2016), pp. 2720–2727. DOI: 10.1021/acs.nanolett.6b00390.

[64] Tawinan Cheiwchanchamnangij and Walter R. L. Lambrecht. "Quasiparticle band structure calculation of monolayer, bilayer, and bulk MoS_2". In: *Physical Review B* 85 (20 2012). DOI: 10.1103/PhysRevB.85.205302.

[65] Xing-Fei He. "Excitons in anisotropic solids: The model of fractional-dimensional space". In: *Physical Review B* 43 (3 1991). DOI: 10.1103/PhysRevB.43.2063.

[66] Tianshu Li and Giulia Galli. "Electronic Properties of MoS_2 Nanoparticles". In: *J. Phys. Chem. C* 111 (44 2007). DOI: 10.1021/jp075424v.

[67] Kin Fai Mak et al. "Tightly bound trions in monolayer MoS_2". In: *Nature Materials* 12 (2013). DOI: 10.1038/nmat3505.

[68] Gerd Plechinger et al. "Identification of excitons, trions and biexcitons in single-layer WS2". In: *Rapid Research Letters* 9 (8 2015), pp. 457–461. DOI: 10.1002/pssr.201510224.

[69] Sefaattin Tongay et al. "Defects activated photoluminescence in two-dimensional semiconductors: interplay between bound, charged and free excitons". In: *Scientific Reports* 3.2657 (2013). DOI: 10.1038/srep02657.

[70] H. Sahin et al. "Anomalous Raman Spectra and Thickness Dependent Electronic properties of WSe_2". In: *Phys. Rev. B* 87.165409 (2013). DOI: 10.1103/PhysRevB.87.165409.

[71] Y S Chang et al. "Surface electron accumulation and enhanced hydrogen evolution reaction in $MoSe_2$ basal planes". In: *Nano Energy* 84.105922 (2021). DOI: 10.1016/j.nanoen.2021.105922.

[72] Rafik Addou, Luigi Colombo, and Robert M Wallace. "Surface Defects on Natural MoS_2". In: *ACS Appl. Mater. Interfaces* 7 (22 2015), pp. 11921–11929. DOI: 10.1021/acsami.5b01778.

[73] William H Blades et al. "Thermally Induced Defects on WSe_2". In: *J. Phys. Chem. C* 124 (28 2020), pp. 15337–15346. DOI: 10.1021/acs.jpcc.0c04440.

[74] Matthew Yankowitz, Devin McKenzie, and Brian J LeRoy. "Local Spectroscopic Characterization of Spin and Layer Polarization in WSe_2". In: *Physical Review Letters* 115.136803 (2015). DOI: 10.1103/PhysRevLett.115.136803.

[75] Pèter Vancsó et al. "The intrinsic defect structure of exfoliated MoS_2 single layers revealed by Scanning Tunneling Microscopy". In: *Scientific Reports* 6.29726 (2016). DOI: 10.1038/srep29726.

[76] Chendong Zhang et al. "Engineering Point-Defect States in Monolayer WSe_2". In: *ACS Nano* 13 (2 2019), pp. 1595–1602. DOI: 10.1021/acsnano.8b07595.

[77] Elmar Mitterreiter et al. "Atomistic Positioning of Defects in Helium Ion Treated Single-Layer MoS_2". In: *Nano Lett.* 20 (6 2020), pp. 4437–4444. DOI: 10.1021/acs.nanolett.0c01222.

[78] János Petö et al. "Spontaneous doping of the basal plane of MoS2 single layers through oxygen substitution under ambient conditions". In: *Nature Chemistry* 10 (2018), pp. 1246–1251. DOI: 10.1038/s41557-018-0136-2.

[79] Yameng Cao et al. "Optical identification using imperfections in 2D materials". In: *2D Materials* 4.045021 (4 2017). DOI: 10.1088/2053-1583/aa8b4d.

[80] Zhangting Wu et al. "Defects as a factor limiting carrier mobility in WSe2: A spectroscopic investigation". In: *Nano Research* 9 (12 2016), pp. 3622–3631. DOI: 10.1007/s12274-016-1232-5.

[81] Philippe K. Chow et al. "Defect-Induced Photoluminescence in Monolayer Semiconducting Transition Metal Dichalcogenides". In: *ACS Nano* 9 (2 2015), pp. 1520–1527. DOI: 10.1021/nn5073495.

[82] Jian Gao et al. "Aging of Transition Metal Dichalcogenide Monolayers". In: *ACS Nano* 10 (2 2016), pp. 2628–2635. DOI: 10.1021/acsnano.5b07677.

[83] Gwan-Hyoung Lee et al. "Highly Stable, Dual-Gated MoS2 Transistors Encapsulated by Hexagonal Boron Nitride with Gate-Controllable Contact, Resistance, and Threshold Voltage". In: *ACS Nano* 9 (7 2015), pp. 7019–7026. DOI: 10.1021/acsnano.5b01341.

[84] N. Severin et al. "Atomic resolution with high-eigenmode tapping mode atomic force microscopy". In: *Physical Review Research* 4.023149 (2 2022). DOI: 10.1103/PhysRevResearch.4.023149.

[85] Krystian Nowakowski, Harold J W Zandvliet, and Pantelis Bampoulis. "Barrier Inhomogeneities in Atomic Contacts on WS_2". In: *Nano Lett.* 19 (2 2018), pp. 1190–1196. DOI: 10.1021/acs.nanolett.8b04636.

[86] Elisa Castanon Garcia-Roves. "Van Der Waals heterostructures: fabrication and nanoscale electronic and thermal characterisation via SPM methods". PhD thesis. Lancaster University, Apr. 2021.

[87] Matthew Hamer. "Fabrication and Characterisation of Air-Sensitive InSe based Heterostructure Devices". PhD thesis. Manchester University, Dec. 2018.

[88] Zhengyang Cai et al. "Chemical Vapor Deposition Growth and Applications of Two-Dimensional Materials and Their Heterostructures". In: *Chemical Reviews* 118 (13 2018), pp. 6091–6133. DOI: 10.1021/acs.chemrev.7b00536.

[89] Saban M. Hus and An-Ping Li. "Spatially-resolved studies on the role of defects and boundaries in electronic behavior of 2D materials". In: *Progress in Surface Science* 92 (3 2017), pp. 176–201. DOI: 10.1016/j.progsurf.2017.07.001.

[90] Yenny Hernandez et al. "High-yield production of graphene by liquid-phase exfoliation of graphite". In: *Nature Nanotechnology* 3 (2008), pp. 563–568. DOI: 10.1038/nnano.2008.215.

[91] Adriano Ambrosi, Zdeněk Sofer, and Martin Pumera. "Lithium Intercalation Compound Dramatically Influences the Electrochemical Properties of Exfoliated MoS_2". In: *Small* 11 (5 2015), pp. 605–612. DOI: 10.1002/smll.201400401.

[92] William S. Hummers and Richard E. Offeman. "Preparation of Graphitic Oxide". In: *J. Am. Chem. Soc.* 80 (6 1958), p. 1339. DOI: 10.1021/ja01539a017.

[93] Aidan. P. Rooney et al. "Observing Imperfection in Atomic Interfaces for van der Waals Heterostructures". In: *Nano Letters* 17 (9 2017), pp. 5222–5228. DOI: 10.1021/acs.nanolett.7b01248.

[94] Hao Xin and Wei Li. "A review on high throughput roll-to-roll manufacturing of chemical vapor deposition graphene". In: *Applied Physics Reviews* 5.031105 (3 2018). DOI: 10.1063/1.5035295.

[95] Sukang Bae et al. "Roll-to-roll production of 30-inch graphene films for transparent electrodes". In: *Nature Nanotechnology* 5 (8 2010), pp. 574–578. DOI: 10.1038/NNANO.2010.132.

[96] Matthew A. Meitl et al. "Transfer printing by kinetic control of adhesion to an elastomeric stamp". In: *Nature Materials* 5 (2006), pp. 33–38. DOI: 10.1038/nmat1532.

[97] Alfonso Reina et al. "Transferring and Identification of Single- and Few-Layer Graphene on Arbitrary Substrates". In: *Journal of Physical Chemistry C* 112 (46 2008). DOI: 10.1021/jp807380s.

[98] Daniil Marinov et al. "Reactive plasma cleaning and restoration of transition metal dichalcogenide monolayers". In: *npj 2D Mater Appl* 5.17 (2021). DOI: 10.1038/s41699-020-00197-7.

[99] V. E. Calado et al. "Formation and control of wrinkles in graphene by the wedging transfer method". In: *Applied Physics Letters* 101.103116 (2012). DOI: 10.1063/1.4751982.

[100] Yuanzheng Li et al. "Accurate identification of layer number for few-layer WS2 and WSe2 via spectroscopic study". In: *Nanotechnology* 29.12 (2018), p. 124001. DOI: 10.1088/1361-6528/aaa923.

[101] Namphung Peimyoo et al. "Nonblinking, Intense Two-Dimensional Light Emitter: Monolayer WS_2 Triangles". In: *ACS Nano* 7 (12 2013), pp. 10985–10994. DOI: 10.1021/nn4046002.

[102] Nils Scheuschner et al. "Photoluminescence of freestanding single- and few-layer MoS_2". In: *Physical Review B* 89.125406 (2014). DOI: 10.1103/PhysRevB.89.125406.

[103] Carlo M. Orofeo et al. "Scalable synthesis of layer-controlled WS_2 and MoS_2 sheets by sulfurization of thin metal films". In: *Appl. Phys. Lett.* 105.083112 (2014). DOI: 10.1063/1.4893978.

[104] Pantelis Bampoulis et al. "Defect Dominated Charge Transport and Fermi Level Pinning in MoS_2/Metal Contacts". In: *ACS Applied Materials and Interfaces* 9 (22 2017), pp. 19278–19286. DOI: 10.1021/acsami.7b02739.

[105] Muhammad R. Islam et al. "Tuning the electrical property via defect engineering of single layer MoS2 by oxygen plasma". In: *Nanoscale* 6 (2014), pp. 10033–10039. DOI: 10.1039/C4NR02142H.

[106] Narae Kang et al. "Photoluminescence Quenching in Single-Layer MoS2 via Oxygen Plasma Treatment". In: *J. Phys. Chem. C* 118 (36 2014), pp. 21258–21263. DOI: 10.1021/jp506964m.

[107] Suhhyun Kim et al. "Effects of plasma treatment on surface properties of ultrathin layered MoS_2". In: *2D Mater.* 3.3 (2016), p. 035002. DOI: 10.1088/2053-1583/3/3/035002.

[108] Hongsheng Liu, Nannan Han, and Jijun Zhao. "Atomistic insight into the oxidation of monolayer transition metal dichalcogenides: from structures to electronic properties". In: *RSC Adv.* 5 (2015), pp. 17572–17581. DOI: 10.1039/C4RA17320A.

[109] Roberto C Longo et al. "Intrinsic air stability mechanisms of two-dimensional transition metal dichalcogenide surfaces: basal versus edge oxidation". In: *2D Materials* 4.2 (2017). DOI: 10.1088/2053-1583/aa636c.

[110] Bruno Schuler et al. "How Substitutional Point Defects in Two-Dimensional WS_2 Induce Charge Localization, Spin–Orbit Splitting, and Strain". In: *ACS Nano* 13 (9 2019), pp. 10520–10534. DOI: 10.1021/acsnano.9b04611.

[111] K A Cochrane et al. "Intentional carbon doping reveals CH as an abundant charged impurity in nominally undoped synthetic WS_2 and WSe_2". In: *2D Mater.* 7.3 (2020), p. 031003. DOI: 10.1088/2053-1583/ab8543.

[112] Martik Aghajanian et al. "Resonant and bound states of charged defects in two-dimensional semiconductors". In: *Phys. Rev. B* 101 (8 2020), 081201(R). DOI: 10.1103/PhysRevB.101.081201.

[113] Yu Jie Zheng et al. "Point Defects and Localized Excitons in 2D WSe_2". In: *ACS Nano* 13 (5 2019), pp. 6050–6059. DOI: 10.1021/acsnano.9b02316.

[114] Shuai Zhang et al. "Defect Structure of Localized Excitons in a WSe_2 Monolayer". In: *Phys. Rev. Lett.* 119.046101 (4 2017). DOI: 10.1103/PhysRevLett.119.046101.

[115] C B González Biel and Y J Dappe. "Theoretical characterisation of point defects on a MoS_2 monolayer by scanning tunnelling microscopy". In: *Nanotechnology* 27.10 (2016), p. 105702. DOI: 10.1088/0957-4484/27/10/105702.

[116] Gioele Mirabelli et al. "Air sensitivity of MoS_2, $MoSe_2$, $MoTe_2$, HfS_2, and $HfSe_2$". In: *Journal of Applied Physics* 120.125102 (12 2016). DOI: 10.1063/1.4963290.

[117] Fan Ye et al. "Environmental Instability and Degradation of Single- and Few-Layer WTe2 Nanosheets in Ambient Conditions". In: *Small* 12 (42 2016), pp. 5802–5808. DOI: 10.1002/smll.201601207.

[118] K. Iordanidou et al. "Oxygen and hydroxyl adsorption on MS_2 (M = Mo, W, Hf) monolayers: a first-principles molecular dynamics study". In: *Phys. Status Solidi—RRL* 10 (11 2016), pp. 787–791. DOI: 10.1002/pssr.201600210.

[119] KC Santosh et al. "Surface oxidation energetics and kinetics on MoS_2 monolayer". In: *Journal Of Applied Physics* 117.135301 (2015). DOI: 10.1063/1.4916536.

[120] Zhangting Wu et al. "Defect Activated Photoluminescence in WSe2Monolayer". In: *The Journal of Physical Chemistry C* 121 (22 2017), pp. 11977–12504. DOI: 10.1021/acs.jpcc.7b0.

[121] Tengfei Yan et al. "Photoluminescence properties and exciton dynamics in monolayer WSe_2". In: *Appl. Phys. Lett.* 105.101901 (10 2014). DOI: 10.1063/1.4895471.

[122] R. O. C. Norman and D. J. Waddington. *Modern Organic Chemistry*. Park Scientific Instruments, 1993.

[123] Charles Ruggieri et al. "Zinc(II) Tetraphenylporphyrin Adsorption on Au(111): An Interplay Between Molecular Self-Assembly and Surface Stress". In: *J. Phys. Chem. C* 119 (11 2015), pp. 6101–6110. DOI: 10.1021/acs.jpcc.5b00217.

[124] Ralph W. G. Wyckoff. *Crystal Structures*. 2nd. Vol. Volume 1. John Wiley and Sons, Incorporated, 1963.

[125] J. V. Barth et al. "Scanning tunneling microscopy observations on the reconstructed Au(111) surface: Atomic structure, long-range superstructure, rotational domains, and surface defects". In: *Physical Review B* 42.15 (1990), p. 9307. DOI: 10.1103/PhysRevB.42.9307.

[126] Felix Hanke and Jonas Björk. "Structure and local reactivity of the Au(111) surface reconstruction". In: *Physical Review B* 87 (23 2013), p. 235422. DOI: 10.1103/PhysRevB.87.235422.

[127] R Temirov et al. "A novel method achieving ultra-high geometrical resolution in scanning tunnelling microscopy". In: *New Journal of Physics* 10.053012 (2008). DOI: 10.1088/1367-2630/10/5/053012.

[128] Jun Zhang et al. "Real-Space Identification of Intermolecular Bonding with Atomic Force Microscopy". In: *Science* 342 (6158 2013), pp. 611–614. DOI: 10.1126/science.1242603.

[129] Niko Pavliček et al. "Atomic Force Microscopy Reveals Bistable Configurations of Dibenzo[a,h]thianthrene and their Interconversion Pathway". In: *Phys. Rev. Lett.* 108 (8 Feb. 2012), p. 086101. DOI: 10.1103/PhysRevLett.108.086101.

[130] R Pawlak et al. "High-resolution imaging of C60 molecules using tuning-fork-based non-contact atomic force microscopy". In: *Journal of Physics: Condensed Matter* 24.8 (2012), p. 084005. DOI: 10.1088/0953-8984/24/8/084005.

[131] Leo Gross et al. "Bond-Order Discrimination by Atomic Force Microscopy". In: *Science* 337 (6100 2012), pp. 1326–1329. DOI: 10.1126/science.1225621.

[132] César Moreno et al. "Imaging Three-Dimensional Surface Objects with Submolecular Resolution by Atomic Force Microscopy". In: *Nano Letters* 15 (4 2015), pp. 1530–6984. DOI: 10.1021/nl504182w.

[133] Fabian Mohn, Leo Gross, and Gerhard Meyer. "Measuring the short-range force field above a single molecule with atomic resolution". In: *Applied Physics Letters* 99 (5 2011), p. 053106. DOI: 10.1063/1.3619829.

[134] Bruno Schuler et al. "Adsorption geometry determination of single molecules by atomic force microscopy". In: *Physical review letters* 111.10 (2013), p. 106103.

[135] Takashi Yokoyama et al. "Nonplanar adsorption and orientational ordering of porphyrin molecules on Au(111)". In: *The Journal of Chemical Physics* 115.8 (2001), pp. 3814–3818. DOI: 10.1063/1.1389276.

[136] Violeta Iancu, Aparna Deshpande, and Saw-Wai Hla. "Manipulating Kondo Temperature via Single Molecule Switching". In: *Nano Letters* 6 (4 2006), pp. 820–823. DOI: 10.1021/nl0601886.

[137] S. P. Jarvis et al. "Physisorption Controls the Conformation and Density of States of an Adsorbed Porphyrin". In: *Journal of Physical Chemistry C* 119 (50 2015), pp. 27982–27994. DOI: 10.1021/acs.jpcc.5b08350.

[138] Willi Auwärter et al. "Controlled Metalation of Self-Assembled Porphyrin Nanoarrays in Two Dimensions". In: *Chem. Phys. Chem.* 8 (2 2007), pp. 250–254. DOI: 10.1002/cphc.200600675.

[139] Willi Auwärter et al. "Self-assembly and conformation of tetrapyridyl-porphyrin molecules on Ag(111)". In: *The Journal of Chemical Physics* 124.194708 (19 2006). DOI: 10.1063/1.2194541.

[140] M. P. de Jong et al. "Orbital-specific dynamic charge transfer from Fe(II)-tetraphenylporphyrin molecules to molybdenum disulfide substrates". In: *Physical Review B* 72.035448 (3 2005). DOI: 10.1103/PhysRevB.72.035448.

[141] L. Scudiero, Dan E. Barlow, and K. W. Hipps. "Physical Properties and Metal Ion Specific Scanning Tunneling Microscopy Images of Metal(II) Tetraphenylporphyrins Deposited from Vapor onto Gold (111)". In: *J. Phys. Chem. B* 104 (50 2000), pp. 11899–11905. DOI: 10.1021/jp002292w.

[142] Alexander Weber-Bargioni et al. "Visualizing the Frontier Orbitals of a Conformationally Adapted Metalloporphyrin". In: *Chem. Phys. Chem* 9 (1 2008), pp. 89–94. DOI: 10.1002/cphc.200700600.

[143] Willi Auwärter et al. "Site-specific electronic and geometric interface structure of Co-tetraphenyl-porphyrin layers on Ag(111)". In: *Physical Review B* 81.245403 (24 2010). DOI: 10.1103/PhysRevB.81.245403.

[144] Philip Donovan et al. "Unexpected Deformations Induced by Surface Interaction and Chiral Self-Assembly of CoII-Tetraphenylporphyrin (Co-TPP) Adsorbed on Cu(110): A Combined STM and Periodic DFT Study". In: *J. Chem. Phys.* 16 (38 2010), pp. 11641–11652. DOI: 10.1002/chem.201001776.

[145] K. Diller et al. "Self-metalation of 2H-tetraphenylporphyrin on Cu(111): An x-ray spectroscopy study". In: *J. Chem. Phys.* 136.014705 (1 2012). DOI: 10.1063/1.3674165.

[146] Xiao-Lei Zhang et al. "Identifying the Assembly Configuration and Fluorescence Spectra of Nanoscale Zinc-Tetraphenylporphyrin Aggregates with Scanning Tunneling Microscopy". In: *Scientific Reports* 6.22756 (2016). DOI: 10.1038/srep22756.

[147] Soichiro Yoshimoto et al. "Identifying the Assembly Configuration and Fluorescence Spectra of Nanoscale Zinc-Tetraphenylporphyrin Aggregates with Scanning Tunneling Microscopy". In: *Journal of Chemical Physics* 319 (1-3 2005), pp. 147–158. DOI: 10.1016/j.chemphys.2005.04.038.

[148] Oreste De Luca et al. "Zinc(II) tetraphenylporphyrin on Au(111) investigated by scanning tunnelling microscopy and photoemission spectroscopy measurements". In: *Nanotechnology* 31.36 (2020), p. 365603. DOI: 10.1088/1361-6528/ab95ba.

[149] Yonghua Lu et al. "Electrostatic force microscopy on oriented graphite surfaces: coexistence of insulating and conducting behaviors". In: *Physical Review Letters* 97.076805 (7 2006). DOI: 10.1103/PhysRevLett.97.076805.

[150] Matthew R Rosenberger et al. "Nano-"Squeegee" for the Creation of Clean 2D Material Interfaces". In: *Appl. Mater. Interfaces* 10 (12 2018), pp. 10379–10387. DOI: 10.1021/acsami.8b01224.

[151] Christopher Stephen Woodhead. "Enhancing the Light Output of Solid State Emitters". PhD thesis. Lancaster University, Oct. 2017.

[152] Daniel Rhodes et al. "Disorder in van der Waals heterostructures of 2D materials". In: *Nature Materials* 18 (2019), pp. 541–549. DOI: 10.1038/s41563-019-0366-8.

[153] Yen-Ju Chiang et al. "MoS2 with Stable Photoluminescence Enhancement under Stretching via Plasmonic Surface Lattice Resonance". In: *Nanomaterials* 11.1698 (7 2021). DOI: 10.3390/nano11071698.

[154] A. V. Kretinin et al. "Electronic Properties of Graphene Encapsulated with Different Two-Dimensional Atomic Crystals". In: *Nano Letters* 14 (6 2014), pp. 3270–3276. DOI: 10.1021/nl5006542.

[155] Anish Mistry et al. "The Synthesis and STM/AFM Imaging of 'Olympicene' Benzo[cd]pyrenes". In: *Chemistry – A European Journal* 21 (5 2015), pp. 2011–2018. DOI: 10.1002/chem.201404877.

[156] Qingqing Wu et al. "Tuning the surface states of TiO2 using Cu5 atomic clusters". In: *Applied Surface Science* 594.153455 (5 2022). DOI: 0.1016/j.apsusc.2022.153455.

[157] Thorsten Wölfle, Görlinga Andreas, and Wolfgang Hieringer. "Conformational flexibility of metalloporphyrins studied by density-functional calculations". In: *Physical Chemistry Chemical Physics* 10 (37 2008), pp. 5739–5742. DOI: 10.1039/B800566B.